Adaptive control, regularization techniques and their applications in image

Khua Bux Amur

THÈSE DE DOCTORAT
De L'UNIVERSITÉ PAUL VERLAINE-METZ
ÉCOLE DOCTORALE IAEM

Spécialité

MATHÉMATIQUES APPLIQUÉES

Présentée par

Amur Khuda Bux

Sujet de la thèse:

CONTRÔLE ADAPTATIF, TECHNIQUES DE RÉGULARISATION ET APPLICATIONS EN ANALYSE D'IMAGES

Soutenue le 19 Septembre 2011 devant le jury composé de:

Frédéric Hecht	Université Pierre et Marie Curie	Rapporteur
Étienne Mémin	INRIA(Rennes)	Rapporteur
Xavier Antoine	Université Henri Poincaré (Nancy)	Examinateur
Faker Ben Belgacem	Université de Technologie de Compiègne	Examinateur
Ralph Chill	Université Paul Verlaine-Metz	Examinateur
Abderrahim El Moataz	Université de Caen	Examinateur
Zakaria Belhachmi	Université de Haute Alsace	Directeur de thèse

---

Laboratoire de Mathématiques et Applications de Metz

UMR 7122, Bât. A, Ile du Saulcy, F-57045 METZ Cedex 1 Metz-FRANCE

Ph.D THESIS
OF THE UNIVERSITY PAUL VERLAINE-METZ
DOCTORAL SCHOOL IAEM

Specialty

APPLIED MATHEMATICS

PRESENTED BY

Amur Khuda Bux

The Thesis Subject:

ADAPTIVE CONTROL, REGULARIZATION TECHNIQUES AND THEIR APPLICATIONS IN IMAGE PROCESSING

Defended on September 19, 2011 in front of the the jury:

Frédéric Hecht	Université Pierre et Marie Curie	Reviewer
Étienne Mémin	INRIA(Rennes)	Reviewer
Xavier Antoine	Université Henri Poincaré(Nancy)	Examiner
Faker Ben Belgacem	Université de Technologie de Compiègne	Examiner
Ralph Chill	Université Paul Verlaine-Metz	Examiner
Abderrahim El Moataz	Université de Caen	Examiner
Zakaria Belhachmi	Université de Haute Alsace	Thesis Director

Laboratory of Mathematics and Applications

UMR 7122, Bât. A, Ile du Saulcy, F-57045 METZ Cedex 1 Metz-FRANCE

Dedication

To My Little Son Mufarrih Abass

Acknowledgments

First of all I want to express my gratitude to Almighty Allah the most gracious and merciful who bestowed on me the strength and courage to take up the ever widening field of education and higher research.

I would like to thank Professor Zakaria Belhachmi for his able guidance to conduct this research. It was his inspiration and diligence that enabled me to complete my PhD thesis within time. He guided and helped to shape my thoughts and concepts present in thesis. Moreover, my special thanks goes to the reviewers of the thesis for their precious time and agreeing to review this thesis.

I would thank Professor F.Hecht who introduced me to the skills of computing the optic flow using FreeFEm++. Moreover, I would thank Professor.Joachim Weickert who introduced me the variational techniques in computer vision and image processing during his summer term course on "Differential equations in image processing and computer vision" in 2009.

I would like to thank all the group members of working groups Mathematical imaging and applied mathematics, for providing such a friendly and nice working environment in the Laboratory. Moreover, I would like to thank all the friends, scholars and Laboratory staff for their cooperation and encouragements throughout this work. I want to thank Mr.Jean-Marc Sac-Epée for his help and supports from my first day in Metz to the completion of this work specially in making corrections in the summary of this thesis given in French.

At last I want to thank the Quaid-E-Awam university of Engineering, Science and Technology Nawabshah Sindh-Pakistan for providing me the funding during the preparation of this PhD thesis. Moreover, my special thanks goes to the official administration of Laboratory of Mathematics and Applications Metz for providing a very nice working environment and all possible facilities.

AMUR KHUDA BUX

0.1 Résumé détaillé de la thèse

En analyse d'image, et plus particulièrement en vision assistée par ordinateur, les problèmes de stéreo-vision et les problèmes d'estimation du flot optique ont succ-ité une activité intense de recherche ces deux dernières décennies, recherches portant aussi bien sur l'obtention de modèles adaptés et leur analyse mathématique que sur le développement de méthodes numériques qui permettant la résolution effective de ces problèmes en tenant compte de contraintes, parfois contradictoires, de précision (fidélité à la réalité), de rapidité de calculs (temps réels notamment pour des applications indutrielles), de coûts, ...

Le problème de stéreo-vision consiste à reconstruire des images tridimensionnelles à partir d'images bi-dimensionnelles ou à donner des informations sur la profondeur d'une scène tri-dimensionnelle à partir de deux images prises d'angles différents. L'inconnue dans ces problèmes est une fonction scalaire. Le problème du flot optique est la version vectorielle du précédent; il consiste à déterminer le vecteur déplacement qui décrit le mouvement dans une séquence vidéo. De nombreuses approches, soit statisitiques, soit déterministes, ont été développées pour résoudre ces deux problèmes importants en vision assitée par ordinateur [79, 1, 90, 12, 81, 90, 70, 91, 7, 93, 71, 22, 31]. Parmi les méthodes, celles utilisant des équations aux dérivées partielles et particulièrement les modèles variationnells ont connu un très grand essor et se sont révélés très efficaces et assez souples pour exprimer les différentes contraintes du problème [93, 15, 16, 17, 18, 31, 73].

Dans cette thèse, nous considérons ces deux problèmes dans le cadre de l'approche variationnelle. Celle-ci consiste à chercher la solution comme un état qui minimise une énergie et permet de transférer au domaine de l'analyse d'image tout l'arsenal des méthodes variationnelles développé dans l'étude de problèmes de la physique ou de la mécanique ainsi que l'arsenal de méthodes numértiques qui ont vu le jour dans ce cadre. Précisement, nous cherchons la solution de ces problèmes en minimisant une fonctionnelle énergie qui exprime les contraintes du problème considéré. Ce point de vue conduit inéluctablement à l'étude d'un problème mathématique mal posé [85, 86], au sens où l'existence ou l'unicité de la solution ne sont pas garanties et que la stabilité

par rapport à des perturbations sur les données n'est pas assurée non plus. Ce problème est inhérent à l'absence de données suffisantes (Aperture problem) pour le rendre bien posé.

Usuellement, lorsqu'on veut résoudre un problème mal posé, on rajoute dans l'énergie un terme dit de régularisation. L'ajout de ce terme donne un procédé pour construire des solutions de problèmes auxiliaires qui tendent vers la solution, si elle existe, du problème initial. Le terme ajouté depend en général d'un (ou plusieurs) paramètres destinés à ajuster la contribution de ce terme à l'enérgie. Le choix de ce paramètre, généralement une constante dans les techniques de régularisation, est un sujet crucial qui a suscité d'intenses recherches depuis plus de deux décennies, et pas uniquement dans le domaine de l'analyse d'images mais dans de nombreux domaines où l'on rencontre des problèmes mal posés [85, 86].

Dans ce travail de thèse, le paramètre de régularisation est une fonction de l'espace et non pas simplement une constante, ce qui est une nouveauté dans ce domaine. Le choix de ce paramètre est au coeur de l'approche développée ici et qui fait suite à la méthode introduite dans[12] et appliquée à l'estimation du flot optique. Cette méthode consiste à construire des outils qui vont permettre le choix, en tout point du domaine de calcul, de la valeur du paramètre de régularisation. Elle implique alors un contrôle adaptatif de la régularisation (du terme ajouté à la fonctionnelle). Outre le fait que cette approche permet de résoudre de façon satisfaisante, et automatique, le problème du choix du paramètre de régularisation, elle permet aussi de construire des approches numériques peut coûteuses. Mais le côté le plus attractif de cette méthode dans les problèmes de vision assistée par ordinateur est celui de la dé-densification du flot optique. En effet lorsqu'on résout le problème régularisé, on obtient une solution d'un problème auxiliaire, proche de la solution du problème initial. Or, dans les applications industrielles ou médicales qui utilisent le flot estimé, on a besoin, en plus, de savoir à quels endroits le flot est réel et à quels endroits il est dû à l'effet de régularisation?

La méthode du contrôle adaptatif que nous étudions ici, répond à ce problème de manière satisfaisante parce que la distribution spatiale du paramètre de régularisation joue le rôle d'une cartographie, que nous appellons mesure de confiance, qui montre

et distingue ces deux régions. Il s'agit donc d'une approche qui permet de déterminer la solution de l'un des problèmes considérés de manière précise et efficace, tout en donnant une information a posteriori sur la validité des calculs.

Le manuscrit de thèse comporte deux parties : une partie préliminaire où l'on présente les problèmes considérés dans la thèse et les différentes modélisations proposées en littérature de la vision assistée par ordinateur. Cette partie est loin d'être exhaustive, et nous nous sommes restreints aux approches variationnelles auxquelles appartient cette contribution. Nous étudions également, dans cette partie, les améliorations, principalement numériques, de la méthode originale proposée par Zakaria Belhachmi et Frédéric Hecht [12]. L'objectif ici est de montrer que la méthode ne vise pas à rajouter un nouveau modèle à la liste, déjà longue dans ce domaine, mais qu'elle permet d'améliorer, d'enrichir et de sélectionner, le modèle qui permette une meilleure estimation du flot et la prise en compte de la stratégie de régularisation la plus adaptée par le choix optimal du paramètre. Nous présentons plusieurs expériences numériques basées sur un modèle linéaire qui améliore le terme de données dans la fonctionnelle énergie.

De façon plus détaillée, nous considérons le problème suivant: si on désigne par une fonction f: $\Omega \times (0,T) \longrightarrow \mathbb{R}$ qui représente une séquence d'images $(f(t,x))$ prises le long de l'intervalle de temps $(0,T)$ et $f(.,x)$ est la fonction, qui donne le niveau de gris d'un point (pixel), qu'on désigne par le terme image. Le problème du flot optique peut s'enoncer comme celui de la recherche du champs de vecteur (déplacement) qui correspond aux mouvements dans la séquence donnée. Nous expliquons dans le chapitre 1 comment se représente ce champ de vecteur en général, ce champ est obtenu lorsqu'on écrit les contraintes du mouvement dans une séquence d'images. Ces contraintes peuvent être la conservation du même niveau de gris pour un pixel lors de la prise de vue, ou bien la conservation de son intensité lumineuse, ... Lorsqu'on adopte la conservation du niveau de gris pour chaque pixel, cela se traduit par la relation

$$f(x_1 + u_1, x_2 + u_2, t + 1) = f(x_1, x_2, t) \tag{1}$$

Cette contrainte définit donc le champ de vecteur déplacement (u_1, u_2) qui est précisement le flot optique et dont la détermination rend compte du mouvement dans la séquence d'images. Lorsque les déplacements considérés sont petits, cette contrainte peut se

réecrire comme une équation aux dérivées partielles

$$\frac{\partial f}{\partial t} + \frac{\partial f}{\partial x_1} u_1 + \frac{\partial f}{\partial x_2} u_2 = 0. \tag{2}$$

Le caractère mal posé du problème est alors clair puisque nous ne disposons que d'une équation pour déterminer deux inconnues.

L'approche variationnelle pour résoudre ce problème consiste à introduire une fonctionnelle énergie et d'en déterminer un minimiseur. Dans le cas linéaire, cela revient à minimiser la fonctionnelle

$$E_L(u_1, u_2) = \int_\Omega |\frac{\partial f}{\partial t} + \frac{\partial f}{\partial x_1} u_1 + \frac{\partial f}{\partial x_2} u_2|^2 \, dx + \int_\Omega \alpha(x)(|\mathrm{grad}\, u_1|^2 + |\mathrm{grad}\, u_2|^2) \, dx \tag{3}$$

Le premier terme dans cette expression exprime la contrainte du flot optique et le second correspond au terme de régularisation avec α le paramètre qui, dans la littérature classique, est une constante.

Dans le chapitre 2, nous appliquons la méthode de [12] à un modèle linéaire modifié, en particulier nous présentons divers tests numériques qui permettent de valider l'approche pour ce nouveau modèle. D'une manière générale, la méthode permet la sélection adaptative et correcte du paramètre de régularisation en chaque point de l'espace, ce qui nous donne un algorithme de dé-densification du flot calculé afin qu'il soit le plus proche possible du flot réel. Nous validons cela sur des exemples classiques de la base de données de Middelbury et donnons des valeurs des erreurs qui permettent la comparaison avec les méthodes existantes.

La deuxième partie de la thèse est consacrée à l'extension de la méthode au cadre de la régularisation non linéaire et notamment par variation totale. Nous introduisons dans le chapitre 3, le modèle non linéaire du flot optique par variation totale et sa version modifiée plus adaptée à la simulation numérique. Ensuite, au chapitre 4, nous considérons le problème scalaire de la stéreo-vision. Du point de vue de l'analyse mathématique et numérique les deux modèles se traitent essentiellement de la même manière. C'est pourquoi nous présentons l'étude théorique du chapitre 4 dans le cas de la stéréo-vision. Nous étudions en détail l'existence de solutions, par les méthodes directes de calcul des variations, et établissons les propriétés quamitatives pour la

fonctionnelle non linéaire

$$E_{NL}(u_1, u_2) = \text{terme de données} + \int_\Omega \psi(|\text{grad}\, u_1| + |\text{grad}\, u_2|) \tag{4}$$

Ainsi, nous établissons des résultats d'existence pour le modèle initial (la variation totale), mais cette fonctionnelle a un intérêt purement théorique et se prête mal aux calculs numériques. Nous introduisons donc une fonctionnelle modifée, très souvent utilisée dans les travaux à dominante numérique mais très peu étudiée théoriquement. Nous étudions mathématiquement cette dernière énérgie et obtenons des résultats d'existence dans divers cadres fonctionnels ($W^{1,p}(\Omega)$ et $H^1(\Omega)$). Ce dernier espace étant le cadre naturel de l'approximation de problèmes variationnels.

Ensuite nous présentons la discrétisation de ce problème par la méthode des éléments finis. Bien que la majorité des travaux dans le domaine de l'imagerie numérique utilisent les différences finis pour des raisons historiques, le cadre naturel de l'approximation variationnelle est celui des éléments finis qui permet, entre autres de travailler avec des maillages non structurés et pour lequel on dispose d'une théorie complète de l'approximation. Nous définissons le cadre de l'approximation et nous introduisons les outils necessaires à l'extension de la méthode au cas nonlinéaire ; en particulier, nous introduisons des indicateurs d'erreur résiduels a posteriori pour des problèmes nonlinéaires puisque ce sont précisement ces indicateurs d'erreur qui fournissent le critère de séléction du paramètre. Nous établissons leurs propriétés et déduisons, suivant le modèle linéaire, un algorithme de calcul adaptatif. Les indicateurs que nous introduisons ne sont pas des indicateurs classiques par résidus étudiés notamment par Verfürht [88], mais plutot des indicateurs modifíes intrdoduits par [44] que nous avons adapté à notre problème. L'étude de ces indicateurs permet d' établir l'équivalence avec l'erreur de discrétisation, ce qui dans l'esprit de la méthode [12] se traduit par un critère pour la sélection du choix du paramètre de régularisation.

Nous présentons ensuite divers résultats numériques. Les premiers résultats visent à montrer que la méthode est encore performante dans le cas nonlinéaire et produit bien les résultats escomptés. Notamment, le choix du paramètre de régularisation est toujours aussi efficace. Notons cependant que les résultats numériques sont meilleurs que ne le laissait prédire l'analyse mathématique. Cela s'explique par la complexité,

du point de vue de l'analyse mathématique, du cas non linéaire et la difficulté à obtenir dans ce cas des estimations optimales. D'autres expériences numériques valident l'approche et en montrent toute la force. En revanche, le comportement de la méthode avec des images fortement texturées est, tout en restant meilleur que dans le cas linéaire, moins bon que celui que permettent d'autres méthodes existantes. Il est bien connu, quell que soit la méthode utilisée, que ce cas est difficile en général. La raison principale de ce comportement est liée au modèle lui même ; c'est-à- dire, l'utilisation de la variation totale qui est favorable à des images cartoons (modélisées par des fonctions ѵariations bornées) ou bien l'uitlisation de modèle linéaire plus adaptés aux fonctions de l'espace H^1 (donc peu texturées). Cest aussi le cas dans les problèmes de débruitage pour les régions texturées comme l'avait analysé Yves Meyer [69]. Dans leur papier [1]. Ont proposé un nouveau modèle inspiré des problèmes de déconvolution, qui permet de séparer les parties texturées des parties "à variations bornées". Ce modèle devrait permettre d'améliorer et corriger cet aspect de la méthode. Néanmoins, signalons que ce comportement est aussi intrinsèquement lié à l'utilisation des indicateurs d'erreur qui par nature, tendent à répartir l'erreur de discrétisation uniformément dans le domaine de calcul et de ce fait ne permettent pas toujours de discerner les singularités de l'image de celle du flot optique.

Nous étendons ce travail numérique dans les chapitre 5 au calcul du flot optique et à d'autres fonctionnelles non linéaires, basées sur la variation totale; notamment, nous proposons un modèle anisotrope qui donne de bon résultats et corrige dans une certaine mesure le comportement de la méthode dans les zones texturées. Nous donnons aussi des analyses et des courbes d'erreur qui permettent de comparer aux méthodes existéntes.

La dernier chapitre est consacré à une étude préliminaire dans le cadre de problèmes de débruitage par le modèle de Perona-Malik. L'application de la démarche adoptée dans cette thèse permettrait de simplifier ce modèle et en faciliterait grandement la résolution.

Pour conclure cette présentation, notons que le travail de thèse a permis :

i) De tester les performances de la méthode originale sur un modèle linéaire amélioré

par le renforcement du terme de données. Cela a servi à montrer par des résultats numériques probants, que la méthode est très efficace, automatique, et allie précision et faible coût de calcul. On constate aussi que l'amélioration du terme de données ajouté au caractère lissant des modèles linéaires créent une ambiguité sur le maillage qui augmente le nombre d'éléments aussi bien sur les dicontinuités du flot optique (effet recherché) que sur les discontinutés de l'image (effet indésirable). Le calcul avec des éléments finis d'ordre élevé rend compte plus nettement de ce "paradoxe". Cette ambiguité est partiellement levée lorsqu'on considère les valeurs du flot optique (qui sont correctes comme le montre les calculs d'erreur). Cette ambiguïté ne pourra pas disparaître complétement, mais devrait s'atténuer fortement avec des modèles plus précis et en utilisant une approche plus réaliste des larges déplacements. Le contrôle adaptatif du terme de la régularisation ouvre de la voi à de nombreuses autres applications aussi bien en imagerie que pour des problèmes mal posés dans d'autres domaines de recherche. [ii)] D'étendre la méthode au cadre non linéaire de la variation totale. Cette extension nous a conduit à étudier mathématiquement les modèles considérés, à faire une discrétisation par éléments finis et à faire l' analyse a postériori avec des indicateurs non standard. Ce travail mathématique constitue le fondement qui donne à la méthode sa justification et sa force. La mise en oeuvre de l'algorithme adaptatif qui en découle et les simulations numériques viennent confirmer les prédictions théoriques. Les résultats obtenus sur des exemples issus de la littérature de la vision par ordinateur montrent que la méthode a toute sa place dans ce domaine de l'imagerie et donne des résultats qui supportent parfaitement la comparaison avec les méthodes existantes les plus performantes, en plus d'être complétement novatrice sur le contrôle de la régularisation. Notons, cependant que les performances baissent avec les images fortement texturées (ce qui est souvent le cas quel que soit la méthode utilisée); cet aspect demande un approfondissement, une implementation optimisée et aussi l'utilisation de fonctionnelles énergie plus adaptées à ces images.

iii) Le début de l'application à d'autres problèmes d'imagerie comme la restauration

d'images, présentée ici, avec le modèle de Perona-Malik, est encourageant pour utiliser aussi cette méthodologie comme outil de sélection de modèles.

Une première étape qui se présente comme une perspective de ce travail, en cours, est la mise en oeuvre optimisée pour atteindre les performances des meilleurs méthodes répertoriées dans la littérature spécialisée. Une deuxieme perspective est celle de l'extention de la méthode au cadre des grands déplacements. Enfin, le couplage avec le modèle de décomposition [1] devrait améliorer les performance de la méthode pour des images non essentiellement à variations bornées.

Le premier chapitre est consacré à l'introduction de la thèse. Dans le chapitre deux, le travail débute par l'examen d'un modèle linéaire variationnel pour flot optique, et peut être considéré comme une version améliorée du modèle linéaire proposé dans la note de Z. Belhachmi précédemment évoquée. Dans l'étape suivante, nous étendons nos travaux au cas scalaire (problème vision stéréo), tandis que dans le chapitre 3, où nous considérons le modèle de variation totale (stéréo) qui est non linéaire, nous menons une analyse théorique basée sur des résultats directs de calcul des variations. Nous donnons une version discrétisée du problème faible dans le chapitre quatre. Nous établissons des résultats d'existence et d'unicité pour les problèmes continus et discrets ; par ailleurs, des estimations a priori et a posteriori avec algorithme adaptatif sont au coeur de ce chapitre. À la fin de cette partie, des résultats numériques sont présentés. La dernière partie du chapitre quatre est consacrée à la version améliorée du modèle VT avec approche complémentaire. Avec les mêmes paramètres, nous avons étendu ces idées au cas vectoriel (flot optique), où nous considérons certains modèles variationnels non linéaires pour l'implémentation numérique et les calculs scientifiques relatifs aux problèmes variationnels de flot optique. Finalement, nous avons discuté le problème de débruitage et avons considéré un modèle non linéaire avec diffusivité de Perona-Malik, et avons présenté deux méthodes numériques pour ce problème : dans le premier cas, nous utilisons la méthode des éléments finis avec schéma implicite et, dans le second, nous utilisons un schéma explicite et la méthode des différences finies. On compare enfin les temps de convergence et les résultats scientifiques des deux méthodes.

0.2 Introduction

Nous considérons dans cette thèse la résolution de problèmes issus de l'analyse d'image, qui ont une grande importance dans le domaine de la vision assistée par ordinateur, l'estimation du flot optique et la stéréo vision. Ces deux problèmes sont rencontrés dans de nombreux domaines d'applications de l'imagerie tels que détection et estimation de mouvements (en mécanique des fluides), calcul de champs de déplacements (en mécanique des fractures), guidage de robots, surveillance vidéo, imagerie médicale, ...

Ces problèmes sont généralement mal posés, notamment parce qu'ils sont, par nature,à données incomplètes (champs de camera limité, ...) comme pour le flot optique ou bien ils sont instables pour des perturbations, même petites, des données.

De nombreuses méthodes ont été proposées et mise en oeuvre depuis plus de deux décennies pour résoudre ces problèmes, parmi lesquelles des méthodes basées sur les équations aux dérivées partielles et plus précisément des méthodes variationnelles [1, 12, 8, 19, 20, 16, 17, 24, 20, 51, 93, 65, 66, 90]. L'approche variationnelle consiste à chercher la solution du problème considéré en minimisant une fonctionnelle énérgie qui exprime et traduit certaines proporiétés et contraintes des solutions admissibles. Par exemple, pour le calcul du flot optique, Horn et Schunck ont proposé un des premiers moddèles variationnels (1981) qui consiste à résoudre au sens des moindres carrés une équation qui exprime la constance du niveau de gris pour chaque pixel d'une image dans une séquence vidéo. Nous renvoyons le lecteur intéressé livre de G. Aubert [47], à l'article de review de J. Weickert [19] ainsi qu'à la thèse d'habilitation d'A. Bruhn [17] pour plus de détails sur ces problèmes et les différentes modélisations.

L'emploi des modèles variationnels possède des avantages indiscutables que nous ne détaillerons pas ici. En particulier, ces modèles sont très adaptés pour inclure un terme de régularisation [85, 86] dont l'ajout permet de résoudre le problème considéré. La régularisation, popularisée par le travail pionnier de Tychonov (1977) pour résoudre des problèmes mal posés, dépend en général de paramètres dont le choix est au coeur de nombreux travaux de recherches en théorie de la régularisation depuis plus de 40 ans. Ce choix peut revêtir une grande importance notamment lors de la résolution effective

du problème, sur la qualité des résultats. Le cas de la régularisation linéaire avec un paramètre constant est relativement bien compris, et des choix souvent optimaux du paramètre sont explicites; en revanche dans le cas non linéaire, ce choix est souvent très problématique et purement empirique. La situation devient dramatique lorsque le paramètre en question n'est pas constant et les études et a fortiori les résultats explicites font cruellement défaut.

Dans de nombreux problèmes, le recours à une régularisation avec un paramètre variable peut être un avantage, voire même, peut s'avérer crucial. C'est ce choix de paramètre, dans le cas où c'est une fonction scalaire ou une matrice, qui est au coeur de la méthode que nous étudions dans cette thèse. Plus précisement, nous proposons une méthode qui permette d'effectuer ce choix de manière adaptative et locale. Notre motivation en cela n'est pas uniquement d'accroî tre l'efficacité de la résolution et de réduire le coût des calculs. Mais elle trouve son origine dans la nature du problème à résoudre. En effet, le calcul du flot optique par un modèle variationnel produit un champs de vecteur définit en chaque point du domaine de calcul bien qu'il n'y a que certains pixels, ou certaines zones qui correspondent à un mouvement réel. Cela constitue une faiblesse de ces modèles à laquelle on peut remédier en proposant un moyen pour discerner les endroits où le flot calculé correspond à la contrainte de l'optique flot (les données) des zones où il est essentiellement dû à l'effet de régularisation. Une autre raison pour considérer ce type de régularisation à paramètre variable, par exemple une matrice, est la prise en compte de l'anisotropie du problème où l'effet de régularisation doit être différencié selon la direction considérée.

Une nouvelle méthode, introduite en 2009 par Z. Belhachmi et F. Hecht [12] permet de définir une stratégie de choix de paramètres de régularisation, locale et adaptative. La distribution du paramètre ainsi obtenue à la convergence, fournit une cartographie du domaine de calcul, où il est "facile" de distinguer les zones de mouvement réel (discontinutés du flot), des zones dûe à la régularisation (zones homogènes). C'est cette approche que nous étudions et étendons au cas de la régularisation par variation totale. Cette méthode produit de très bons résultats dans le cas des images faiblement texturées mais ses performances décroissent dans les régions fortement texturées;

cependant elle reste un des rares outis dont nous disposons, à notre connaissance, pour la sélection de paramètres en théorie de la régularisation.

L'outil principal dans cette méthode est l'utilisation d' indicateurs d'erreur a posteriori adaptés et l'obtention d'estimations fines d'équivalence avec l'erreur de discrétisation. Nous obtenons que ces indicateurs, bien choisis, fournissent un critère d'adaptation et de choix local du paramètre de régularisation. En cela nous pouvons dire que la méthode inverse le paradigme (paradogme) dominant en théorie de la régularisation qui consiste à optimiser le choix du paramètre et ensuite discrétiser les équations. Ici, on discrétise puis on optimise le choix du paramètre.

Nous mettons en oeuvre dans cette thèse ce programme dans le cas de problèmes d'analyse d'images et nous pensons que cela démontre aussi que cette approche est assez générale et est certainement applicable dans d'autres domaines, soit pour résoudre des problèmes mal posés, soit encore pour permettre une séléction automatique de modèles.

Contents

List of Figures

List of Tables

Chapter 1

Introduction of Variational models for Optic Flow estimation

1.1 Introduction

1.1.1 Motivation

PDE's based techniques are mathematically well founded and play a major role in the area of image processing and computer vision. Variety of approaches is available in literature to process the image data using mathematical imaging techniques [8, 19, 20, 16, 17, 24, 12, 20, 51, 93, 65, 66, 90].

Amongst the numerous approaches which have been suggested, we focus on partial differential equations (PDE's), and variational approaches in this thesis. These methods have been successfully and widely transferred in computer vision in last two decades [3, 4, 5, 22, 16, 18, 19, 51, 55, 59, 65, 71, 72, 79]. Due to uncertainties in image process and ambiguities in visual interpretation the problems in computer vision are usually ill-posed. One of the main interests in using PDEs is that the theory behind the concept is well-established. Of course, PDE's are written in a continuous setting referring to analog images, and once the existence and the uniqueness have been proven, we need to discretized them in order to find a numerical solution.

Our goal is not to introduce the new mathematical models but we study the adaptive control and regularization methods for existing variational models in computer vision applications [19, 66, 52]. We introduce in this thesis a novel and robust regularization approach for variational techniques in image motion which is recently appeared in the presentation [12]. We demonstrate the effectiveness of our approach on optical flow and stereo vision problems. We start with a short summary on these problems in following paragraphs.

The recovery of the motion information between subsequent frames of an image sequence is one of the crucial research problems in the area of image motion analysis. In this thesis we specifically focus on two mathematical imaging applications, the analysis of image motion in a video sequence and the disparity map in binocular image scene. The first part of this work is devoted to the determination of the velocity of moving objects in a video image sequence called optical flow. In the second part one is there by interested to find the separation depth of pixels between image pair of same scene

called disparity map. We introduce each part shortly as follows.

i. In the First part of our work we discuss the variational optical flow problems to compute flow field $(u_1, u_2)^T$, this flow vector is the solution of following equation called optical flow constraint.

$$f_t + f_{x_1} u_1 + f_{x_2} u_2 = 0$$

if we rewrite this above equation as follows we have

$$-f_t = \nabla f \cdot \mathbf{u}. \tag{1.1}$$

In equation (1.1) $\mathbf{u} = (u_1, u_2)$ is the flow vector and ∇f is gradient of the image. This equation have an interesting meaning. For example if we fix a camera and allow a scene to pass through it then, equation (1.1) says that the rate of change in intensity of a point in image is expressed as the product of spatial rate of change of intensity in the scene and the velocity of the points of scene moving through the camera. Moreover the equation also indicates that flow vector $\mathbf{u}$ must lie on a line perpendicular to the vector (f_{x_1}, f_{x_2}) where f_{x_1} and f_{x_2} are the partial derivatives with respect to x_1 and x_2 respectively as shown in figure 1.1. Let we assume that the partial derivatives are accurate, then the magnitude component of the flow vector in the direction of (f_{x_1}, f_{x_2}) can be expressed as $\frac{-f_t}{|\nabla f|}$ for more details one can refer [34].

Optical flow in 2D specifies how much each pixel moves between adjacent image frames while in 3D, it specifies how much each volume voxel moves between adjacent volumes. In computer vision community, it is well known that the optical flow is a rich source of information about the geometrical structure of the world.

The variational methods based on the computation of the spatial and temporal image derivatives belong to the most efficient and widely used techniques for solving optic flow problems. They consist in the determination of the flow field as a minimizer of a suitable energy functional. TV regularization is a powerful discontinuity-preserving approach [19, 18, 10, 29, 32, 55, 66, 76] to solve ill-posed problems in image processing and computer vision. Including complementary approach with linear model for optical flow as appeared in [52], we consider various nonlinear variational models based on TV regularization to compute optic flow using adaptive finite element method. The

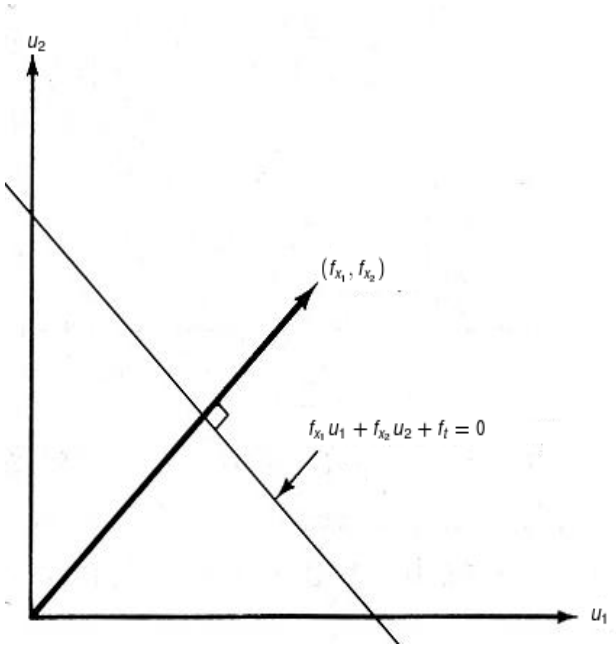

Figure 1.1: Optic Flow Geometry

figure 1.2 shows computed optic flow from an image sequence using TV regularization variational model, which we will discuss in next chapters.

ii. The second part of our work is devoted to the Stereo vision problem using TV regularization approach. Stereo matching is one of the classical problems in the computer vision research has long been studied and lot of research involving new discoveries, techniques and applications has been reported [2, 7, 20, 35, 65, 66, 81] and published over the years. It is quite understandable that the visual information in 3D view possesses more information about the objects in the scene than its counterpart 2D view. Our two eyes give us binocular vision. A point in the scene that we are viewing projects onto one point on the retina of the left eye and a different point on the retina of the right eye. The points are different because our eyes are separated by a few centimeters. The separation of the points is termed as the disparity. There is an inverse relationship between disparity and depth in the scene, the disparity will be relatively large for points in the scene that are near to us and relatively small for points that are far away. Following this principle, stereoscopic imaging uses a pair of images of the same scene obtained from cameras located at slightly different positions.

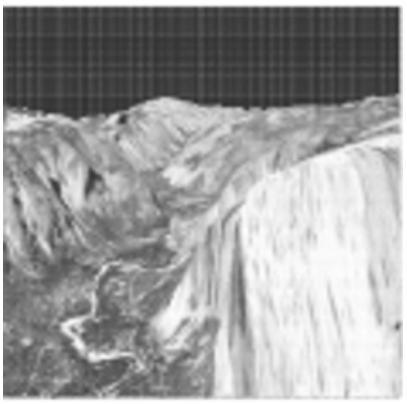

(a) Yosemite image sequence 8th frame

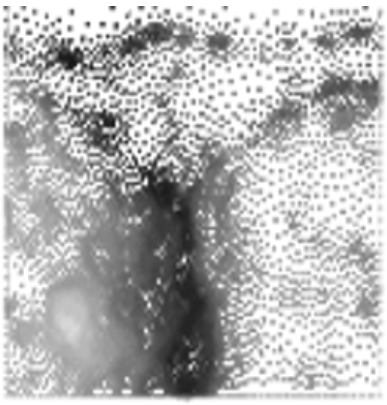

(b) Optic flow field

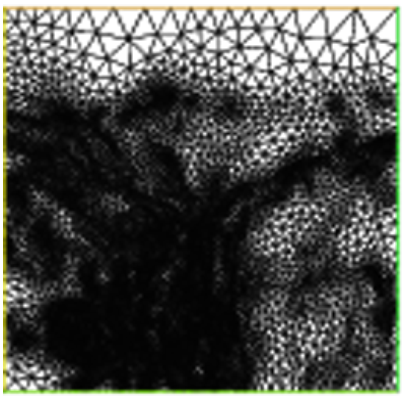

(c) Optic flow on mesh

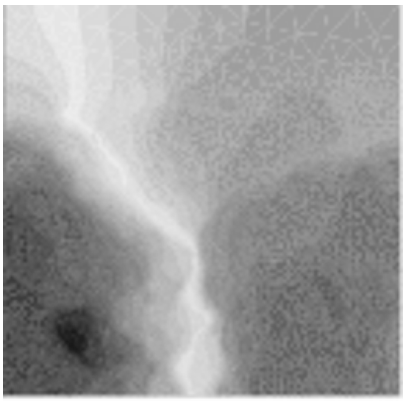

(d) Optic flow magnitude

Figure 1.2: Computed optic flow

Standard formulas exist to calculate depth from disparity, when there is given adequate knowledge of imaging geometry (i.e., camera separation and focal length). However, a major problem is the detection of corresponding points in the left and right images, this process known as stereo matching correspondence problem.

During the image formation process of the cameras, explicit depth information about the scenes is lost. In many applications, such as industrial assembly and inspection, robot obstacle detection and path planning, autonomous vehicle navigation of unfamiliar environments, image based object modeling, surveillance and security, medical image analysis, and human-computer interaction, one of the most critical tasks is the recovery and estimation of depth information. Therefore, the depth information has to be inferred implicitly from the 2D views of the scenes. In the computer vision research, the problem of determining the horizontal disparity map from a pair of images of a same scene captured by two different cameras is called stereo vision problem. Depth by stereo is achieved by estimating the pixel correspondences of similar features in the stereo perspective views originated from the same 3D scene. However, finding correct corresponding points in scene is still an ill posed problem. Some of the factors that make the correspondence problem difficult are depth discontinuities, occlusions, lack of texture, photometric variations and geometric distortions. A number of algorithms have been proposed to address some of the aforementioned problems in stereo vision however, relatively, is still an open problem. Variety of computational approaches is available in literature on the area of stereo vision research [35, 66, 20, 65]. Different approaches are classified in literature as feature based which match characteristic points in the images, e.g., corners[49], area based [35] matching pixels if patches around them exhibit a certain similarity, phase-based [45] that use the phase information in the Fourier domain, and finally energy based approaches [7, 89, 68, 35, 81] which find the disparity by minimizing an energy functional that penalizes deviations from data and smoothness assumptions. later is further divided in to probabilistic and variational approaches. The first type models images and disparity as Markov random fields and tries to find the most probable disparity from given the two images of same scene. This comes down to the minimization of a discrete energy which is usually done

by graph cuts (GC) [89], belief propagation (BP) [58] or dynamic programming (DP) [63] algorithms. However, Li and Zucker [62] have shown that such approaches may have severe drawbacks if the assumption of a piecewise constant disparity is violated. This can be the case if the depth is varying smoothly, for instance in the presence of curved or slanted surfaces. Moreover, the probabilistic approaches suffer from their discrete nature, since they only assign the integer disparity values to the pixels. These restrictions do not apply to the second type of the energy-based methods, variational approaches. Here, the disparity is computed by the minimization of a continuous energy functional which can be done by a gradient descent method. This requires to compute the steady-state of a partial differential equation (PDE), which is of diffusion-reaction type. Variational approaches go back to the work of Horn and Schunck [51], where they have first successfully introduced in optical flow computations. For stereo, they were used, among others, in the work of Slesareva [81], where the authors adapted the very accurate optical flow method of [21] to the weakly calibrated case. By exploiting the known geometry of the two views, they restrict the search for correspondences along epipolar lines. In this work we restrict ourselves to the scenario where the two images have been rectified beforehand and displacements only occur in horizontal direction. Thus the disparity boils down to a pixel wise scalar value. A recent variational stereo method for the rectified case is proposed in [7], which additionally incorporates segmentation ideas and occlusion handling to further improve results at disparity boundaries.

Our work is based on nonlinear variational approach where disparity u is computed via minimization of nonlinear energy functional using direct methods of calculus of variation. From computaional point of view we use adaptive finite element method where we propose a suitable mesh adaptive strategy. Figure 1.3 illustrates an example of the stereo vision problem.

Computational accuracy is greatly influenced by grid quality. Dynamic mesh adaptation on unstructured grids, by localized refinement and derefinement, is a very efficient tool for enhancing solution accuracy and optimizing computational time. In order to efficiently and effectively adapt a mesh to a solution field, the criteria used for the adaptation process needs to be as accurate as possible. The mesh adaption methods

Figure 1.3: **Left** and **Right** The left and right views of same scene, **Center**: The ground truth disparity map which is required to compute. available at http://vision.middlebury.edu/stereo/data/scenes2006/.

are progressing rapidly. A posteriori error estimation allows us to some what assess the accuracy by using the computed solution itself. The image grids are already well refined and dense, therefore to improve the accuracy of computations and reduce error density we propose a new mesh adaption strategy where a posteriori error estimation techniques have been developed and integrated with mesh refinement strategies. Using our method where the mesh adaption is performed by derived a posteriori error indicators, one can improve the computations by building a good mesh for solution u. All the computations are performed using FreeFem++ [43], where automatic mesh generation and mesh adaption capabilities of of FreeFem++ make the job easier. For detailed information about mesh generation technique and ideas on mesh adaption one can read the given manual of software free available on http://www.freefem.org/ff++/. The figure 1.4 demonstrates our computed solution u obtained from minimizing a nonlinear energy functional with total variation regularizer. We will discuss this functional and our numerical strategy in chapters three and four. The figure shows computed disparity on mesh between a pair of images by our method, moreover adaptive procedure is visualized where disparity is shown on different iterations of adaption on a triangular mesh.

Fields of applications: Mathematical Problems in Image Processing is a ma-

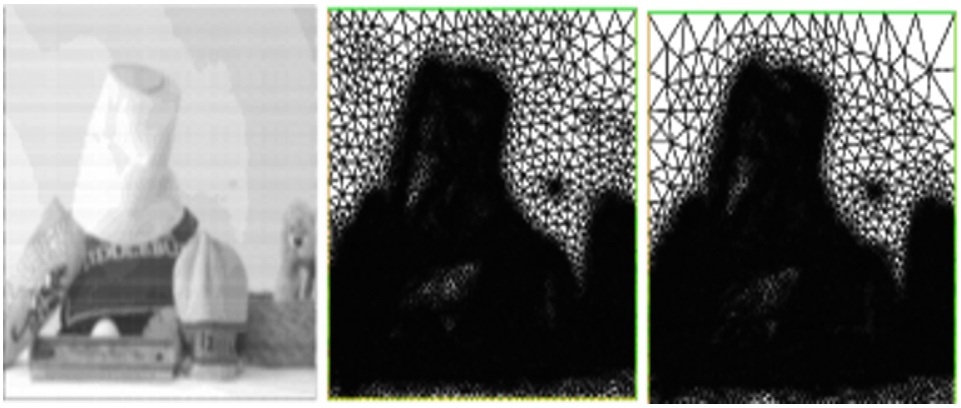

Figure 1.4: **Left** view0 downloaded from http://vision.Middlebury.edu/data/ **Center:** The computed disparity on mesh after first iteration. **Right:** The computed disparity after third iteration of mesh adaption.

jor, elegant and unique contribution to the applied mathematics literature, towards applications in image processing and computer vision. It is surprising when we realize just how much we are surrounded by images. Images allow us not only to perform complex tasks on a daily basis, but also to communicate, transmit information, represent and understand the world around us. Just think, for instance about digital television, medical imagery, video-surveillance,... The tremendous development in information technology accounts for most of this. We are now able to handle more and more data. Many day to day tasks are now fully or partially accomplished with the help of computers. Whenever the images are involved this phenomena can be called Computer Vision [8]. The image sequence analysis is one of the very active research areas of computer vision which is a very useful tool for a variety of different tasks. For example, it allows to distinguish stationary from moving objects and thus to detect and avoid obstacles. This makes it particularly useful for tasks where vehicles have to be guided safely through an unknown environment. In this context one can also either think of robot navigation where one is interested in a fully autonomous behavior or the design of drivers assistance systems where support is only required in certain situations. Moreover, the estimated motion allows to track objects on their way through the scene, to keep them focused and to follow them if desired. This

interaction with the environment goes far beyond a pure avoidance of obstacles. In combination with approaches from machine learning, motion patterns can be trained in such a way that the obtained algorithms even allow for the interpretation of human mimics and gestures. These techniques serve as an important step towards human machine interfaces. In the case of stereo reconstruction one is interested in determining the horizontal depth information between the left and the right frame of a stereo pair, image registration requires to compute the displacement field between two images that may have even been obtained by two different types of image acquisition methods, e.g. computer tomography (CT) and magneto resonance imaging (MRI). Although these above are very few examples to justify the importance of image sequence analysis, how ever they clearly show why in the last two decades so much research has been carried out with respect to the development of accurate models and robust numerical methods for solving computer vision we refer the reader for more dtails in[17].

1.1.2 Variational methods in picture motion

Most of the modern PDE's based methods used for recovery of motion information from an image sequence are expressed in the terms of variational problems where an energy functional is minimized to compute optical flow and disparity map. Minimizing continuous energy functional leads in natural way to partial differential equations(PDEs): applying gradient descent, for instance, yields a systems of coupled diffusion-reaction equations for two flow components u_1 and u_2 in the case of optical flow and a single equation for computation of disparity map u. The fast emerging methods of PDE-based image restoration methods [87, 29], such as nonlinear diffusion filtering and total variation denoising, has motivated many researchers to apply similar ideas to estimate optical flow [90]. The energy functionals mainly consist of two terms: The data term which is derived from optical flow constraints like brightness constancy assumption that corresponding pixels in different frames of an image sequence reveal the same grey value. The second term is called smoothness term which assumes the global or piecewise smoothness of flow field $\mathbf{u}$ or the horizontal disparity map u, more clearly the smoothness term fills in information from regions with existing reliable flow estimates

to the regions where no estimates are possible . Let we denote the data term as $M(\partial^k f)$ where $\partial^k f$ denotes the set of all partial (spatial and temporal) derivatives of f of order k. The smoothness term is denoted as $D(\nabla f, \nabla \mathbf{u})$ where f denotes the image gradient and $\nabla \mathbf{u}$ denotes the flow gradient. Combining the data term and smoothness term the general energy functional is modeled as

General energy Functional:

$$E[\mathbf{u}] = \int_{\Omega} (\underbrace{M(\partial^k f)}_{\textbf{data term}} + \underbrace{\alpha(\mathbf{x}) D(\nabla f, \nabla \mathbf{u})}_{\textbf{smoothness term}}) d\mathbf{x} \tag{1.2}$$

Where $\Omega \subset \mathbb{R}^2$ is domain of integration, $\mathbf{x} = (x_1, x_2)^T$ and $\nabla = (\partial x_1, \partial x_2)$. Here $\alpha(\mathbf{x})$ is given strictly positive continuous function on Ω. The variational techniques can be classified into local methods that optimize some local energy-like expression, and global strategies which attempt to minimize a global energy functional. Examples of the first category include the Lucas-Kanade methods [65], and the structure tensor approach of Bigün and Granlund. [24]. Global approaches comprise the classic method of Horn and Schunck [51] and discontinuity-preserving variant such as [19]. Local methods may offer relatively high robustness under noise, but do not give dense flow fields where as Global methods, on other hand, yield flow fields with high accuracy but are known to be more sensitive to noise [19]. Their success is mainly due to the fact that the energy functional express the data constraints(constancy) and incorporates a regularization term to cope with the aperture problem and to recover a fully dense flow filed. The major drawback of the variational methods is the reliability of the computed optic flow at all locations. In fact, the regularization term supply to the problem of incomplete data to obtain a fully dense flow but, given a location, one cannot say a priori if the computed field comes from the satisfaction of the constraints or only from the fill in effect of the regularization. To circumvent this difficulty to apply variational methods, we propose some new confidence measures to identify the locations where the problem of incomplete data has been solved successfully. The almost used confidence measure is based on the magnitude and gradient of the image [12]. Recently an energy based confidence measure was introduced in [19, 16]. The question of building such confidence measures should be considered in a more general setting to observe the role of

effects of regularization solving ill-posed problems. Nevertheless, when the regularization procedure is based on some Tikhonov regularization [42, 85], one can think about the adaptive discretization strategies, where a refinement process relies both to the standard discretization and the regularization parameters which could be an efficient way to measure, and as far as possible to control, the effects of such regularization. Aim of this thesis is not to introduce a new variational model but to show that how the proposed control of regularization in a general setting increases the efficiency of existing nonlinear variational models. On other hand this thesis also contributes in providing a theoretical framework from direct calculus of variation for nonlinear class of regularization methods for optical flow methods, we prove that they have a unique solution that depends in a continuous way on the given data.

Ill-posdness and role of smoothing: Determination of optical flow yields an ill-posed problem which allows only to compute the optical flow component normal to image edges, this ill-posdness is due to aperture problem. To overcome the ill-posdness for variational optical flow methods, image community use smoothing techniques and smoothness assumptions: where the image sequences are pre-smoothed prior to differentiation in order to remove noise and to stabilize the differentiation process. Local methods use spatial constancy assumptions on the optical flow field in the case of the Lucas-Kanade method [65], and spatiotemporal constancy for Bigün method [24]. Global approaches on other hand supplement the optical flow constraint with a regularization term[51]. Third approach is combined local-global (CLG) methods by Andrés Bruhn and Joachim Weickert [19] which combines both the local and global approaches and is robust under noise and gives dense flow fields.

Smoothing: Let we consider an image sequence $g(x_1, x_2, t)$ where (x_1, x_2) denotes the location within a rectangular image domain Ω, and $t \in [0, T]$ denotes time. It is common to smooth image sequence prior to differentiation [25, 19] by convolving each frame with some Gaussian $K_\sigma(x_1, x_2)$ of standard deviation σ:

$$f(x_1, x_2, t) := (K_\sigma * g)(x_1, x_2, t).$$

The low-pass effect of Gaussian convolution attenuate high frequencies and removes the noise.

Constancy assumption: Many PDEs based methods for optic flow are based on the assumption that grey values of image objects in subsequent frames do not change over the time:

$$f(x_1 + u_1, x_2 + u_2, t + 1) = f(x_1, x_2, t) \tag{1.3}$$

where the displacement field (u_1, u_2) is called optic flow. Performing first order Taylor expansion yields optic flow constraint. Obviously unique determination of two unknowns u_1, u_2 (aperture problem) is not possible from single equation. For non vanishing image gradients, it is only possible to determine the flow component parallel to $\nabla f := (f_{x_1}, f_{x_2})^T$, i.e normal to the edges. This is so called normal flow is given by

$$w_n = -\frac{f_t}{|\nabla f|}\frac{\nabla f}{|\nabla f|}$$

1.1.3 Some classical variational approaches in image motion

To overcome the difficulty to solve aperture problem, Lucas and Kanade [65] proposed the strategy to determine two components u_1 and u_2 at some location (x_1, x_2, t) using weighted least square fit by minimizing the function

$$E_{LK}(u_1, u_2) := K_\rho * ((f_{x_1} u_1 + f_{x_2} u_2 + f_t)^2) \tag{1.4}$$

Here the standard deviation ρ of the Gaussian serves as an integration scale over which main contribution of the least square fit is computed, moreover they proposed to assume that the unknown optic flow vector is constant with in some neighborhood of size ρ. A minimum (u_1, u_2) of E satisfies $\partial_{u_1} E = 0$ and $\partial_{u_2} E = 0$.

In the framework of regularization Horn and Schunck [51] have pioneered this class of global differential methods. They determined the unknown functions u_1 and u_2 as minimizers of the global energy functional

$$E_{HS}[u_1, u_2] = \int_\Omega ((f_{x_1} u_1 + f_{x_2} u_2 + f_t)^2) + \alpha(|\nabla u_1|^2 + |\nabla u_2|^2)) \tag{1.5}$$

where $\alpha > 0$ is a regularization parameter, the regularizer $|\nabla u_1|^2 + |\nabla u_2|^2$ fills in information from the neighborhood. This results in the dense flow field. In 2004 Andrés Bruhn and Joachim Weickert extended the Horn and Schunck approach by

combining the local and global approaches. They proposed CLG variational approach [19] as

$$E_{CLG}[u_1, u_2] = \int_\Omega ((\mathbf{u}^T J_\rho(\nabla_3 f)\mathbf{u}) + \alpha(|\nabla u_1|^2 + |\nabla u_2|^2)) \tag{1.6}$$

where the matrix $J_\rho(\nabla_3 f)$ is structure tensor will be discussed in detail in coming chapters. $\mathbf{u} := (u_1, u_2, 1)^T$ and $\nabla_3 f = (f_{x_1}, f_{x_2}, f_t)^T$. Recently this above model (1.6) is brought in to consideration by Z.Blehachmi and F.Hecht in 2009 and slightly modified as

$$E_{CLG}[u_1, u_2] = \int_\Omega ((\mathbf{u}^T J_\rho(\nabla_3 f)\mathbf{u}) + \alpha(\mathbf{x})(|\nabla u_1|^2 + |\nabla u_2|^2)) \tag{1.7}$$

where $\alpha(\mathbf{x})$ is scalar valued strictly positive continuous function of space, they proposed an adaptive approach for the above problem where the function $\alpha(\mathbf{x})$ play a crucial role in computational procedure. As so far the Lucas-Kanade and Horn Shunck approaches are linear methods that are based on quadratic optimization. To cope with the results at the locations with flow discontinuities and extending the above approaches to more robust against outliers in both the data and smoothness term a non-quadratic and approach was proposed by [19], where TV regularization is used. They proposed following energy functional to minimize

$$E_{NL}[u_1, u_2] = \int_\Omega (\psi_1(\mathbf{u}^T J_\rho(\nabla_3 f)\mathbf{u}) + \alpha\Psi_2(|\nabla u_1|^2 + |\nabla u_2|^2) \tag{1.8}$$

where $\psi_1(s^2)$ and $\psi_2(s^2)$ are non quadratic penalizers and $\psi_i(s^2) = 2\beta_i^2\sqrt{1 + \frac{s^2}{\beta^2}}$ for $i = 1, 2$ β is a small regularization parameter.

Rest of our thesis is organized as follows.

In chapter two we start with optic flow problem. We extend the work given in presentation [12], and propose a linear variational model using complementary optic flow approach. The minimization of energy functional yields Euler's Lagrange equations, from where we calculate variational formulation for the given continuous problem, which is then numerically discretized to compute optic flow from the given image sequences. Last and crucial part of this chapter is devoted to derive a posteriori error indicators for the given discretized problem, and the adaptive algorithm. Finally we complete the second chapter with our numerical computations, where we consider three

different examples from the real world image sequences.

Third chapter is devoted to the mathematical modeling and analysis of stereo vision problem, here we design the data term from constancy of grey value assumption but the motion is considered as one dimensional shift between left view and right view from two different cameras, the second part of the energy functional is smoothness term which in our case is the total variation regularizer. The second part of the chapter three is based on analysis of variational model in the framework of classical results direct from the calculus of variation, where the convexity and weak convergence is discussed, moreover using the well known results from calculus of variation we write the Euler-Lagrange equation for the given energy functional. The third part goes to the weak formulation of Euler-Lagrange equation obtained from minimizing the given energy functional.

The chapter four is dedicated to numerical analysis, and scientific computations for the given stereo TV model. We give discretization of continuous weak problem for stereo case given in the chapter three, here we also discuss the well-posdness of the discrete as well as the continuous weak problems. In second part of this chapter we derive a priori and a posteriori error estimates in appropriate norms. We finalize the theoretical discussions in this chapter with our adaptive algorithm as discussed for the optic flow problem in chapter two. Finally we present our scientific computational results obtained from three different numerical experiments.

Chapter five is dedicated to scientific computations for nonlinear optical flow problems using total variational regularization approach. Following the similar pattern as discussed in last chapters we write Euler-Lagrange equations, weak formulation, discretized problem, define a posteriori estimates and use same mesh adaption algorithm. At last we present our computational results for these nonlinear models.

Chapter six is devoted to image denoising problem where we discuss the Perona-Malik diffusion equation and propose an adaptive algoritm for time-dependent denoising problem and end the chapter with numerical results. The second part of this chapter is given as appendix A, where we discuss a finite difference method for Perona-Malik equation.

Chapter 2

Local and Adaptive selection of the Regularization Parameters for Linear Models of Optic Flow Problem

2.1 Introduction

The computation of the two dimensional velocity field between subsequent frames of a video sequence is classical image analysis problem and one of the active research areas in computer vision research, image community is very much attracted to this research area [3, 4, 5, 22, 16, 18, 19, 51, 55, 59, 65, 71, 72, 79]. This velocity field is called is called optic flow, in other words optic flow is a dense vector field which associates one displacement vector to each pixel in the image plane. Reliable computation of this displacement field constitutes one challenging task in computer vision research. Mostly the well founded optic flow methods use constancy assumptions on the image features such as, the brightness constancy assumption, gradient constancy assumption and smoothness assumption. In general these assumptions are not sufficient for the determination of optic flow and yield an ill-posed problem, which allows only for the determination of the component normal to the image edges, we refer the reader to review in [18, 17, 79] and references there in.

The PDE's based approach is one of the modern and the most efficient approaches proposed to overcome the ill-posed problems in image sequence analysis [3, 18, 19, 5, 6, 53, 90, 80]. Considering a variational approach one calculates the flow field as a minimizer of a suitable energy functional. The success of variational approach in vision problems is mainly due to the fact that the energy functional consists of a data term based on constraints (constancy assumptions), e.g. grey value constancy in Horn and Schunck model [51] and a regularization term which penalizes fluctuations in the flow field and cope with the aperture problem to recover a fully dense flow field. However there is an ambiguity that these two terms may contradict each other, to circumvent this difficulty a novel approach was proposed as complementary optical flow [52] where they have focused on improvements in data term(constancy assumptions) and smoothness term to create complementarity between these two terms. In this chapter we extend the variational method recently appeared in [12], by improving the data term in their variational model in the spirit of [52].

We follow the novel regularization technique proposed in [12] with a modification in the data term and show that how the regularization effects play a crucial role in

the solutions of ill-posed problems [39, 40, 85]. Though the regularization approach in ill-posed problems is a vast field to discuss, specially when the regularization approach is Tikhonov based [39, 40, 85], we think about the adaptive discretization strategies, where a refinement process relies both on the standard discretization and the optimal choice of the regularization parameters to control the effects of such a regularization.

An adaptive finite element method is used to compute the optic flow which includes an implicit confidence measure. The adaptation is performed using a posteriori error indicators as discretization error in an appropriate norm. The scaling factors in the error indicators serve as the local regularization parameters. Goal of this presentation is not only to provide an efficient and accurate method to solve optic flow problems but also to show that how the error indicators constitute a natural confidence measure. To show the robustness of adaptive procedure we build a good "mesh" for the optic flow at every adaptive iteration of given adaptive algorithm. The method should also work with finite difference based discretization but our choice is related to the fact that the analysis and the adaptive process are more flexible in the framework of finite element methods.

2.2 Variational optic flow problem

The vector field (u_1, u_2) describes the "motion" in a given sequence of an image is called optical flow. Given a domain $\Omega \in \mathbb{R}^2$ and a function $f : \Omega \times \mathbb{R} \longrightarrow \mathbb{R}$ modeling a sequence of frames of an image. The estimation of optical flow is based on the image brightness constancy assumption which states that the apparent brightness $f(x_1, x_2, t)$ at position (x_1, x_2) and time t of moving object when it moves by a small vector $(\partial x_1, \partial x_2)$ in short time ∂t remains constant over time. This reads:

$$f(x_1, x_2, t) = f(x_1 + \partial x_1, x_2 + \partial x_2, t + \partial t) \tag{2.1}$$

First order Taylor expansion yields

$$f(x_1 + \partial x_1, x_2 + \partial x_2, t + \partial t) = f(x_1, x_2, t) + \frac{\partial f}{\partial x_1} dx_1 + \frac{\partial f}{\partial x_2} dx_2 + \frac{\partial f}{\partial t} dt \tag{2.2}$$

From (2.1) and (2.2) we have

$$\frac{\partial f}{\partial x_1}\frac{dx_1}{dt} + \frac{\partial f}{\partial x_2}\frac{dx_2}{dt} + \frac{\partial f}{\partial t} = 0 \tag{2.3}$$

For small displacements, if we assume $f \in C^1([0,\infty);\mathbb{R}^2)$, then from (2.3) we are led to consider the following problem:

Find the displacement field $u_1(x_1,x_2)$, $u_2(x_1,x_2)$, such that

$$f_t + f_{x_1}u_1 + f_{x_2}u_2 = 0 \tag{2.4}$$

The vector field (u_1,u_2) is called the optic flow.

The principle of the variational approach is to determine $\mathbf{u} = (u_1,u_2)$ as the minimizer of a given energy functional. This functional consists of two parts: a data term which is derived from (2.4) and a regularization term due to the fact that the first part does not yield a well-posed problem. We refer the reader to [18, 19, 17] and the references therein for a complete review of the various variational models. In what follows, we will consider a linear model called the combined local global approach [12, 19] with modified data term using the normalizing approach from [52], where one may review the detailed discussion on the normalization of data term and complementarity between smoothness term and data.

We consider the following energy functional associated with the optic flow recovery by variational methods

$$E(\mathbf{u}) = \int_\Omega \left(\frac{1}{|\mathbf{grad}\, f|^2 + \zeta^2}(\mathbf{u}^T J_\varrho \mathbf{u}) + \alpha(\mathbf{x})\,|\nabla \mathbf{u}|^2 \right) d\mathbf{x} + \int_\Omega \frac{1}{|\mathbf{grad}\, f|^2 + \zeta^2}\mathbf{f}\cdot\mathbf{u}\, d\mathbf{x} \tag{2.5}$$

where α is a given, strictly positive scalar valued, continuous function on Ω. Accordingly, we consider a disjoint partition into a finite number of subdomains Ω_l such that the function α is equal to α_l on each Ω_l. we assume that $\alpha_{min} > 0$.

The variational optic flow problem consists of: find $\mathbf{u}(\Omega)$ such that

$$E\mathbf{u} = \inf E(\mathbf{v}) \tag{2.6}$$

We denote by J_ϱ the matrix $K_\varrho * (\mathbf{grad} f)(\mathbf{grad} f)^T$, where we use the spatial gradient $(\frac{\partial}{\partial x_1}, \frac{\partial}{\partial x_2})$

$$J_\varrho = \begin{pmatrix} K_\varrho * f_{x_1}^2 & K_\varrho * f_{x_1} f_{x_2} \\ K_\varrho * f_{x_1} f_{x_2} & K_\varrho * f_{x_2}^2 \end{pmatrix}.$$

and $K_\varrho(x, y)$ is a Gaussian kernel with standard deviation ϱ, $*$ stands for convolution. For sake of simplicity we introduce data normalization parameter denoted as θ, where

$$\theta = \frac{1}{|\mathbf{grad}\, f|^2 + \zeta^2}$$

the regularization parameter $\zeta > 0$ avoids division by zero. Given a vector field $\mathbf{v}$ we denote

$$\mathbf{grad(v)} = \begin{pmatrix} \frac{\partial v_1}{\partial x_1} & \frac{\partial v_1}{\partial x_2} \\ \frac{\partial v_2}{\partial x_1} & \frac{\partial v_2}{\partial x_2} \end{pmatrix}$$

We set $\mathbf{f} = (-\theta f_{x_1} f_t, -\theta f_{x_2} f_t)^T$, and $\mathbf{u} = (u_1, u_2)^T$, where f_{x_1}, f_{x_2} and f_t stands for the derivatives with respect to x_1, x_2 and t. For the sake of brevity we will denote by $\mathbf{u}^T\, \theta\, J_\varrho \mathbf{u}$, $\theta\, J_\varrho \mathbf{u}^2$ or $|\theta\, J_\varrho^{\frac{1}{2}} \mathbf{u}|^2$ the product $(\theta\, J_\varrho \mathbf{u}, \mathbf{u})$ where $(.,.)$ is the scalar product in $\mathbb{R}^2$.

We work in H^1 functional space for other possible choices we refer the reader to [12]. We assume that the functional space H^1 as a Hilbert space for the scalar product

$$(\mathbf{u}, \mathbf{v})_\varrho = \int_\Omega \mathbf{grad}\ \mathbf{u} : \mathbf{grad}\ \mathbf{u} d\mathbf{x} + \int_\Omega \theta J_\varrho \mathbf{u} \cdot \mathbf{v} d\mathbf{x}.$$

equipped with the norm

$$\|\mathbf{u}\|_{H^1_\varrho(\Omega)} = (\mathbf{u}, \mathbf{u})_\varrho^{\frac{1}{2}}$$

Proposition 2.1 . Problem (2.6) admits a weak solution $\mathbf{u}_\alpha$ in $H^1(\Omega)$.

When Ω and $\mathbf{f}$ are smooth, additional regularity could be proved for the solution $\mathbf{u}_\alpha$. For instance, with Lipschitz-continuous, $\mathbf{f} \in H^1(\Omega)$ the following regularity result holds [[13], Proposition 2.5] and [[12],Proposition 2.3].

Proposition 2.2. There exists a constant $c > 0$ only depending on the geometry of Ω such that a weak solution $\mathbf{u}_\alpha$ of problem (2.6) belongs to $H^{s+1}(\Omega)$, for all real numbers $s < s_0$, where s_0 is given by

$$s_0 = \min\left\{\frac{1}{2}, c\left|\log\left(1 - \frac{\alpha_{min}}{\alpha_{max}}\right)\right|\right\}$$

The Euler-Lagrange equations are given by:

$$\begin{cases} \operatorname{div}\left(\alpha(\mathbf{x})\,\mathbf{grad}\,u_1\right) - \left(\theta\, f_{x_1}^2 u_1 + \theta\, f_{x_1} f_{x_2} u_2 + \theta\, f_{x_1} f_t\right) = 0 \,\text{in}\,\Omega \\ \operatorname{div}\left(\alpha(\mathbf{x})\,\mathbf{grad}\,u_2\right) - \left(\theta\, f_{x_1} f_{x_2} u_1 + \theta\, f_{x_2}^2 u_2 + \theta\, f_{x_2} f_t\right) = 0 \,\text{in}\,\Omega \\ \frac{\partial u_1}{\partial n} = \frac{\partial u_2}{\partial n} = 0, \text{ on } \partial\Omega \end{cases} \tag{2.7}$$

Remark 2.3. (1) If Ω is not smooth, the Neumann condition on the boundary should be understood in the weak sense. (2) In the usual optic flow models [17, 18] $\alpha(\mathbf{x})$ is taken constant in the whole domain. Since we intend to perform an adaptive strategy both in h and α we have to consider a piecewise constant function. Ideally, α is constant at each level of the refinement process which means that the decomposition of Ω into sub-domains is generated dynamically during the computations. For the sake of simplicity, we will assume it known a priori.

The weak formulation of (2.7) reads:

$$\begin{cases} \text{Find } \mathbf{u} \in H^1(\Omega) \text{ such that} \\ \int_\Omega \alpha(\mathbf{x}) \nabla\mathbf{u} : \nabla\mathbf{v}\, d\mathbf{x} + \int_\Omega \theta\, J_\varrho \mathbf{u}\cdot\mathbf{v}\, d\mathbf{x} = \int_\Omega \theta\, \mathbf{f}\cdot\mathbf{v}\, d\mathbf{x}\ \forall \mathbf{v} \in H^1(\Omega) \end{cases} \tag{2.8}$$

We introduce the notations: for $\mathbf{u}, \mathbf{v} \in H^1(\Omega)$

$$a_\alpha(\mathbf{u},\mathbf{v}) = \int_\Omega \alpha(\mathbf{x}) \nabla\mathbf{u} : \nabla\mathbf{v}\, d\mathbf{x} + \int_\Omega \theta\, J_\varrho \mathbf{u}\cdot\mathbf{v}\, d\mathbf{x} \tag{2.9}$$

$$(\mathbf{f},\mathbf{v}) = \int_\Omega \theta\, \mathbf{f}\cdot\mathbf{v}\, d\mathbf{x}$$

Thus, problem (2.8) consists of finding $\mathbf{u} \in H^1(\Omega)$, such that:

$$a_\alpha(\mathbf{u},\mathbf{v}) = (\mathbf{f},\mathbf{v})\ \ \forall \mathbf{v} \in H^1(\Omega)$$

In order to obtain the error estimates with constants independent of α, we introduce the norm:

$$\|\mathbf{u}\|_{\varrho,\alpha}^2 = \left|\alpha^{\frac{1}{2}}\,\mathbf{grad}\,\mathbf{u}\right|_{L^2(\Omega)}^2 + \left\|\theta^{\frac{1}{2}}\, J_\varrho^{\frac{1}{2}}\mathbf{u}\right\|_{L^2(\Omega)}^2$$

For the a posteriori analysis purpose, we will assume that the matrix J_ϱ is definite a.e. In addition, to avoid inessential technicalities in the discretization we assume that Ω is a polygonal domain.

Remark 2.4. Note that for nonsmooth domains, we may proceed by approximation in

the spirit of [14]. The nonsmooth parts are approximated by smooth neighborhoods on which the regularization parameter goes to zero. We recall the the following estimates proved in [proposition 2.6, [12]]

Proposition 2.5 . Let $\mathbf{u} \in H^1(\Omega)$ be a solution of problem (2). For $\alpha > 0$, the following inequalities hold [[12], Proposition 2.6]

$$\|\mathbf{u}_\alpha\|_{\varrho,\alpha} \leq C \left\| (\theta\, J_\varrho)^{\frac{1}{2}} \mathbf{u} \right\|_{L^2(\Omega)}, \tag{2.10}$$

and

$$\|\mathbf{u} - \mathbf{u}_\alpha\|_{\varrho,\alpha} \leq C \left(\frac{\alpha_{max}}{\alpha_{min}} \right)^{\frac{1}{2}} \left| \alpha^{\frac{1}{2}} \mathbf{gradu}_\alpha \right|_{L^2(\Omega)}, \tag{2.11}$$

With constant C independent of α.

Note that we are only interested here in the behavior of $\mathbf{u}_\alpha$ as the ratio $\frac{\alpha_{max}}{\alpha_{min}}$ is large because we intend to adapt locally the choice of the regularization parameters α.

2.3 Problem Discretization

Suppose that the domain Ω is polygonal and let we consider a regular family of triangulations $\mathcal{T}_h$ made up of elements which are triangles (or quadrilaterals) with maximum size $h > 0$, satisfying the usual admissibility assumptions, i.e:

Admissibility: the intersection of two different elements is either empty, a vertex, or a whole edge.

Shape regularity: The ratio of the diameter of any element $T \in \mathcal{T}_h$ to the diameter of its largest inscribed ball is bounded by a constant σ independent of T and h.

$$X_h := \left\{ \mathbf{v}_h \in C(\bar{\Omega}) | \forall K \in \mathcal{T}_h, \mathbf{v}_{h|T} \in P_1(K)^2 \right\}$$

We denote by $J_{\varrho,h}$ a finite element approximation of the matrix $J_{\varrho,h}$ obtained as follows: for any $K \in \mathcal{T}_h$ we denote by $J_{\varrho,h,K}$ the matrix where the coefficients.

$$(\theta J_{\varrho,h;K})_{i,j} = \theta_K \, \frac{1}{|K|} \int_K (J_\varrho)_{i,j} \, d\mathbf{x}, \; 1 \leq i,j \leq 2$$

are the mean values of the coefficients of J_ϱ on K. The matrix $J_{\varrho,h}$ is the piecewise constant matrix which take the value $J_{\varrho,h;K}$ on the element K.

We denote by $a_{\alpha,h}$ the bilinear form a_α, where J_ϱ is replaced by $J_{\varrho,h}$.

The discrete problem reads

$$\begin{cases} \text{Find } \mathbf{u}_{\alpha,h} \in X_h \text{ such that} \\ a_{\alpha,h}(\mathbf{u}_h, \mathbf{v}_h) = (\mathbf{f}, \mathbf{v}_h) \qquad \forall \mathbf{v}_h \in X_h \end{cases} \tag{2.12}$$

Under the assumption of the definiteness of J_ϱ, the ellipticity of the bilinear form $a(\cdot;\cdot)_{\alpha,h}$ holds. Applying the Lax-Milgram Lemma, we have

Proposition 2.6 For any $\alpha > 0$ there exists a unique solution $\mathbf{u}_{\alpha,h}$ of the discrete problem (2.12)

Cea's Lemma implies:

$$\|\mathbf{u}_\alpha - \mathbf{u}_{\alpha,h}\|_\alpha \leq C \left(\inf_{\mathbf{v}_h \in X_h} \|\mathbf{u}_\alpha - \mathbf{v}_h\|_\alpha + \sup_{\mathbf{w}_h \in X_h} \frac{(a_\alpha - a_{\alpha,h})(\mathbf{v}_h, \mathbf{w}_h)}{\|w_h\|} \right) \tag{2.13}$$

We denote by Π_h the orthogonal projection from $H^1(\Omega)$ onto X_h for the norm $\|\cdot\|_\alpha$.

Proposition 2.7. For any real number s with $1 \leq s \leq 2$ there exists a constant C which neither depends on h nor on α such that for any $\mathbf{v} \in \left(\bigcup_{l=1}^L H^s(\Omega_l) \cap H^1(\Omega)\right)$, the following two error estimates hold [[12] A.3 and A.4]

$$\|\mathbf{v} - \Pi_h^\alpha \mathbf{v}\|_\alpha \leq C \sum_{l=1}^L \sqrt{\alpha_l} h_l^{s-1} \|\mathbf{grad}\, \mathbf{v}\|_{H^{s-1}(\Omega_l)} \tag{2.14}$$

$$|(a_\alpha - a_{\alpha,h})(\mathbf{v}_h, \mathbf{w}_h)| \leq \lambda_{\min(\theta\, J_\varrho)}^{\frac{-1}{2}} h\, |\theta\, J_\varrho|_{W^{1,\infty}(\Omega)} \|\mathbf{v}_\alpha\|_\alpha \|\mathbf{w}_h\|_\alpha \tag{2.15}$$

Assembling these estimates yields

Theorem 2.8. Assume that J_ϱ belong to $W^{1,\infty}(\Omega)$, and the solution u_α of (2.8) belongs to $\left(\bigcup_{l=1}^L H^2(\Omega_l) \cap H^1(\Omega)\right)$. There exists a constant C, which neither depends on h nor on α such the following estimate holds

$$\|u_\alpha - u_{\alpha,h}\|_{\alpha,\varrho} \leq C \sum_{l=1}^L \sqrt{\alpha_l} h_l \|u_\alpha\|_{H^2(\Omega_l)} \tag{2.16}$$

2.4 The confidence measure by residual error indicator

For the a posteriori error estimates we assume that $\mathbf{f} \in L^2(\Omega)^2$ and we fix $\mathbf{f}_h$ a finite element approximation of $\mathbf{f}$ associated with $\mathcal{T}_h$. We also fix a finite element approxi-

mation $\tilde{J}_{\varrho,h}$ of J_ϱ. For $K \in \mathcal{T}_h$, we denote by $\mathcal{E}_K$ the set of its edges not contained in the boundary $\partial\Omega$. The union of all $\mathcal{E}_K$, $K \in \mathcal{T}_h$ is denoted by $\mathcal{E}_h$. With each edge $e \in \mathcal{E}_h$, we associate a unit vector $\mathbf{n}_e$ normal to e and we denote by $[\phi]_e$ the jump of the piecewise continuous (vector valued) function ϕ across e in the direction $\mathbf{n}_e$. For each $K \in \mathcal{T}_h$ we denote by h_K the diameter of K and we denote by h_e the diameter of $e \in \mathcal{E}_K$. We define the residual error indicators [88] as follows:

For each element $K \in \mathcal{T}_h$, we set

(2.17)

$$\eta_K = \alpha_K^{-\frac{1}{2}} h_K \left\| \mathbf{f}_h + \alpha_K \Delta \mathbf{u}_h + \tilde{J}_{\varrho,h} \mathbf{u}_h \right\|_{L^2(K)^2} + \frac{1}{2} \sum_{e \in \mathcal{E}_K} \alpha_e^{-\frac{1}{2}} h_e^{\frac{1}{2}} \left\| [\alpha \mathbf{gradu}_h \cdot n_e]_e \right\|_{L^2(e)^2}$$

where $\alpha_e = \max(\alpha_{K_1}, \alpha_{K_2})$, K_1 and K_2 being the two elements adjacent to e.

2.4.1 An upper bound for the error:

For $K \in \mathcal{T}_h$ we denote by $\mathcal{N}(K)$ the set of its vertices. Let $\mathcal{N}_h = \cup_{K \in \mathcal{T}_h} \mathcal{N}(K)$ be the set of all vertices in $\mathcal{T}_h$. We denote by $\mathcal{N}_{h,\Omega}, \mathcal{N}_{h,\Gamma_N}$ the set of all vertices in Ω, and on Γ_N respectively. For any $K \in \mathcal{T}_h, e \in \mathcal{E}_h$ and $x \in \mathcal{N}_h$ we denote by

ω_K the union of all elements sharing an edge e with K,

$\tilde{\omega}_K$ the union of all elements sharing at least a vertex x with K,

ω_e the union of all elements having e as an edge,

$\tilde{\omega}_e$ the union of all elements sharing at least one vertex with e,

ω_x the union of all elements having x as a vertex.

We define the quasi-interpolation operator of Clement type $\mathcal{I}_h$ by

$$\mathcal{I}_h \phi = \sum_{x \in \mathcal{N}_{h,\Omega} \cup \mathcal{N}_{h,\Gamma_\mathcal{N}}} \pi_x \varphi \lambda_x$$

where

$$\varphi_x \phi = \frac{1}{|\omega_x|} \int_{\omega_x} \varphi \, dx$$

is the mean value of φ on ω_x and λ_x the barycentric coordinate associated to x. For vector-valued functions, $\mathcal{I}_h$ is defined by applying it to the components of the function.

In particular, $\mathcal{I}_h\mathbf{v} \in X_h$ for all $\mathbf{v} \in L^2(\Omega)$. For any $\mathbf{v} \in H^1(\Omega)$, $K \in \mathcal{T}_h$ and $e \in \mathcal{E}_h$, following the argument of [88], one can prove the following interpolation error estimates

$$\begin{aligned} \|\mathbf{v} - \mathcal{I}_h\mathbf{v}\|_{L^2(K)} &\leq c_1 h_K \alpha_K^{-\frac{1}{2}} \|\mathbf{v}\|_{\alpha,\tilde{\omega}_K} \\ \|\mathbf{v} - \mathcal{I}_h\mathbf{v}\|_{L^2(e)} &\leq c_1 h_K^{\frac{1}{2}} \alpha_e^{-\frac{1}{2}} \|\mathbf{v}\|_{\alpha,\tilde{\omega}_K} \end{aligned} \tag{2.18}$$

c_1, c_2 are constants depending only on the shape parameter.

Proposition 2.9 For all $K \in \mathcal{T}_h, e \in \mathcal{E}_h$ and for all $\mathbf{v} \in X_\varrho$ there exist $\mathbf{v}_h \in X_h$ and constants c and c', independent of h_K and α such that the following estimates hold [[12], Proposition 4.1]

$$\begin{aligned} \left\|(\theta J_\varrho)^{\frac{1}{2}}\mathbf{v} - \mathcal{I}_h\mathbf{v}\right\|_{L^2(K)} &\leq c_1 h_K \alpha_K^{-\frac{1}{2}} \|\mathbf{v}\|_{\alpha,\tilde{\omega}_K} \\ \left\|(\theta J_\varrho)^{\frac{1}{2}}\mathbf{v} - \mathcal{I}_h\mathbf{v}\right\|_{L^2(e)} &\leq c_2 h_K^{\frac{1}{2}} \alpha_e^{-\frac{1}{2}} \|\mathbf{v}\|_{\alpha,\tilde{\omega}_K} \end{aligned} \tag{2.19}$$

$$\left(\sum_{K\in\mathcal{T}_h} h_K^2 \left\|(\theta J_\varrho)^{\frac{1}{2}}\mathbf{u}_h\right\|^2_{L^2(K)}\right) \leq \frac{1}{2}\sum_{K\in\mathcal{T}_h} \alpha_K \left(\eta_K^2 + h_K^2\alpha_K^{-1}\|\mathbf{f} - \mathbf{f}_h\|^2_{L^2(K)}\right)$$

The constants c, c' are depending on $\lambda_{\min}((\theta J_\varrho)^{\frac{1}{2}})$ the lowest eigenvalue of $(\theta J_\varrho)^{\frac{1}{2}}$ and $\max_{ij,k}\left|((\theta J_\varrho)^{\frac{1}{2}})_{ij,k}\right|$ where we denote $(\theta J_\varrho^{\frac{1}{2}})_{ij,k}$ the derivative of the coefficient $((\theta J_\varrho)^{\frac{1}{2}})_{ij}$ with respect to the variable $x_k,\ k = 1, 2..$.

From the continuity of the interpolation operator, we have

$$\|\mathbf{v}_h\|^2_{L^2(K)} \leq \|\mathbf{v}\|^2_{L^2(\tilde{w}_K)}$$

Assembling all these estimates yield

Theorem 2.10. There exists a constant C which is independent of h and α such that the following estimate holds

$$\|\mathbf{u}_\alpha - \mathbf{u}_{\alpha,h}\| \leq C\left(1 + \frac{\alpha_M}{\alpha_m}\right)^{\frac{1}{2}} \left(\sum_{K\in\mathcal{T}_h} \eta_K^2 + h_K^2\alpha_K^{-1}\|\mathbf{f} - \mathbf{f}_h\|^2_{L^2(K)}\right)^{\frac{1}{2}} \tag{2.20}$$

Combining (2.17) and (2.10) we obtain

Corollary 2.11 Let $\mathbf{u}$ be a solution of problem (2.4). There exists a constant C which is independent of h and α such that the following estimate holds

(2.21)

$$\|\mathbf{u} - \mathbf{u}_{\alpha,h}\| \leq C\left(1 + \frac{\alpha_{max}}{\alpha_{min}}\right)^{\frac{1}{2}} \left(\sum_{K\in\mathcal{T}_h} \eta_K^2 + h_K^2\alpha_K^{-1}\|\mathbf{f} - \mathbf{f}_h\|^2_{L^2(K)} + \alpha_K^{\frac{1}{2}}\|\mathbf{grad}\,\mathbf{u}_\alpha\|^2_{L^2(K)}\right)^{\frac{1}{2}}$$

The meaning of inequality (2.21) is the following: For each element $K \in \mathcal{T}_h$, we define a new error indicator

$$\tilde{\eta}_K = \eta_K + \alpha_K^{\frac{1}{2}} \left\| \mathbf{grad}\, \mathbf{u}_{\alpha,h} \right\|_{L^2(K)} \tag{2.22}$$

Then we have an upper bound for the error between an $H^1(\Omega)$ solution of the initial problem (without regularization) and the discrete regularized solution. This upper bound furnishes a natural confidence measure and allows for an optimal choice of α. In case we use an affine finite elements discretization, the new term $\alpha_K^{\frac{1}{2}-\epsilon} \left\| \mathbf{grad}\, \mathbf{u}_{\alpha,h} \right\|_{L^2(K)}$ behaves like $\alpha_K^{\frac{1}{2}} h_K$ and consistent with η_K.

2.4.2 An upper bound for the indicator.

We take as a test function $\mathbf{w} \in X_\varrho$ in (2.8)

$$\int_\Omega \alpha(\mathbf{x})\, \mathbf{grad}\, (\mathbf{u} - \mathbf{u}_h) : \mathbf{grad}\ \mathbf{w}\, d\mathbf{x} + \int_\Omega \theta J_\varrho \mathbf{u} \cdot \mathbf{w}\, d\mathbf{x} =$$

$$\int_\Omega \mathbf{f} \cdot \mathbf{w}\, d\mathbf{x} - \int_\Omega \alpha(\mathbf{x})\, \mathbf{grad}\, \mathbf{u}_h : \mathbf{grad}\, \mathbf{w}\, d\mathbf{x} + \int_\Omega \theta J_\varrho \mathbf{u}_h \cdot \mathbf{w}\, d\mathbf{x}$$

Integrating by parts yields

$$\int_\Omega \alpha(\mathbf{x})\, \mathbf{grad}\, (\mathbf{u} - \mathbf{u}_h) : \mathbf{grad}\ \mathbf{w}\, d\mathbf{x} + \int_\Omega \theta J_\varrho (\mathbf{u} - \mathbf{u}_h) \cdot \mathbf{w}\, d\mathbf{x} = \tag{2.23}$$

$$\sum_{K \in \mathcal{T}_h} \Big(\int_K \mathbf{f} + \alpha_K \theta J_\varrho \Delta \mathbf{u}_h + \theta J_\varrho\, \mathbf{u}_h) \cdot \mathbf{w}\, d\mathbf{x} - \frac{1}{2} \sum_{e \in \mathcal{E}_K} \int_e [\alpha_K\, \mathbf{grad}\, \mathbf{u}_h \cdot \mathbf{n}] : \mathbf{grad}\, \mathbf{w}\, d\tau +$$

$$\int_K (\mathbf{f} - \mathbf{f}_h) \cdot \mathbf{w}\, d\mathbf{x} + \int_K (\theta J_\varrho - \theta \tilde{J}_{\varrho,h}) \mathbf{u}_h \cdot \mathbf{w} d\mathbf{x}$$

We will obtain the estimates by appropriate choices of the function $\mathbf{w}$ in (2.23) With each $K \in \mathcal{T}_h$ we associate the bubble function K equal to the product of the barycentric coordinates on K. For each edge $e \in \mathcal{E}_K$ we associate the bubble function ψ_e equal to the product of the barycentric coordinates on e.

Proposition 2.12. There exists a constant c independent of h and α such that the following estimate holds [[12] Proposition 4.4], for all $K \in \mathcal{T}_h$

(2.24)

$$\eta_K \leq c \left\| \mathbf{u}_\alpha - \mathbf{u}_{\alpha,h} \right\|_{\alpha,\omega_K} + c \left(\sum_{K' \in \omega_k} h_{K'}^2 \alpha_{K'}^{-1} \left\| \mathbf{f} - \mathbf{f}_h \right\|_{L^2(K')}^2 + h_{K'}^2 \alpha_{K'}^{-1} \left\| (\theta J_\varrho - \theta \tilde{J}_{\varrho,h})^{\frac{1}{2}}\, \mathbf{u}_\alpha \right\|_{L^2(K')}^2 \right)$$

Note that the term $h_{K'}^2 \alpha_{K'}^{-1} \left\| (\theta J_\varrho - \theta \tilde{J}_{\varrho,h})^{\frac{1}{2}} \mathbf{u}_\alpha \right\|^2_{L^2(K')}$ is of high order and could be dropped from the estimate (2.24).

2.5 Adaptive strategy and numerical experiments

We perform our numerical experiments using the software FreeFem++. We refer to the reader for details of FreeFem++ as a programing language for numerical solution of partial differential equations [43]. Though the CPU time optimization is not performed throughout our computations, but if necessary, one can use standard methods to speed up the computations for optic flow. The computation of the matrix $J_{\varrho,h}$ is performed by using a $P1$ approximation with mass lumping which is known to be a stable and accurate method.

2.5.1 Adaptive strategy

As the geometric domain for given image is already well refined, therefore we use a novel strategy for adaptive procedure which is different from usual refinement techniques. This interesting method is based on coarsening the initial grid. Specially in this case as we observe from our experiments that the refinement of gird is performed by increase in grid points on discontinuities like edges and other damaged regions where error indicator density is large, consequently the coarsening of grid appears in the regions away from the edges of flow field. This whole procedure is performed automatically showing the dramatic regularization effects on optic flow grid. The algorithm is based on the following steps:

(1) We start with the cartesian grid $\mathcal{T}_h^0$ corresponding to the image.

(2) **Adaptivity steps:**

- Compute $\mathbf{u}_{\alpha_0,h}$ on $\mathcal{T}_h^0$ with $\alpha = \alpha_0$ a large constant.
- We build and adapted isotropic mesh $\mathcal{T}_h^1$ (in the sense of the finite element method, i.e with respect to the parameter h) with the metric error indicator

which is well suited for the optic flow $\mathbf{u}_{\alpha_0,h}$.

- we perform the local adaptive choice of $\alpha(x)$ on $\mathcal{T}_h^1$ and obtained a new function $\alpha_1(\mathbf{x})$.

(3) GO to step 2 and compute $\mathbf{u}_{\alpha_{1,h}}$ on $\mathcal{T}_h^1$.

Let us give more details on the implementation of this algorithm. On the triangulation $\mathcal{T}_{h,n}$ we compute the solution $\mathbf{u}_{\alpha_n,h}$

In addition to the standard information on the error distribution on the computations of $\mathbf{u}_{\alpha_n,h}$, the error indicators act as a confidence measure by locating the regions of large errors on the gradients (edges).

Note that all the meshes $\mathcal{T}_h^n$ are obtained by mesh adaptivity such that the minimal mesh sizes are greater than 1 which is the size of pixel.

The principal of the adaptive regularization process is to decrease the values of α in the regions where the error indicator is large(edges) and to increase the values in the complementary regions. However, for stability reasons we start with a relatively high initial guess and during the adaptive process α decreases. For automatic choice of α during the adaption we use following formula for each triangle K

$$\alpha_k^n = \frac{1}{|K|}\int_K (\alpha(\mathbf{x}))_{i,j}\, d\mathbf{x}\ 1 \le i,j \le 2 \tag{2.25}$$

$$\alpha_K^{n+1} = \mathtt{max}\left(\frac{\alpha_K^n}{1+\kappa * \left(\left(\frac{\eta_K}{\|\eta\|_\infty}\right) - 0.1\right)^+}, \alpha_{trh}\right) \tag{2.26}$$

where α_{trh} is a threshold and κ is a coefficient chosen to control the rate of decreasing of α, $(u^+) = \mathtt{max}(\mathbf{u}, 0)$ and $\|\eta\|_\infty = \mathtt{max}_K(\eta_K)$

This formula could be explained as follows: first we normalize $\eta_K \in (0,1)$ and if it is greater to 10% then we decrease the value of α. The value 10% as well as the choice of κ are chosen experimentally. Typically we choose the value of κ as 5 or 10.

Remark 2.13

(i) In these formulas we make the choice of taking α, more or less, constant in the regions where the flow is smooth and the error indicator is small.

(ii) When some a priori information on regions of uncertainties or damaged regions

in the image are available, we may keep the value of α very small (in these regions) which allows us to approximate correctly the Neumann boundary conditions in such nonsmooth situations. The algorithm is efficient in the sense that we obtain the regularized optic flow with a few elements (computational efficiency) and a map (the graph of $\alpha(\mathbf{x})$) which constitute a natural confidence measure. In the following examples we give an illustration of our adaptive approach to the optic flow determination.

2.5.2 Example 1:Taxi Sequence

In this example we consider a Taxi sequence available at http://i21www.ira.uk.de/, we have 256 x 191 gray value images. Here we consider the first two frames of taxi image sequence to compute optic flow using the variational optic flow model (2.5). To show the adaptive control of regularization for the given variational model we have performed four adaptive iterations using the given adaptive algorithm 2.5.1. The numerical results are given here as the vector plots, the plots showing the magnitude of optic flow, meshes obtained from the various adaptive iterations, error indicators η_K, $\tilde{\eta}_K$ and the plots for the distribution of $Log_{10}\alpha$. The results are given on unstructured gird as the computational domain. The robustness of adaptive algorithm is quite clear from the given numerical results. Moreover the performance of the algorithm is slightly improved as compared to the results given in [12], specifically when we compare the given meshes on the various iterations. Dramatic refinement and coarsening of grid improves the quality of solution at each adaptive iteration which is the main goal of the given algorithm. From left to right and from top to bottom, for every image there is given a caption which explains the purpose of corresponding result. From the mesh adaption process we observe that the number of elements increase along the edges while the coarsening of the grid occurs far from these regions. Initially we choose the value of α very large. Here for this example we select the initial value as $\alpha = 1000$. The value of α automatically changes on on various regions of domain with respect to the change in the value of error indicator as shown in given formula for α_K in the given adaptive algorithm. One should note particularly in this example that we have given some plots for error indicator $\tilde{\eta}_K$ and distribution of $Log(\alpha)$ for various iterations as

color images, here the lighter color shows smaller value of corresponding parameter and darker(rich) color shows larger value(the scales given are difficult to visualize because of some technical reasons). One can observe that as the adaptive procedure starts working, the value of α decreases along edges, consequently the regularization effects appear on the damages regions of resulting flow field with the refinement of mesh in these regions. The error indicator density also decreases during the adaptive process as shown in the given plots. Though the performance of the adaptive algorithm is improved with the improvement in data term but we have observed that the edges are still looking smoothed which is may be because of extra smoothness properties of quadratic regularizer, keeping this fact in view we propose the TV regularization (usually used for discontinuity preservation in the image processing) in this thesis which will be discussed in forthcoming chapters where we will show the experimental results for taxi image sequence with enhanced edges.

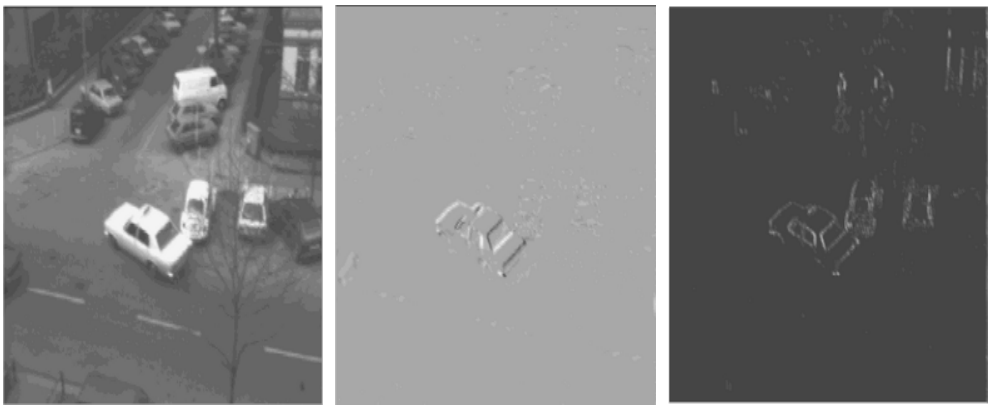

(a) First frame taxi sequence (b) Time derivative f1-f2 (c) Structure tensor J_ϱ

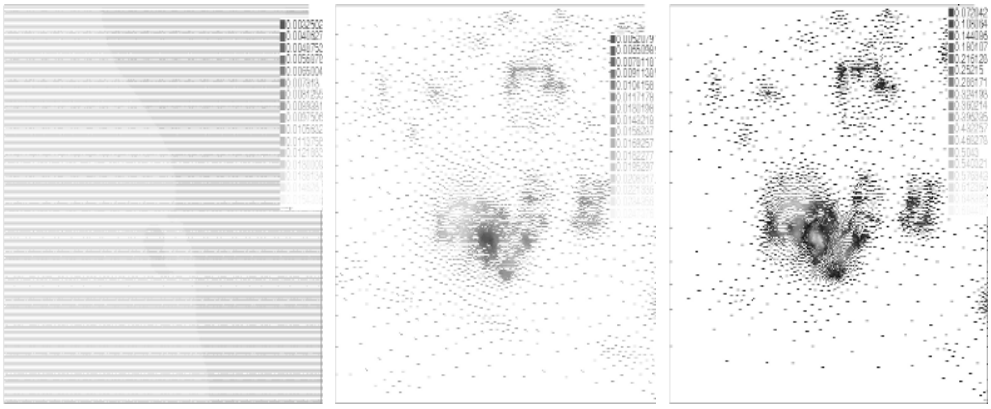

(d) Flow vector iter0 (e) Flow vector iter1 (f) Flow vector iter2

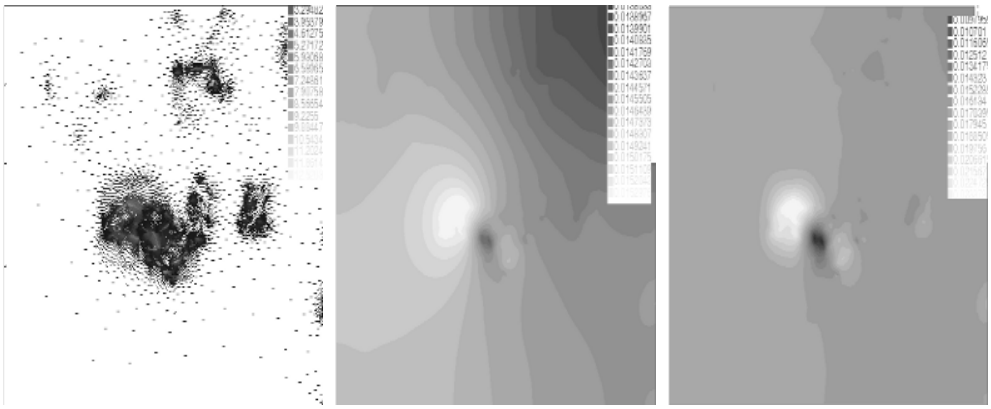

(g) Flow vector iter3 (h) Flow magnitude iter0 (i) Flow magnitude iter1

Figure 2.1: Example:1. Humburg Taxi Sequence and Quadratic regularization

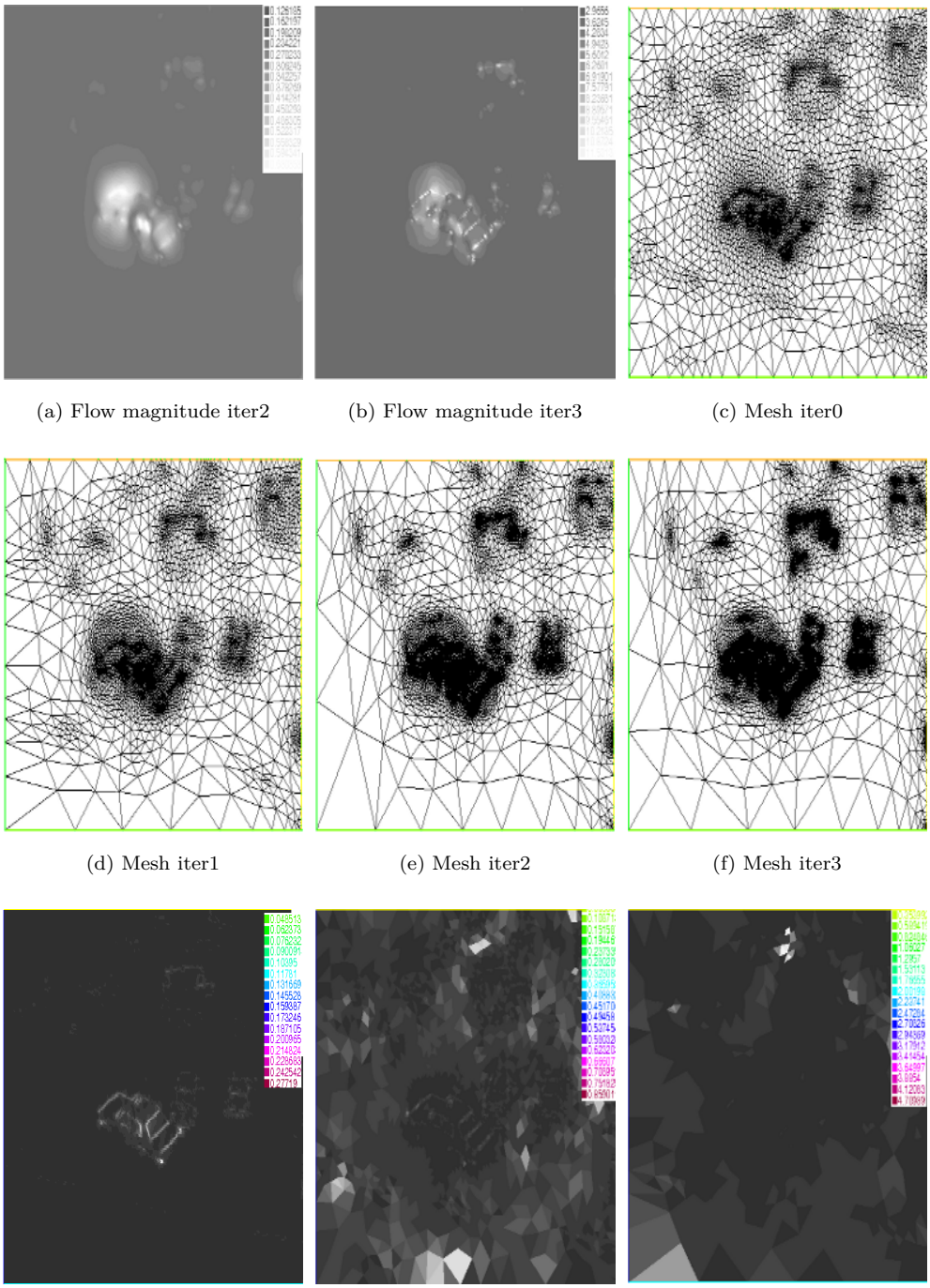

(a) Flow magnitude iter2 (b) Flow magnitude iter3 (c) Mesh iter0

(d) Mesh iter1 (e) Mesh iter2 (f) Mesh iter3

(g) Error density η_K iter0 (h) Error density η_K iter1 (i) Error density η_K iter2

Figure 2.2: Example:1. Humburg Taxi Sequence and Quadratic regularization

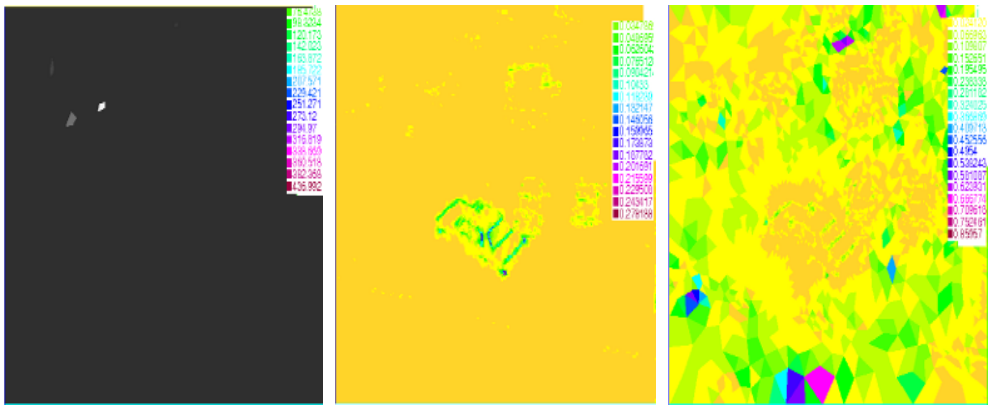

(a) Error density η_K iter3 (b) Gradient $\tilde{\eta}_K$iter0 (c) Gradient $\tilde{\eta}_K$iter1

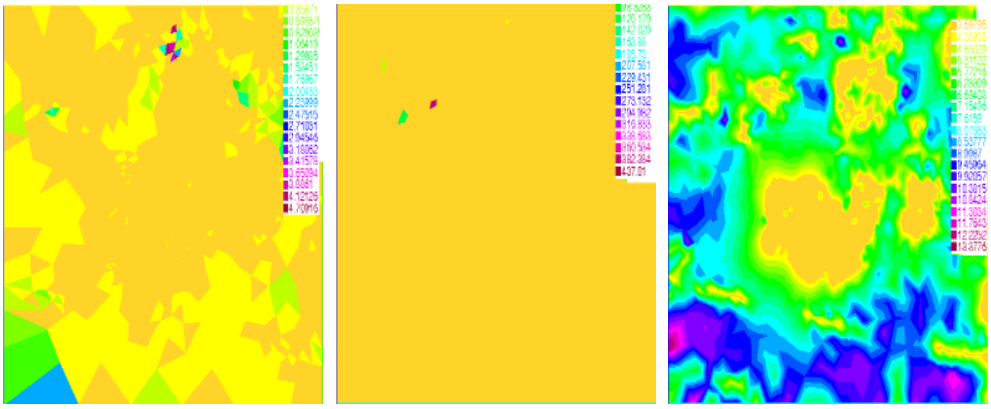

(d) Gradient $\tilde{\eta}_K$iter2 (e) Gradient $\tilde{\eta}_K$iter3 (f) $Log_{10}\alpha$ iter0

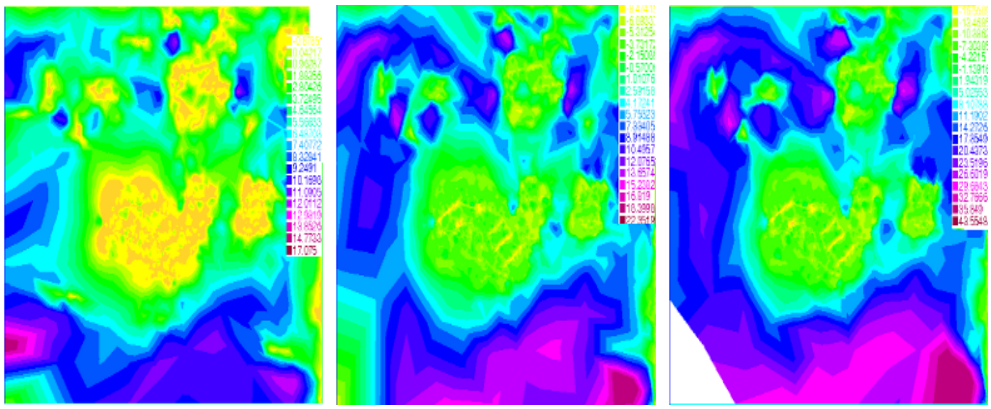

(g) $Log_{10}\alpha$ iter1 (h) $Log_{10}\alpha$ iter2 (i) $Log_{10}\alpha$ iter3

Figure 2.3: Example:1. Humburg Taxi Sequence and Quadratic regularization

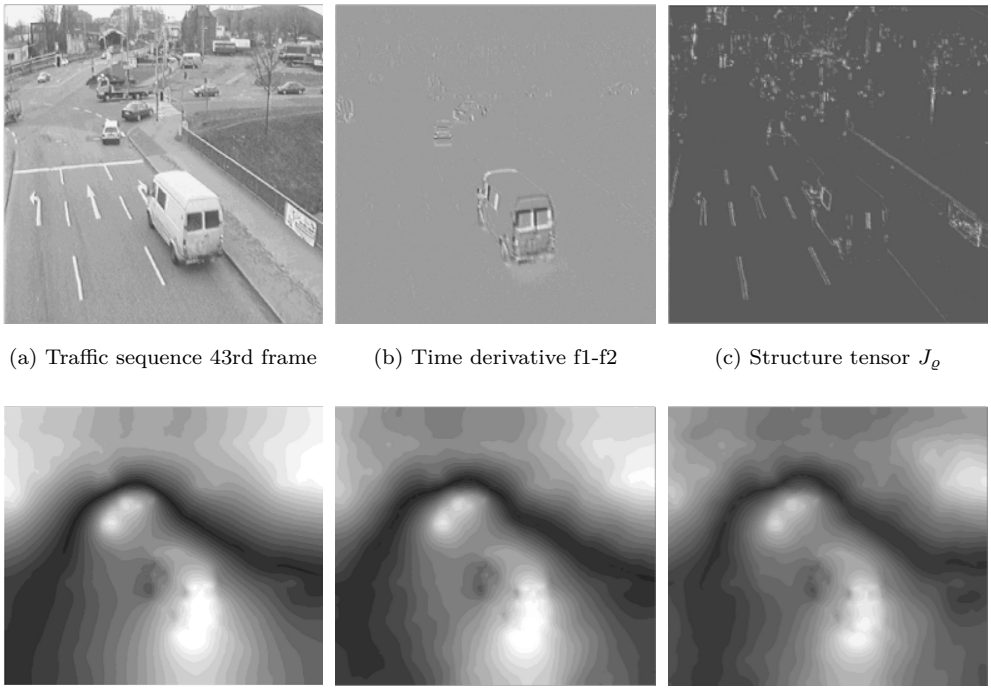

(a) Traffic sequence 43rd frame (b) Time derivative f1-f2 (c) Structure tensor J_ϱ

(d) Flow magnitude iter0 (e) Flow magnitude iter1 (f) Flow magnitude iter2

Figure 2.4: Example:2 Traffic Intersection Sequence and Quadratic regularization

2.5.3 Exaple:2 Traffic Intersection Sequence

Traffic sequence showing an intersection at Rheinhafen, Karlsruhe downloaded from http://i21www.ira.uk.de/. In this example we test our algorithm and perform 10 iterations of adaptation. Initially we choose $\alpha = 1000$. The distribution of $log(\alpha)$ is shown on various iterations of adaptation which demonstrates the refinement and coarsening of grid, one can observe from adaptive iterations that the value of α almost decreases in the damages regions like edges and remains stable or increases in the flat regions of computational domain. This whole process provides a robust adaptive control and regularization procedure which furnishes the dense flow field on the corners of moving image. The results in this case are very smooth ans not quiet satisfactory because of extra smoothness and low quality images with brightness variations seen on the flow magnitude images. Results are given with the captions describing the purpose of each plot.

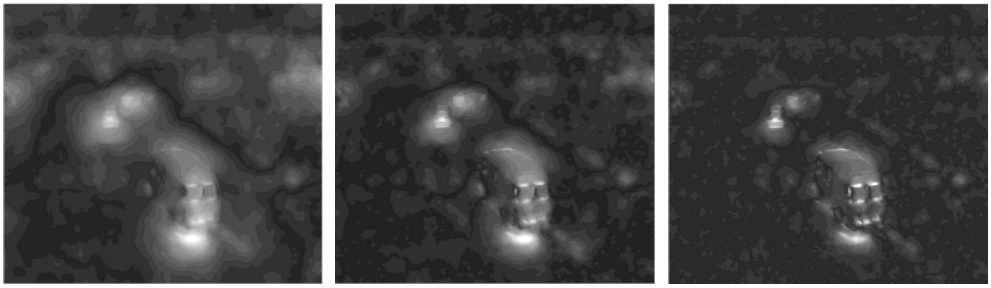

(a) Flow magnitude iter6 (b) Flow magnitude iter7 (c) Flow magnitude iter8

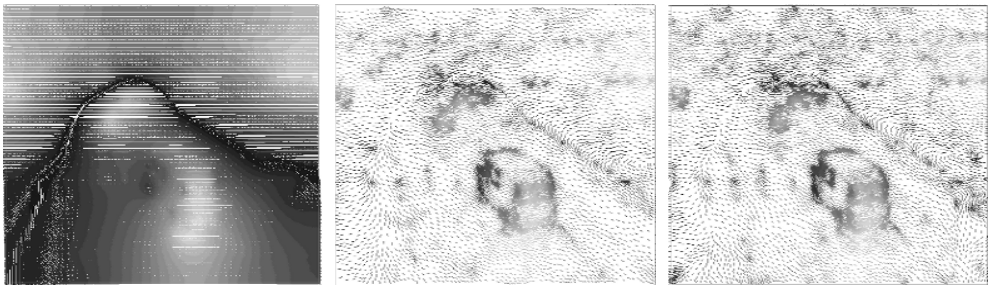

(d) Flow vector iter0 (e) Flow vector iter2 (f) Flow vector iter3

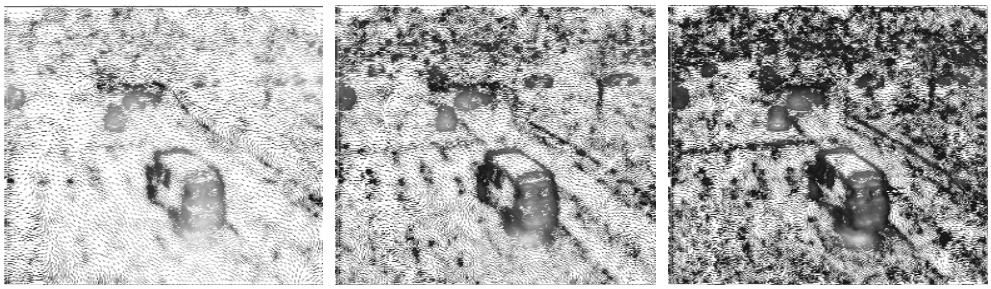

(g) Flow vector iter4 (h) Flow vector iter6 (i) Flow vector iter7

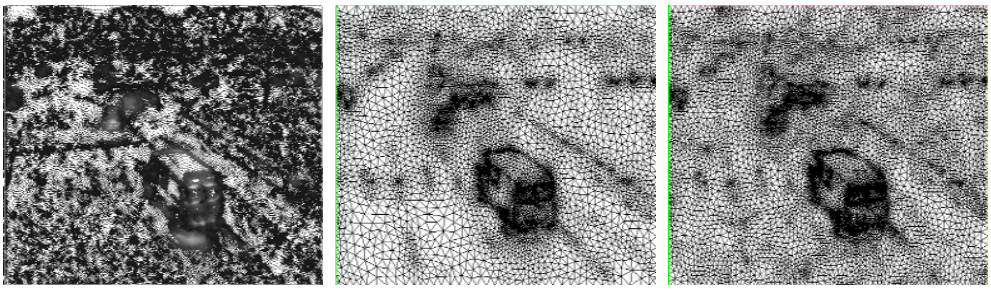

(j) Flow vector iter8 (k) Mesh iter0 (l) Mesh iter1

Figure 2.5: Example:2 Traffic Intersection Sequence and Quadratic regularization

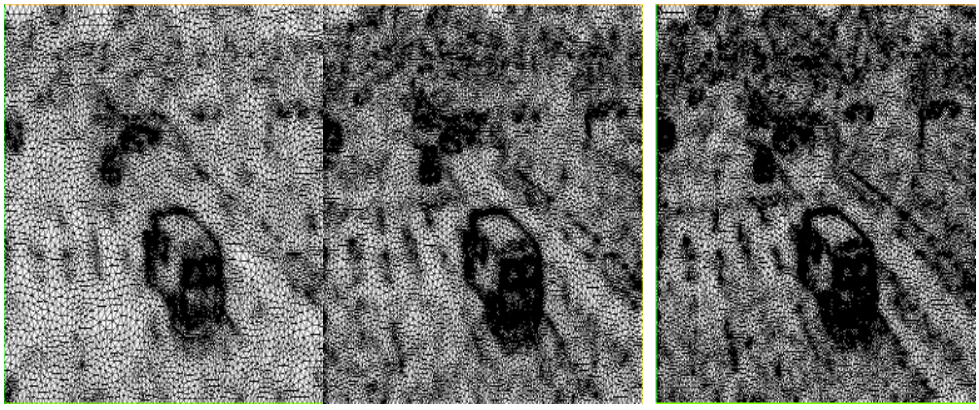

(a) Mesh iter2 (b) Mesh iter4 (c) Mesh iter5

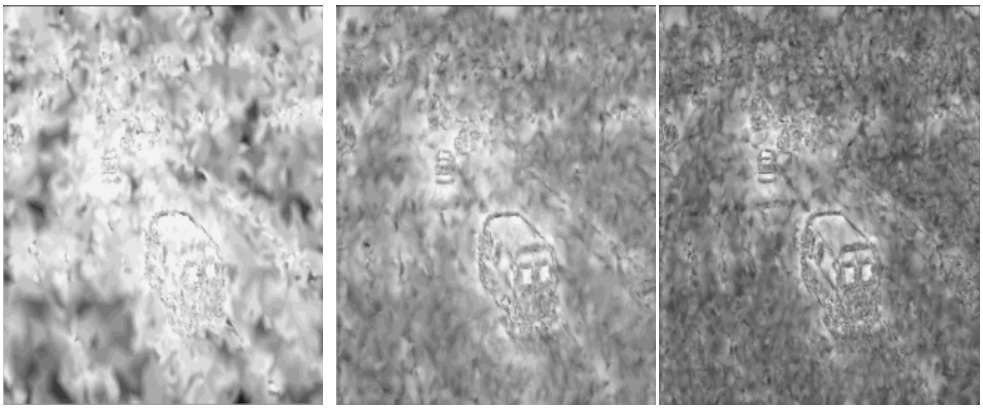

(d) $Log_{10}\alpha$ iter0 (e) $Log_{10}\alpha$ iter3 (f) $Log_{10}\alpha$ iter5

Figure 2.6: Example:2 Traffic Intersection Sequence and Quadratic regularization

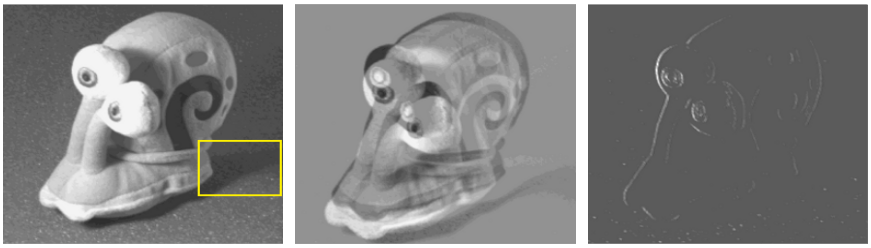

(a) Snail sequence first frame shadow is highlighted (b) Time derivative f1-f2 (c) Structure tensor J_ϱ

Figure 2.7: Example:3 Snail Sequence

2.5.4 Example 3: Snail sequence

We consider the grey version of snail image sequence downloaded from $http://www.mia.uni-saarland.de/Research/CVOpticFlow.shtml$. This sequence was already tested in [52], where they have used a HSV color representation with higher order constancy assumptions. We test our algorithm using grey version of sequence and show the regularization effects on various adaptive iterations for optical flow computations. Initially we select $\alpha = 1000$. We perform six iteration of mesh adaption and show the plots for flow field and corresponding mesh at each iteration. The motion of shadow during the image motion is highlighted by applying yellow box around shadow at each iteration of adaption. In order to show the effects of regularization on geometrical domain of flow field we have given here the plots for distribution of α on the computational domain of flow field for three iterations. One can observe from these images that the geometry of image is almost smooth therefore the interesting regularization effects appear on the domain as demonstrated by the variations in α on the various regions. The plots for α are given in color images, to identify the level of increase or decrease is same as given in the case of taxi sequence. The darker color(rich) shows the greater value and lighter color shows the smaller value, for example one can observe that the value of α decreases beside the eyes of the image(edges) and increases away from these regions with respect to adaptation time. We also observe from the given meshes which justify the claim of the given algorithm.

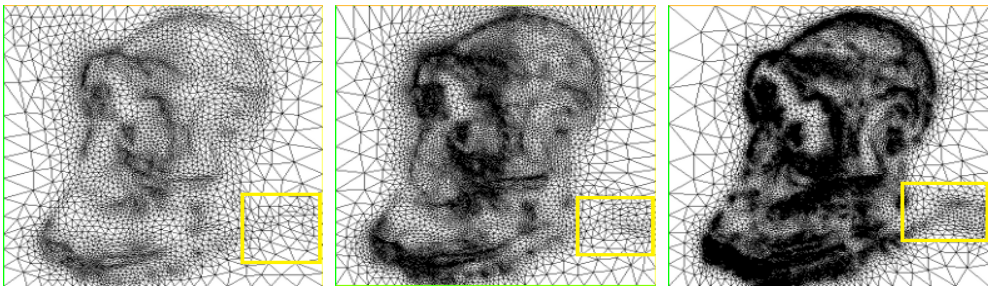

(a) Mesh first iteration (b) Mesh 2nd iteration (c) Mesh 3rd iteration

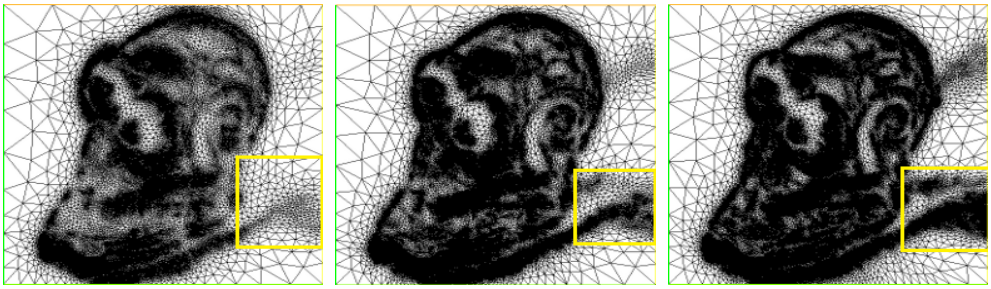

(d) Mesh 4th iteration (e) Mesh 5th iteration (f) Mesh 6th iteration

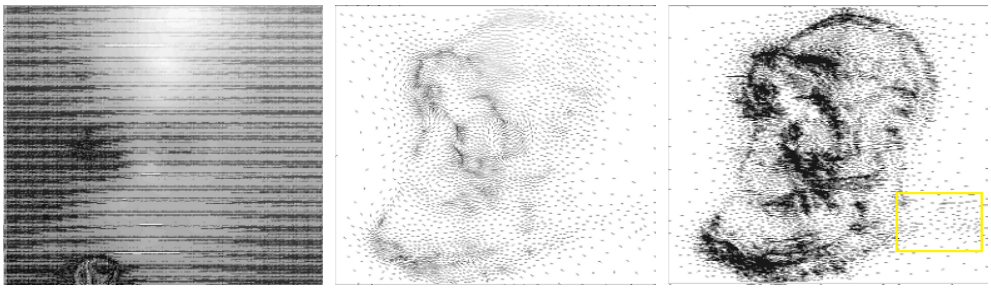

(g) Optic Flow Field ite0 (h) Optic Flow Field First Iter (i) Optic Flow Field 2nd Iter

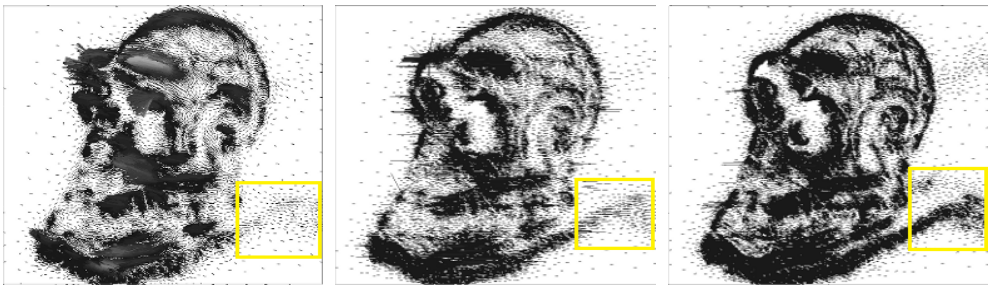

(j) Optic Flow Field 3rd Iter (k) Optic Flow Field 4th Iter (l) Optic Flow Field 5th Iter

Figure 2.8: Example:3 Snail Sequence and Quadratic regularization

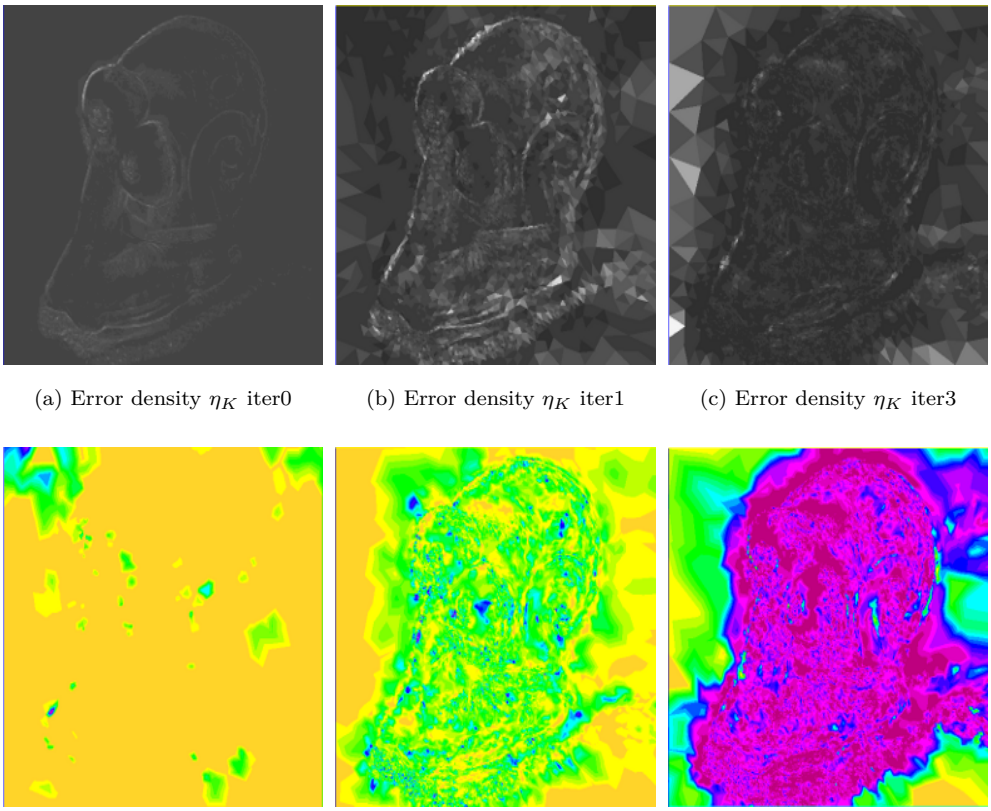

(a) Error density η_K iter0 (b) Error density η_K iter1 (c) Error density η_K iter3

(d) α iter1 (e) α iter3 (f) α iter6

Figure 2.9: Example:3 Snail Sequence and Quadratic regularization

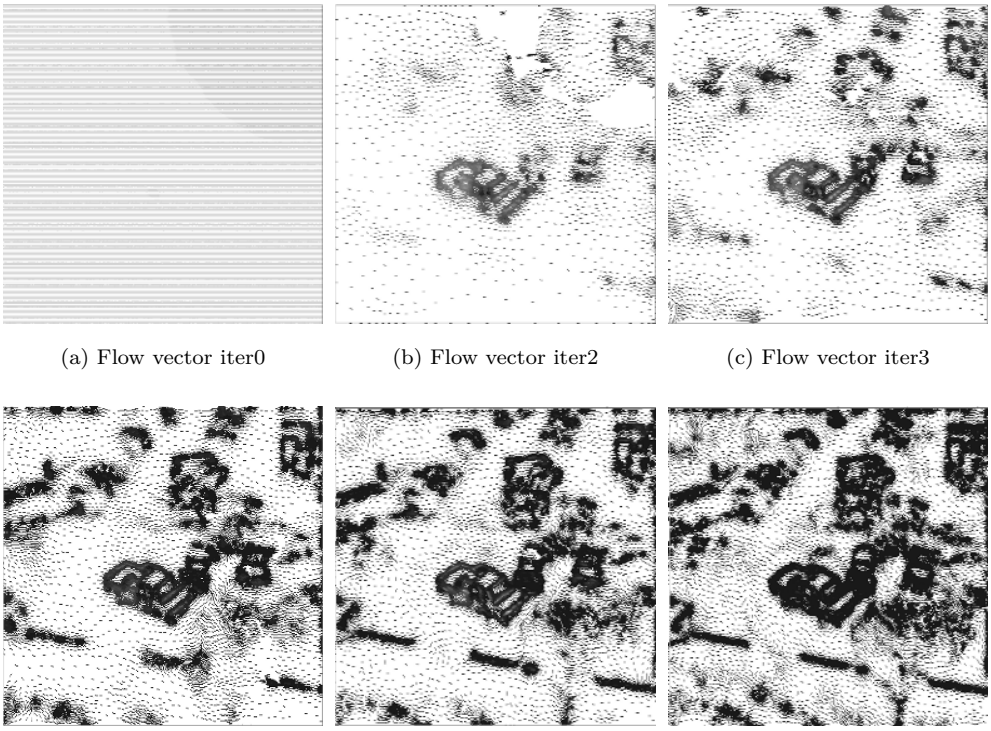

(a) Flow vector iter0 (b) Flow vector iter2 (c) Flow vector iter3

(d) Flow vector iter4 (e) Flow vector iter5 (f) Flow vector iter6

Figure 2.10: Example:4 Taxi Sequence with P2 Finite element and Quadratic regularization

2.5.5 Example 4: Taxi Sequence using P2 Finite element

In this example we consider the same frames of taxi sequence but we change the strategy of computation with increasing the order of interpolant for the finite element as P2. The goal of this experiment is to check the performance and capability of our method using higher order finite elements and to compare the computing performance of the method with lower order finite elements. We start with $\alpha = 1000$ and perform 7 iterations of mesh adaption. Though the sharpness in flow field is improved in this case but computational time increases and the algorithm works slower as compared to P1 finite element. Our results are given with the captions for each plot which describes well the purpose for computed result and number of iteration on which the given parameter is computed.

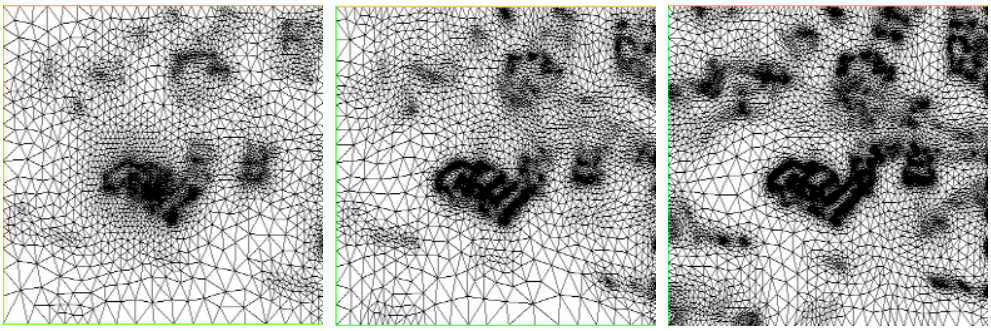

(a) Mesh after iter0 (b) Mesh after iter1 (c) Mesh after iter2

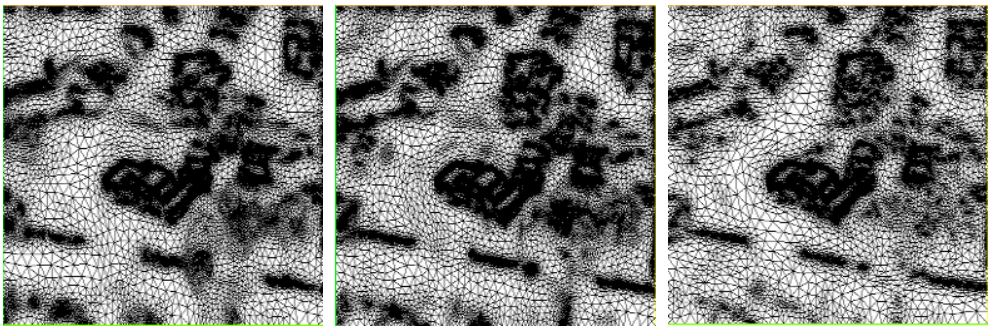

(d) Mesh after iter3 (e) Mesh after iter4 (f) Mesh after iter6

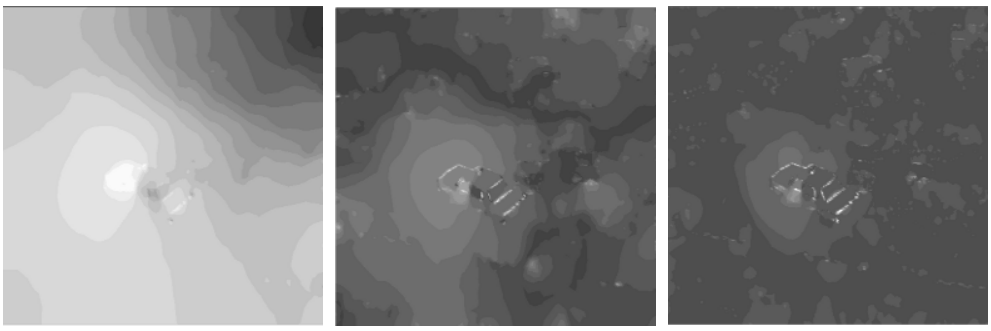

(g) Flow magnitude iter1 (h) Flow magnitude iter3 (i) Flow magnitude iter6

Figure 2.11: Example:4 Taxi Sequence with P2 Finite element and Quadratic regularization

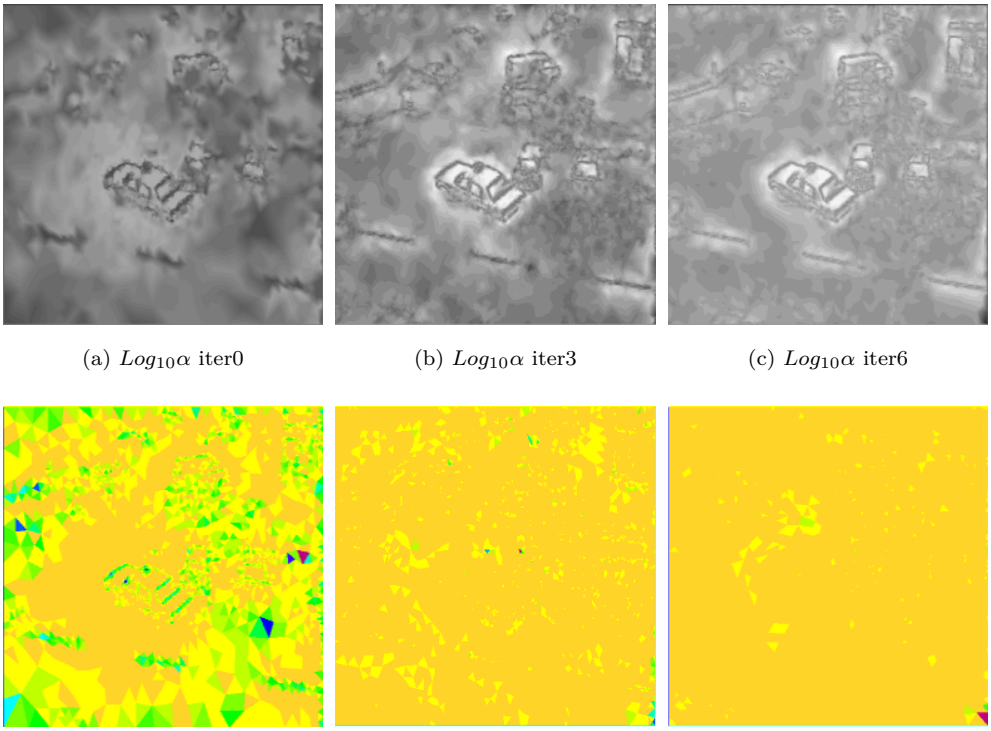

(a) $Log_{10}\alpha$ iter0 (b) $Log_{10}\alpha$ iter3 (c) $Log_{10}\alpha$ iter6

(d) Error density η_K iter0 (e) Error density η_K iter3 (f) Error density η_K iter6

Figure 2.12: Example:4 Taxi Sequence with P2 Finite element and Quadratic regularization

2.6 Conclusion

The linear complementary optic flow model (2.5) brought in to the consideration for the scientific computations of optic flow and control of effect of regularization. Our method allow the choice of local regularization parameters which is an automatic and iterative procedure of regularization. The automatic refinement and derefinement of image grid is a robust quality of this method which is a novel approach and provides the sharp and dense optic flow field on the grid. One can observe from our results given for the various adaptive iterations that the claim given in the adaptive algorithm that the scalar pointwise function $\alpha(\mathbf{x})$ decreases on the damaged regions like corners and increases or remains stable in the flat or smooth regions is almost satisfied from computational point of view. The decrease in α results in refinement of grid which yields dense flow field where as the increase in α coarsen the grid which is mostly observed in flat and smooth regions in flow field. Each new iteration yields a dramatic regularization effect and improvement in densifying the optic flow field. The meshes for flow field on various iterations of adaptation are provided here to fulfill our claim. Though the given adaptive algorithm but as the regularization approach used in this chapter is quadratic, therefore the smoothness in edges is still a challenge. To cope with this problem of extra smoothing we propose the nonlinear regularization approach in the forth coming chapters.

Chapter 3

Modeling and Analysis of TV-Regularization in Stereo-Vision Problems

3.1 Introduction

Visual correspondence problems are of central importance in computer vision. Computation of stereo motion, optical flow and other vision problems rely on visual correspondence.

Identifying the corresponding pixels in a given pair of images in a same real world scene is called visual corresponding problem. If the images are taken from different view points then visual corresponding gives stereo depth of the scene. If the images were taken from same point of view but at different times then visual correspondence gives motion of the scene. The shift in the coordinates between the corresponding pixels is called disparity. In the stereo case the disparities are usually one dimensional quantities that represent the horizontal shifts due to the camera setup or image rectification. In the case of motion the disparities are usually two dimensional and shifts occur both in vertical and horizontal directions, motion in this case is known as optic flow. This chapter is devoted to the mathematical settings of the correspondence problems by considering the stereo image pair obtained from the same scene. Computation of stereo problems is one of the challenging tasks in computer vision research. The depth information here is obtained by change in the position of each pixel in left view w.r.t right view during the camera motion which is usually termed as the horizontal disparity map. Variety methods is available on the disparity estimation [1, 20, 35, 66]. Different robust approaches like feature based, area based, phase based, and energy based are available in literature but due to uncertainties in the imaging process and ambiguities in visual interpretation the problem is ill-posed and the accuracy in estimation of disparity is still doubtful, more over the accurate and efficient computation is one of the challenging tasks for image community.

Energy based approach is an elegant approach where an energy functional is minimized to solve computer vision problems. Minimizing the continuous energy functionals leads in a natural way to partial differential equations. The fastly emerging use of PDE-based image restoring methods such as nonlinear diffusion filtering and total variation denoising, has motivated many researchers to apply similar ideas to estimate correspondence problems[1, 12, 20, 93, 19, 16, 90, 17, 66, 35]. In this chapter we present the mathemat-

ical framework for TV regularization variational stereo model and study the existence and uniqueness of optimizer in a general framework of calculus of variations. We use classical results from direct calculus of variations to show the existence and uniqueness for minimization of energy functional, moreover we give here the short overview of the role of the smoothing/regularization processes that are part of the local and global approaches in correspondence problems. Variational stereo computations require the solution of a parametrization problem with data term based on constancy assumptions and smoothness term which regularize the solution to recover the horizontal missing depth information between two images.

3.2 Variational Stereo Problem

3.2.1 General structure

In order to formulate the stereo estimation problem, let we consider an image pair modeled by a real valued function $I : \Omega \longrightarrow \mathbb{R}$, where $\Omega \subset \mathbb{R}^2$ is a image domain, bounded with piecewise smooth boundary. We further assume that the images are presmoothed by a convolution with a Gaussian kernel of standard deviation σ.

Role of the Pre-Smoothing process: Pre-smoothing usually lead to the improved the results [91]. Let us consider some image frames $\mathsf{g}(x_1, x_2)$ where (x_1, x_2) denotes the location within a rectangular domain Ω. It is common to smooth the image sequence prior to differentiation e.g by convolving each frame with some Gaussian $K_\sigma(x_1, x_2)$ of standard deviation σ :

$$I(x_1, x_2) := (K_\sigma * \mathsf{g})(x_1, x_2)$$

The low-pass effect of Gaussian convolution removes the noise and other destabilizing high frequencies. It guarantees that $I \in C^\infty$, which in general is useful to establish any well-posdness proof for the presented methods. Since the amount of the smoothing in this processing step is directly related to the noise level of the input data, the standard deviation σ of Gaussian kernel is generally known as noise scale parameter [17]. The impact of such a presmoothing step on input data is illustrated in Figure 3.1. Too large

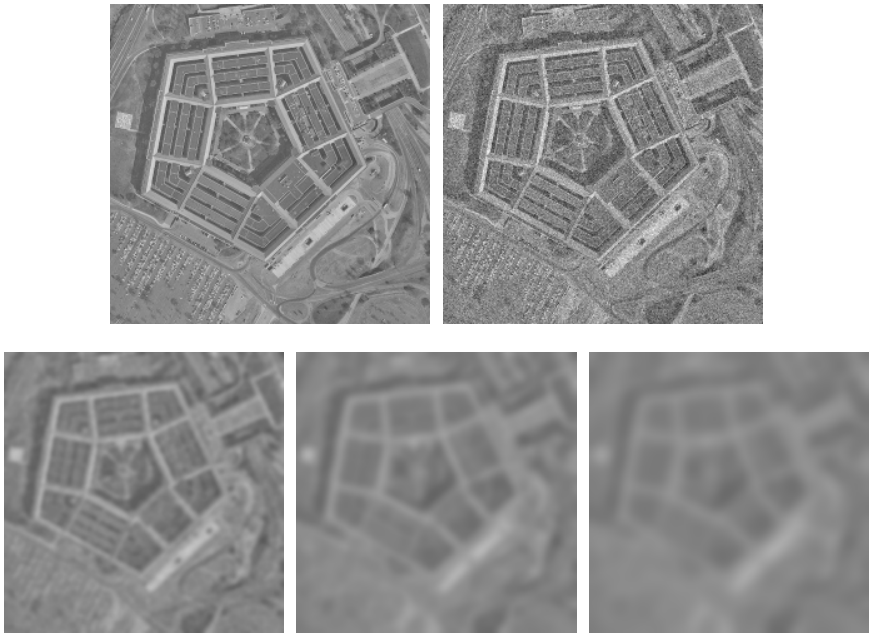

Figure 3.1: Effects of presmoothing step. From left to right and from top to bottom (a) **Top left:** Original aerial left view of image pentagon downloaded from http://vasc.ri.cmu.edu/ (b) **Top right:** Added Gaussian noise of standard deviation $\sigma_n = 15$ (c) **Bottom left:** convolution with truncated Gaussian kernal of standard deviation $\sigma = 2$ (d) **Bottom middle:** convolution with truncated Gaussian kernal of standard deviation $\sigma = 4$ (e) **Bottom right:** convolution with truncated Gaussian kernal of standard deviation $\sigma = 6$.

amount of presmoothing may be problematic by removing useful details that may not allow to establish better correspondences.

Energy Minimization:

We compute the unknown horizontal disparity component u by minimizing the following energy functional.

$$\mathbf{E}(u) = \int_{\Omega} (\alpha(\mathbf{x})\Psi(|\nabla u|) + \mathbf{D}(I(\mathbf{x}), u))\, d\mathbf{x} \tag{3.1}$$

where $\mathbf{x} := (x_1, x_2)^T \in \Omega$. The structure of the given energy functional (3.1) is based on following two parts.

i.Regularizing term: The term $\alpha(\mathbf{x})\,\Psi(|\nabla u|)$ is generally known as regularizer or smoothness term which plays the role of smoothing the disparity u by its filling-in effect, where $\nabla := (\partial x_1, \partial x_2)^T$ denotes the gradient operator and $|.|$ denotes the Euclidean norm.

ii. Data Term: The term $\mathbf{D}(I(\mathbf{x}), u)$ is denoted as data term plays a role of matching the disparity u with given image pair $I(x_1, x_2)$. Typically the data term is modeled using different constancy assumptions. Several energy minimization algorithms have been proposed to solve (3.1), various approaches are available in literature[12, 93, 51].

Regularization:

A classical way to overcome the ill-posed problems in computer vision is to add a regularization term to energy functional. This idea was introduced by Tikhonov and Arsenin[86] in 1977. Then the regularization approaches go back to the work of Horn and Schunck [51] in 1981, and then improved by Nagel [70] in 1983 where they were first successfully introduced in optical flow computations. Recent variational stereo approaches either use isotropic disparity-driven regularizers [7] which adapt the smoothing of the disparity map w.r.t. the magnitude of the disparity gradient, or anisotropic image-driven regularizers that try to preserve edges in accordance with the image data [2]. For stereo, those were used among others, in the work of Slesareva et al. [81]. A more sophisticated approach was proposed by [20]. A theoretical framework for a broad class of regularization methods for optic flow estimation is given in [90], they have mainly focused on convex rotationally invariant functionals and and a detailed study on four classes of convex regularizers as isotropic-image driven, isotropic-flow driven, anisotropic-image driven and anisotropic-flow driven is given. We give here the summary of these four classes of regularizes in following table, for more details we refer the reader to [90].

Where $B(\nabla I)$ is a regularized projection matrix of order two, also called diffusion tensor. The usage of a diffusion tensor $B(\nabla I)$ instead of a scalar-valued diffusivity $g(|\nabla I|^2)$allows a direction-dependent smoothing behavior. This regularization process can therefore be classified as anisotropic.

Table 3.1: Classification of Regularizers

	Isotropic	Anisotropic
Image-Driven	$g(\|\nabla I\|^2)\,\|\nabla u\|^2$	$\nabla u^T B(\nabla I)\nabla u$
Flow-Driven	$\psi(\|\nabla u\|^2)$	tr $\psi(\nabla u \nabla u^T)$

This work is extension of [12] for optical flow determination where a quadratic regularizer $\Psi(|\nabla u|) = |\nabla u|^2$ is proposed and the discontinuities are controlled by a weight function $\alpha(\mathbf{x})$ and mesh adaption process performed by derived a posteriori error estimators. In order to get an edge-preserving regularization in computer vision problems, one usually assumes that the images belong to the space of functions of Bounded Variation (BV). To preserve discontinuities like edges in the stereo depth we propose in this thesis the well known approach called Total Variation regularization(TV) which was already proposed by ROF in 1996 for image denoising [76] and [10, 47, 57]. We have in (3.1) $\Psi(|\nabla u|) = |\nabla u|$. The weight function $\alpha(\mathbf{x}) : \Omega \longrightarrow \mathbb{R}^+$ is a given continuous function on Ω, moreover we assume that $\alpha(\mathbf{x})$ is bounded and away from zero. It is also assumed here that the domain Ω is smooth open set.

Brightness Constancy assumption: Many differential methods for image sequence analysis are based on constancy assumption, that the grey values of image objects in subsequent frames of same scene do not change over the time. In the case of stereo motion we model the data term using brightness constancy assumption on the grey values of pixels during the camera motion which reads:

$$I(\mathbf{x} + \mathbf{u}, t + 1) = I(\mathbf{x}, t) \tag{3.2}$$

where $\mathbf{u} = (u, 0)^T$. We assume that $I \in C^1((\Omega; \mathbb{R})$. Using first order Taylor's expansion on (3.2), we set the data term as

$$\mathbf{D}(I(\mathbf{x}), \mathbf{u}) = (I_{x_1} u + I_t)^2 \tag{3.3}$$

We set $\mathbf{f} = -I_{x_1} I_t$, where I_{x_1} and I_t stand for derivatives with respect to x_1 and t respectively.

3.2.2 Analysis of stereo model in the framework of calculus of variations.

The minimization problem (3.1) is solved in the space of functions of bounded variations i.e the space of functions u such that $\|Du(\Omega)\| < \infty$. Here Du is the distributional gradient of u. This functional space is typically used in image analysis. The main reason is that the functions can be discontinuous across the hypersurfaces. In the terms of images, this means that the images are discontinuous across the edges. Among our first concerns, we are interested in the existence of a solution. The presentation of the methodology to prove existence reveals two major notions: coercivity and lower semicontinuity (abbreviated l.s.c). Now, if the functional is not l.s.c., the idea is to look at the greatest l.s.c. functional less than or equal to the initial one. It is called the relaxed functional [47].

Existence and uniqueness of solution

We recall the following well established theory on existence and uniqueness from [47]. Associated to the functional $E(u)$ the minimization problem

$$m := inf\{E(u) : u \in X\}$$

where the natural space X on which we wish to find the solution is

$$X = \left\{u \in L^2; \nabla u \in L^1(\Omega)^2\right\}$$

In order to use direct method of calculus of variations we have to assume some minimal hypotheses on $\Psi(s)$:

i. $\Psi(s)$ is strictly convex, nondecreasing function from $\mathbb{R}^+$ to $\mathbb{R}^+$ with $\Psi(0) \approx 0$ (without loss of generality).

ii. $\lim_{s \longrightarrow +\infty} \Psi(s) = +\infty$

iii. We assume that Ψ grows at most linearly i.e: There exist two constants c_1 and c_2 such that:

$$c_1 s - c_2 \leq \Psi(s) \leq c_1 s + c_2.$$

To proceed further we recall some useful properties of $BV(\Omega)$, we assume that Ω is bounded and has Lipschitz boundary.

(P_1) **Lower semicontinuity:**

Let $u_j \in BV(\Omega)$ and $u_j \underset{L^1(\Omega)}{\longrightarrow} u$. Then $\int_\Omega |Du| \leq \underline{lim}_{j \longrightarrow \infty} \int_\Omega |Du_j|$, here Du is the distributional gradient of u.

(P_2) **A** *weak** **topology:**

$$u_j \xrightarrow[\text{BV-w}^*]{*} u$$

$$\Leftrightarrow u_j \xrightarrow[\text{L}^1(\Omega)]{} u$$

and $$Du_j \xrightarrow[\text{X}]{*} Du$$

where $Du_j \xrightarrow[\text{X}]{*} Du$ means $\int v Du_j \longrightarrow \int v Du$ for all v in $C_0(\Omega)^N$.

(P_3) **Compactness:**

Every uniformly bounded sequence u_j in $BV(\Omega)$ is relatively compact in $L^P(\Omega)$ for $1 \leq p < \frac{N}{N-1},\ N \geq 1$. Moreover, there exist a subsequence u_{jk} and u in $BV(\Omega)$ such that $u_{jk} \xrightarrow[\text{BV-w}^*]{*} u$.

(P_4) Decomposability of $BV(\Omega)$

We recall the direct results on decomposability of $BV(\Omega)$ from [47] as follows.

$$|Du|(\Omega) = \int_\Omega |Du| = \int_\Omega |\nabla u| \, d\mathbf{x} + \int_{S_u} \left|u^+ - u^-\right| d\mathcal{H}^{N-1} + \int_{\Omega - S_u} |C_u|$$

Where second and third parts are know as jump part and cantor part. When u is a BV function, i.e Du is a measure. We can extend this decomposition more generally as follows.

Let $\Psi : \mathbb{R} \longrightarrow \mathbb{R}^+$ be convex, even nondecreasing on $\mathbb{R}^+$ with linear growth at infinity

and that Ψ^∞ be recession function of Ψ defined by $\Psi^\infty(z) = \lim_{s\longrightarrow+\infty} \frac{\Psi(sz)}{s}$. Then for $u \in BV$, we set.

$$\int_\Omega \Psi(Du) = \int_\Omega \alpha(\mathbf{x})\Psi(|\nabla u|)d\mathbf{x} + \Psi^\infty(1)\int_{S_u} \left|u^+ - u^-\right| d\mathcal{H}^{N-1} + \Psi^\infty(1)\int_{\Omega - S_u} |C_u|$$

The main consequence of this definition is that $u \longrightarrow \int_\Omega \Psi(Du)$ is l.s.c. for the $BV-w^*$. To show the existence and uniqueness of problem (3.1) we recall the theorem 3.2.1 of [47] and define the relaxed functional of $E(u)$ as

$$\bar{E}(u) = \int_\Omega \alpha(x)\Psi(|\nabla u|)d\mathbf{x} + c_3\int_{S_u} \left|u^+ - u^-\right| d\mathcal{H}^{N-1} + \int_\Omega (I_x u + I_t)^2 d\mathbf{x} \tag{3.4}$$

where $c_3 = \lim_{s\longrightarrow+\infty} \frac{\Psi(s)}{s}$

We solve the following minimization problem

$$\inf_{u\in BV(\Omega)} \bar{E}(u), \tag{3.5}$$

where $\bar{E}$ is defined by (3.4)

Theorem:3.1. Under the assumption i, ii, iii of this section and discussed BV properties the minimization problem admits a unique solution.

Proof: The Proof follows from [47]

step 1: Existence

Let u_n be minimizer for (3.5) considering assumption ii we have

$$\begin{cases} \alpha(\mathbf{x})\left|Du_n\right|(\Omega) = \int_\Omega \alpha(\mathbf{x})\left|\nabla u_n\right| d\mathbf{x} + c_3\int_{S_{u_n}} \left|u_n^+ - u_n^-\right| d\mathcal{H}^{N-1} \le M \\ \int_\Omega \left|I_x u_n + I_t\right|^2 d\mathbf{x} \le M \end{cases}$$

where M denotes a universal strictly positive constant that may differ from line to line. The first inequality above says that total variation of Du_n is uniformly bounded. It remains to prove that $|u_n|_{L^1}$ is bounded. Let $w_n = \frac{1}{|\Omega|}\int_\Omega u_n d\mathbf{x}$ and $v_n = u_n - w_n$. Then $\int_\Omega v_n d\mathbf{x} = 0$ and $Dv_n = Du_n$. Hence $|Dv_n| \le M$. Using the generalized Poincaré-Wirtinger inequality we obtained

$$|v_n|_{L^2}(\Omega) \le c_4\left|Dv_n\right|(\Omega) \le M \tag{3.6}$$

where c_4 is constant. Now from inequality $\int_\Omega \left|I_x u_n + I_t\right|^2 d\mathbf{x} \le M$ we deduce

$$|I_x u_n + I_t|_{L^2}^2 \le M$$

which is equivalent to

$$|I_x v_n + I_x w_n + I_t|_{L^2}^2 \leq M$$

Rewriting $I_x w_n$ by

$$I_x w_n = (I_x v_n + I_x w_n + I_t) - (I_x v_n + I_t)$$

we get

$$|I_x w_n|_{L^2} \leq M + |I_x v_n|_{L^2} + |I_t|_{L^2(\Omega)} \leq M$$

we have

$$|I_x w_n|_{L^2} = \left| \frac{1}{|\Omega|} \int_\Omega u_n d\mathbf{x} \right| |I_x|_{L^2} \leq M$$

which implies that $\left| \int_\Omega u_n d\mathbf{x} \right|$ is uniformly bounded. From (3.6) we obtained

$$|u_n|_{L^2}(\Omega) = \left| v_n + \frac{1}{|\Omega|} \int_\Omega u_n d\mathbf{x} \right|_{L^2(\Omega)} \leq |v_v|_{L^2} + \left| \int_\Omega u_n d\mathbf{x} \right|$$

Hence u_n is bounded in $L^2(\Omega)$ and in $L^1(\Omega)$ (Ω is bounded). Since $|Du_n|$ is also bounded, we get that u_n is bounded in $BV(\Omega)$. Subsequently there exist u in $BV(\Omega)$ such that $u_j \xrightarrow[\text{BV-w}^*]{} u$ and $u_j \xrightarrow[\text{L}^2(\Omega)]{} u$

Finally from weak semicontinuity property of convex function of measures and weak semi continuity of L^2 norm we get

$$\int_\Omega |I_x u + I_t|^2 d\mathbf{x} \leq \underline{lim}_{n \longrightarrow +\infty} \int_\Omega |I_x u_n + I_t|^2 d\mathbf{x}$$

$$\int_\Omega \Psi(|Du|) \leq \underline{lim}_{n \longrightarrow +\infty} \int_\Omega \Psi(|Du_n|),$$

That is

$$\bar{E}(u) \leq \underline{lim}_{n \longrightarrow +\infty} \bar{E}(u_n) = \inf_{v \in BV(\Omega)} \bar{E}(v)$$

i.e the u is minimum point of $\bar{E}(u)$.

Step 2: Uniqueness. Let u and v two minima of $\bar{E}(u)$ from the strict convexity of Ψ we easily get $Du = Dv$ which implies that $u = v + c_5$. But since functional $u \longrightarrow \int_\Omega |I_x u + I_t|^2$ is also strictly convex we deduce that $I_x u = I_x v$ which implies that $u = v$.

The major interest to introduce the regularized version of the energy functional $E(u)$ as $E_\beta(u)$ is that one can use the the smoothness parameter α as pointwise constant

function. From a numerical point of view, total variation is not straight forward to minimize, since it is not differentiable at zero therefore we refer a regularized version for the smoothness term in equation (3.1) as Ψ_β such that $\forall\beta, \Psi_\beta \geq 0$ and $\forall s, \lim_{\beta \longrightarrow 0} \Psi_\beta(s) = \Psi(s)$. The regularized version of energy functional $E(u)$ is introduced here as E_β for each $\beta > 0$, the associated minimization problem admit unique minimum in the Soblev space H^1. We recall the theoretical results on $\Gamma-$ convergence from [47] to prove that u_β converges in $L^1(\Omega)$ strong to the minimum of $\bar{E}(u)$. Following the same lines of [47] we approximate the smoothing term, using quadratic approximation.

$$\Psi_\beta(s) = \begin{cases} \frac{\Psi'(\beta)}{2\beta}s^2 + \Psi(\beta) - \frac{\beta\Psi'(\beta)}{2} & if\ 0 \leq s \leq \beta \\ \Psi(s) & if\ \beta \leq s \leq 1/\beta \\ \frac{\beta\Psi'(1/\beta)}{2}s^2 + \Psi(1/\beta) - \frac{\Psi'(1/\beta)}{2\beta} & if\ s \geq \beta \end{cases}$$

Various choices for selection of regularization function Ψ and its relaxed version Ψ_β are available in literature, we refer the interested reader to [5, 19, 18]. From scientific computing point of view, a widely used function is $\Psi_\beta(s) = \sqrt{\beta^2 + |\nabla u|^2}$ to approximate TV regularization. In order to cope with vanishing diffusivity and to make analysis of the continuous problem as well well as numerical analysis we modify the regularized version of $\Psi_\beta(s)$ by

$$\Psi_{\epsilon,\beta}(s) = \epsilon\,|\nabla u|^2 + \sqrt{\beta^2 + |\nabla u|^2}$$

where ϵ and β are strictly positive small regularization parameters. In fact, in addition to "good" regularization properties, such a function allows us to work in Hilbertian framework. we define the regularized version of functional $E_{\epsilon,\beta}$ as

$$E_{\epsilon,\beta}(u) = \begin{cases} \int_\Omega \epsilon\,|\nabla u|^2 + \alpha(\mathbf{x})\sqrt{\beta^2 + |\nabla u|^2}d\mathbf{x} + \int_\Omega (I_x u + I_t)^2 d\mathbf{x} & if u \in W^{1,2}(\Omega) \\ +\infty & \text{Otherwise} \end{cases}$$

Existence of minimizers of $E_{\epsilon,\beta}$ follows from direct methods of calculus of variations. we have the following result (see proof in [53, 79, 90])

Theorem 3.2 Using direct methods from calculus of variations the energy functional $E_{\epsilon,\beta}(u)$ attains minimum in H^1 space and satisfies the Euler-Lagrange equation.

$$0 = -\mathtt{div}\left(\epsilon\nabla u + \frac{\alpha(\mathbf{x})\nabla u}{\sqrt{\beta^2 + |\nabla u|^2}}\right) + (I_{x_1}^2 u + I_{x_1} I_t) \quad in \quad \Omega \tag{3.7}$$

where $\frac{\partial u}{\partial n} = 0$, on $\partial\Omega$,

For computational purpose, in finite dimensional settings we may set $\epsilon = 0$, moreover for analysis we may also set $\epsilon = 0$, at least when for the diffusion reaction equation (3.7), we are looking for a steady-state solution of gradient system

$$\partial_\rho u = -\mathtt{div}\left(\epsilon\nabla u + \frac{\alpha(\mathbf{x})\nabla u}{\sqrt{\beta^2 + |\nabla u|^2}}\right) + (I_{x_1}^2 u + I_{x_1} I_t) \quad in \quad \Omega \tag{3.8}$$

Here the ρ is considered as an artificial evolution parameter.

3.2.3 Variational Formulation

Typically the finite difference methods are proposed in literature to solve the nonlinear partial differential equation (3.7) like [19], instead we present a finite element method to solve this equation. A commonly used frame work to solve equation (3.7) is variational method this consists in defining a bilinear form $a_\alpha(u, v; u)$ and a linear form $(\mathbf{f}, v)$ such that the equation (3.7) is associated to following variational formulation.

Weak formulation: The weak formulation of (3.7) reads

Find a unction u in a Soblev space $H^1(\Omega; \mathbb{R})$ such that

$$\begin{cases} \text{Find } u \in H^1(\Omega; \mathbb{R}) \qquad \text{such that} \\ \int_\Omega \left(\epsilon + \frac{\alpha(\mathbf{x})}{\sqrt{\beta^2 + |\nabla u|^2}}\right)\nabla u : \nabla v d\mathbf{x} + \int_\Omega I_{x_1}^2 u \cdot v d\mathbf{x} = \int_\Omega \mathbf{f} \cdot v d\mathbf{x} \qquad \forall v \in H^1 \end{cases} \tag{3.9}$$

We introduce the notations for above formulation (3.9) as

$$a_\epsilon(u, v) = \epsilon \int_\Omega \nabla u : \nabla v d\mathbf{x} \tag{3.10}$$

$$a_\alpha(u, v; w) = \int_\Omega \alpha(\mathbf{x}) A(w)\nabla u : \nabla v d\mathbf{x} + \int_\Omega I_{x_1}^2 u \cdot v d\mathbf{x}. \tag{3.11}$$

$$(\mathbf{f}, v) = \int_\Omega \mathbf{f} \cdot v d\mathbf{x} \tag{3.12}$$

Problem (3.9) reduces to the following notation:

$$\begin{cases} \text{Find } u \in H^1(\Omega;\mathbb{R}) \qquad \text{such that} \\ \quad a_\epsilon(u,v) + a_\alpha(u,v;w) = (\mathbf{f},v) \end{cases} \tag{3.13}$$

Theorem 3.3 The problem (3.9) admits a unique weak solution.

Proof: The proof of theorem is similar to the proof in the discrete problem corresponding to therefore we postpone to the next chapter.

Chapter 4

Local and Adaptive selection of Parameters in TV regularization for Stereo-Vision Discrete Problems and Numerical Computations

4.1 Introduction

The efficient numerical solution of partial differential equations plays an important role in the state-of the-art technology. This demand and the ever increasing computational power from current computer hardware have brought the rapid development of numerical methods for partial differential equations, a development that encompasses convergence analyses and implementational aspects of software packages and programing languages like [43]. As in the previous chapter we discussed the modeling and analysis of nonlinear variational stereo model based on total variational regularization approach, in this chapter we consider the same TV stereo model to compute the dense disparity map between two consecutive frames of same stereo scene. TV regularization is one of the most popular regularization approaches for computer vision problems specially for image restoration [32, 76, 29] and variational stereo methods [7, 35]. This chapter is devoted to numerical analysis and implementation of TV stereo model (3.1) discussed in previous chapter. It is observed from the available literature on PDE's based approaches in image processing and computer vision [20, 19, 16, 18, 79, 17] that usually the practitioners use finite difference methods using structured grids for numerical solution of partial differential equations in image processing and computer vision. This thesis provides an efficient computational approach based on adaptive finite element method using triangular grid. Our work is based on a novel adaptive approach which provides an advanced computational strategy with low computational cost. The adaptive algorithm is a robust enhancement in computational strategies for computer vision and image processing problems. We present the theoretical analysis of discrete model, more over the numerical simulations and error estimation are the core of this chapter.

The major drawback of the variational methods is the reliability of computations at all locations. An obvious remedy is to refine the grid near the critical regions, i.e., to place more grid-points where the solution is less regular. The question then is how to identify those regions and how to obtain a good balance between the refined and unrefined regions such that the overall accuracy is optimal. The problem is to obtain the reliable estimates of the accuracy of the computed numerical solution. A priori error

estimates, as provided, e.g, by the standard error analysis for the finite element method or finite difference methods, are often insufficient since they only yield information on the asymptotic error behavior and require regularity conditions of the solution which are not satisfied in the presence of singularities like edges etc [88]. These considerations clearly show the need for an error estimator which can a posteriori be extracted from the computed numerical solution and the given data of the problem. Of course, the calculation of the a posteriori error estimate should be far less expensive than the computation of the numerical solution. Moreover, the error estimator should be local and should yield reliable upper and lower bounds for the true error in a user-specified norm. In this context one should note, that global upper bounds are sufficient to obtain a numerical solution with an accuracy below a prescribed tolerance. Local lower bounds, however, are necessary to ensure that the grid is correctly refined so that one obtains a numerical solution with a prescribed tolerance using a (nearly) minimal number of grid-points. Typically the image grids are already refined so no further refinement is necessary using standard mesh adaption algorithms available in literature like [88]. As we discussed already that deriving a posteriori error estimator, we propose a new mesh adaptive strategy as given in [12], which is performed by a posteriori error estimates which are equivalent to discretization error in appropriate norm and includes an implicit confidence measure. Effects of regularization by weight α here are shown using different values of α as constant parameter as well as with the mesh adaptive algorithm given in [12], by considering the weight function $\alpha(\mathbf{x})$ as scalar pointwise function on the grid depending on a posteriori estimates introduced in [12]. This work is an extension as a nonlinear case for one dimensional flow of a presentation given there in [12]. To compare our results with image community, existing ones in present literature [20], we compute numerical error called absolute average error. Our aim is to provide an efficient and accurate numerical analysis for a given nonlinear stereo model. All the computations are performed using FreeFem++ [43]. In addition to improve the computational results we also build a "good" mesh on computed disparity.

4.2 Problem Discretization

Suppose that the domain Ω is polygonal and let we consider a regular family of triangulations $\mathcal{T}_h$ made up of elements which are triangles (or quadrilaterals) with maximum size $h > 0$, satisfying the usual admissibility assumptions, i.e:

Admissibility: the intersection of two different elements is either empty, a vertex, or a whole edge.

Shape regularity: The ratio of the diameter of any element $K \in \mathcal{T}_h$ denoted by h_K to the diameter of its largest inscribed ball denoted by ρ_K is bounded independently of K. We denoted the shape parameter as $C_\tau = \max_{K\in\tau} \frac{h_K}{\rho_K}$ Given element $K \in \mathcal{T}$, we define K^* as the union of all elements in $\mathcal{T}_h$ that share atleast one side with K, and $B_h(K)$ as union of all elements in $\mathcal{T}_h$ that have empty intersection with K. We introduce the following discrete space as $X_h \subset X$, which denotes the space of continuous piecewise affine finite elements over $\mathcal{T}_h$, that is

$$X_h := \left\{ v_h \in C^0(\bar{\Omega}) | \forall K \in \mathcal{T}_h, v_{h|T} \in P_1(K) \right\}$$

where $P_1(K)$ denotes space of all polynomials in $\mathbb{R}^2$ of degree equal to one.

The discrete formulation reads

$$\begin{cases} \text{Find } \; u_h \in X_h \; \text{ such that} \\ a_\epsilon(u_h, v_h) + a_\alpha(u_h, v_h; w_h) = (\mathbf{f}, v_h) \qquad \forall v_h \in X_h \end{cases} \tag{4.1}$$

where

$$a_\epsilon(u_h, v_h) = \epsilon \int_\Omega \nabla u_h : \nabla v_h d\mathbf{x} \tag{4.2}$$

and

$$a_\alpha(u_h, v_h; w_h) = \int_\Omega \alpha\, A(w_h) \nabla u_h : \nabla v_h \, d\mathbf{x} + \int_\Omega I^2_{x_1} u_h \cdot v_h \, d\mathbf{x} \tag{4.3}$$

and

$$(\mathbf{f}, v_h) = \int_\Omega \mathbf{f} \cdot v_h \, d\mathbf{x} \tag{4.4}$$

For given $\mathcal{K} > 0$, let

$$X_h^{\mathcal{K},p} = \{ v \in X_h, \, \|v\|_{W^{1,p}} \leq \mathcal{K} \} \tag{4.5}$$

We define the iteration map, $T_h : X_h^{\mathcal{K},p} \longrightarrow X_h^{\mathcal{K},p}$ via

$$a_\epsilon(T_h u_h, v_h) + a_\alpha(T_h u_h, v_h; w_h) = (\mathbf{f}, v_h) \qquad \forall v_h \in X_h^{\mathcal{K},p} \tag{4.6}$$

T_h is well defined because $u_h \in X_h^{\mathcal{K},p}$ implies $A(s) \in L^\infty(\Omega)$. In order to obtain the error estimates with constants independent of α we introduce the norm

$$\|u\|_{2,\alpha} = \left(\int_\Omega \alpha^{\frac{1}{2}} |\nabla u|^2 + \left| f_x^{\frac{1}{2}} u \right|^2 \right)^{\frac{1}{2}}$$

Before to prove result for existence we recall the Boruwer's fixed point theorem and following corollary 4.2. from [48].

Theorem 4.1.(Brouwer) Let C denote a non-void, convex and compact subset of finite dimensional space and let F be a continuous mapping from C to C. Then F has atleast one fixed point.

Corollary 4.2. Let H be a finite-dimensional Hilbert space whose scalar product is denoted by $(\cdot, \cdot)$. and corresponding norm $|\cdot|_.$. Let Φ be a continuous mapping from H to H with following property:
there exists $\mu > 0$ such that

$$(\Phi(f), f) \geq 0 \text{ for all } f \in H \text{ with } |f| = \mu. \tag{4.7}$$

Then there exist an element f such that

$$\Phi(f) = 0 \tag{4.8}$$

We now give the existence result in $W^{1,p}$ for $p > 2$

Theorem 4.3. There exist $\mathcal{K} > 0$, $p > 2$, h_0 and δ such that for any $\mathbf{f}$ satisfying $\|\mathbf{f}\|_{W^{-1,p}(\Omega)} \leq \delta$, and for all $0 < h \leq h_0$, the map T_h maps $X_h^{\mathcal{K},p}$ into it self.

Proof: We note that $u_h \in X^{\mathcal{K},p}$ implies $A(u_h)$ is bounded, therefore it follows from Meyer's result[46], the gradient estimate in linear case, we have for $\frac{1}{q} = 1 - \frac{1}{p}$

$$\begin{aligned} \|T_h u_h\|_{W^{1,p}(\Omega)} &\leq C \sup_{0 \neq v_h \in X_h} \frac{a_\epsilon(T_h u_h, v_h) + a_\alpha(T_h u_h, v_h; w_h)}{|v_h|_{W^{1,q}(\Omega)}} \\ &= C \sup_{0 \neq v_h \in X_h} \frac{(\mathbf{f}, v_h)}{|v_h|_{W^{1,q}(\Omega)}} \\ &\leq C \|\mathbf{f}\|_{W^{-1,p}(\Omega)} \end{aligned} \tag{4.9}$$

choosing $\delta = \frac{\mathcal{K}}{C}$ yields the result. $\square$

In order to proceed for the existence theorem we prove the following lemma

Lemma 4.4. Given $p > 2$ the map $T_h : X_h^{\mathcal{K},p} \longrightarrow X_h^{\mathcal{K},p}$ is lipschitz continuous, provided that A is lipschitz continuous.

Proof: For $v, w, \phi \in X_h$ we have

$$\begin{aligned} a_\epsilon(T_h v - T_h w, \phi) + a_\alpha(T_h v - T_h w, \phi; w) &= a_\epsilon(T_h v, \phi) + a_\alpha(T_h v, \phi; w) - a_\epsilon(T_h w, \phi) - a_\alpha(T_h w, \phi; w) \\ &= a_\epsilon(T_h v, \phi) + a_\alpha(T_h v, \phi; w) - (\mathbf{f}, \phi) \\ &= \epsilon \int_\Omega \nabla T_h v : \nabla \phi \, d\mathbf{x} + \int_\Omega \alpha \left(A(w) \nabla T_h v : \nabla \phi \, d\mathbf{x}\right. \\ &+ \int_\Omega I_{x_1}^2 T_h v \cdot \phi \, d\mathbf{x} - \epsilon \int_\Omega \nabla T_h v : \nabla \phi \, d\mathbf{x} \\ &- \int_\Omega \alpha \left(A(v) \nabla T_h v : \nabla \phi \, d\mathbf{x} - \int_\Omega I_{x_1}^2 T_h v \cdot \phi \, d\mathbf{x}\right. \end{aligned}$$

(4.10)

Therefore one can write the above equation as:

$$a_\epsilon(T_h v - T_h w, \phi) + a_\alpha(T_h v - T_h w, \phi; w) = \int_\Omega \alpha \left(A(w) - A(v)\right) \nabla T_h v : \nabla \phi \, d\mathbf{x} \tag{4.11}$$

(4.12)

$$|a_\epsilon(T_h v - T_h w, \phi) + a_\alpha(T_h v - T_h w, \phi; w)| = \left| \int_\Omega \alpha \left(A(w) - A(v)\right) \nabla T_h v : \nabla \phi \, d\mathbf{x} \right|$$

$$\leq \int_\Omega \alpha \, |A(w) - A(v)| \, |\nabla T_h v : \nabla \phi| \, d\mathbf{x}$$

$$\leq \alpha_{\max} \|A\|_{W^{1,\infty}(I)} \| |w - v| \, |\nabla T_h v| \|_{L^2(\Omega)} \|\nabla \phi\|_{L^2(\Omega)}$$

(Cauchy-Shwarz inequality)

$$\leq \alpha_{\max} \|A\|_{W^{1,\infty}(I)} \|w - v\|_{L^q(\Omega)} \|\nabla T_h v\|_{L^p(\Omega)} \|\phi\|_{H^1(\Omega)}$$

(Hölder's inequality $q = 2p/p - 2$)

$$\leq \alpha_{\max} \|A\|_{W^{1,\infty}(I)} \, c_p' \, \|w - v\|_{H^1(\Omega)} \|T_h v\|_{W^{1,p}(\Omega)} \|\phi\|_{H^1(\Omega)} \text{ (Sobolev inequality)}$$

choosing $\phi = T_h w - T_h v$ we have the following result

$$\|T_h w - T_h v\|_{H^1(\Omega)} \leq \frac{\alpha_{\max} c_p' \|A\|_{W^{1,\infty}}(I) \mathcal{K}}{\epsilon \alpha_{\min}} \|w - v\|_{H^1(\Omega)} \tag{4.13}$$

where $I = \left[0, \max\left\{M, \|u_h\|_{L^\infty(\Omega)}\right\}\right]$.

From the Brouwer Theorem 4.1 and lemma 4.4, we have the following result.

Theorem.4.5. Let $\mu > 0, \mathcal{K}$, $p > 2$, $h_0 > 0$, $C > 0$ and $\delta > 0$ as in theorem (4.3), then problem (4.1) admits a unique solution.

Remark.4.6:

T_h is Lipschitz continuous therefore one can apply the Brouwer's fixed point theorem which guaranties the convergence of fixed point iteration:

$$u_h^{n+1} = T_h u_h^n$$

$u_h^n \longrightarrow u_h$ as $n \longrightarrow \infty$

Remark:4.7

For the continuous weak problem (3.9) one can define T similarly as T_h. Under the hypothesis of the theorem 4.3 the similar result can be proved for T. Then for small $\mathcal{K}$ with appropriate choice of δ one can prove the existence and uniqueness of the continuous weak problem (3.9) using contraction principle.

Case: p=2: We recall Brouwer fixed-point theorem and define a map $\Phi : X_h \longrightarrow X_h$ as

$$(\Phi(w), v) = a_\epsilon(w, v) + a_\alpha(w, v; w) - (\mathbf{f}, v), \ \forall w, v \in X_h \tag{4.14}$$

$a_\epsilon + a_\alpha$ solves the problem (4.1) if and only if $\Phi(u_h) = 0$. It follows from the ellipticity of $a_\epsilon(w, v) + a_\alpha(\cdot, v; \cdot)$ that

$$(\Phi(w), w) \geq \left(C \|w\|_{H^1(\Omega)} - \|\mathbf{f}\|_{L^2(\Omega)}\right) \|w\|_{H^1(\Omega)} \tag{4.15}$$

choosing $\mu = \frac{1}{C} \|\mathbf{f}\|_{L^2(\Omega)}$, we have $\forall\ w \in X_h$

$$\|w\|_{H^1(\Omega)} = \mu$$

we get

$$(\Phi(w), w) \geq 0$$

Moreover Φ is continuous in X_h and thus we may apply corollary 4.2.

Considering the case $p = 2$, we proceed with the Galerkin approximation method, we construct sequence of approximate solutions, since H^1 is a separable space, there exist

(1.) A sequence $(w_m)_{m\geq 1}$ in H^1 such that $(w_m)_{m\geq 1}$ is a basis of $H^1(\Omega)$. We denote by X_m the finite dimensional space spanned by $w_1, \cdots w_m$. Then we have the following approximation problem

$$\begin{cases} \text{Find } \ u_m \in X_m \ \text{ such that} \\ a_\epsilon(u_m, v) + a_\alpha(u_m, v; u_m) = (\mathbf{f}, v) \qquad \forall v \in X_m \end{cases} \tag{4.16}$$

if we set $u_m = \sum_{i=1}^m \lambda_i w_i$. applying corollary 4.2 we have

$$0 = (\Phi(u_m), u_m) \geq (C \left\|u_m\right\|_{H^1(\Omega)} - \left\|\mathbf{f}\right\|_{L^2(\Omega)}) \left\|u_m\right\|_{H^1(\Omega)}$$

which gives

$$\left\|u_m\right\|_{H^1(\Omega)} \leq \frac{1}{C} \left\|\mathbf{f}\right\|_{L^2(\Omega)}. \tag{4.17}$$

(2.) It follows from (4.17) that the sequence (u_m) is bounded in $H^1(\Omega)$. Therefore we can extract a subsequence $(u_m)_m$ such that $u_m \rightharpoonup u^*$ weakly in $H^1(\Omega)$.
Since $u \longmapsto a_\epsilon(u, v) + a_\alpha(u, v; u)$ is weakly sequentially continuous we have

$$\lim_{m \longrightarrow \infty} a_\epsilon(u_m, v) + a_\alpha(u_m, v; u_m) = a_\epsilon(u^*, v) + a_\alpha(u^*, v; u^*)$$

u^* is the solution of (4.16), taking $v = u_m$ we have

$$a_\epsilon(u^*, u_m) + a_\alpha(u^*, u_m; u^*) = (\mathbf{f}, u_m) \ m \geq 1$$

and u_m is basis of $H^1(\Omega)$ which yields the result.
(3.) The uniqueness follows from the uniform ellipticity of $a_\epsilon(.,.) + a_\alpha(.,.;.)$. □

4.3 Error estimates

Theorem 4.8. Suppose that $A(s)$ is Lipschitz continuous. There exist $\delta > 0$, $h_0 > 0$ and $p > 2$ the problems (3.9) and (4.1), have unique solutions for any $\mathbf{f}$ such that $\left\|\mathbf{f}\right\|_{W^{-1,p}(\Omega)} \leq \delta$. Moreover, there exist $C > 0$ not depending on h such that

$$\left\|u - u_h\right\|_{H^1(\Omega)} \leq C \left\|u - v\right\|_{H^1(\Omega)} \tag{4.18}$$

Proof:

$$\begin{aligned} a_\epsilon(u-u_h,v)+a_\alpha(u-u_h,v;u_h) &= a_\epsilon(u,v)+a_\alpha(u,v;u_h)-a_\epsilon(u_h,v)-a_\alpha(u_h,v;u_h)\ \ \forall v\in X_h \\ &= a_\epsilon(u,v)+a_\alpha(u,v;u_h)-(\mathbf{f},v) \\ &= \epsilon\int_\Omega \nabla u:\nabla v\,d\mathbf{x}+\int_\Omega \alpha\,(A(u_h)\nabla u:\nabla v\,d\mathbf{x}+\int_\Omega I^2_{x_1}u\cdot v\,d\mathbf{x} \\ &- \epsilon\int_\Omega \nabla u:\nabla v\,d\mathbf{x}-\int_\Omega \alpha\,(A(u)\nabla u:\nabla v\,d\mathbf{x}-\int_\Omega I^2_{x_1}u\cdot v\,d\mathbf{x} \end{aligned} \tag{4.19}$$

Therefore one can write the above equation as:

$$a_\epsilon(u-u_h,v)+a_\alpha(u-u_h,v;u_h)=\int_\Omega \alpha\,(A(u_h)-A(u))\nabla u:\nabla v\,d\mathbf{x} \tag{4.20}$$

Assuming $u\in W^{1,p}(\Omega)$ and $A\in W^{1,\infty}(I)$ for any bounded interval $I\subset\mathbb{R}$, we find for any $v\in X_h$

$$a_\epsilon(u-u_h,v)+a_\alpha(u-u_h,u-u_h;u_h)=a_\epsilon(u-u_h,v)+a_\alpha(u-u_h,u-v;u_h)+a_\alpha(u-u_h,v-u_h;u_h)$$

$$= a_\alpha(u-u_h,u-v;u_h)+\int_\Omega \alpha\,(A(u_h)-A(u))\nabla u:\nabla(v-u_h)\,d\mathbf{x}$$

(From equation (4.20))

$$\leq \alpha_{\max}M\,\|u-u_h\|_{H^1}\,\|u-v\|_{H^1}+\int_\Omega \alpha\ |A(u)-A(u_h)|\,|\nabla u:\nabla(v-u_h)|\ d\mathbf{x}$$

(Cauchy-Shwarz inequality)

$$\leq \alpha_{\max}M\,\|u-u_h\|_{H^1}\,\|u-v\|_{H^1}+\|A\|_{W^{1,\infty}(I)}\int_\Omega \alpha\ |u-u_h|\,|\nabla u:\nabla(v-u_h)|\ d\mathbf{x}$$
$$\leq \alpha_{\max}M\,\|u-u_h\|_{H^1}\,\|u-v\|_{H^1}+\alpha_{\max}\|A\|_{W^{1,\infty}(I)}\,\||u-u_h|\,|\nabla u|\|_{L^2(\Omega)}\,\|v-u_h\|_{H^1}$$

(Cauchy-Shwarz inequality)

$$\leq \alpha_{\max}M\,\|u-u_h\|_{H^1}\,\|u-v\|_{H^1}+\alpha_{\max}\|A\|_{W^{1,\infty}(I)}\,\|u-u_h\|_{L^q(\Omega)}\,\|u\|_{W^{1,p}(\Omega)}\,\|v-u_h\|_{H^1}$$

(Hölder's inequality)

$$\leq \alpha_{\max}M\,\|u-u_h\|_{H^1}\,\|u-v\|_{H^1}+\alpha_{\max}\|A\|_{W^{1,\infty}(I)}\,c'_p\,\|u-u_h\|_{H^1(\Omega)}\,\|u\|_{W^{1,p}(\Omega)}\,\|v-u_h\|_{H^1}$$

(Sobolev's Inequality)

$$\leq \alpha_{\max}\,\|u-u_h\|_{H^1}\left(M\,\|u-v\|_{H^1}+c'_p\,\|A\|_{W^{1,\infty}(I)}\,\|u\|_{W^{1,p}(\Omega)}\,\|v-u_h\|_{H^1}\right)$$

Sobolev's inequality is used where $I = \left[0, \max\left\{M, \|u\|_{L^\infty(\Omega)}\right\}\right]$ and $q = 2p/(p-2)$. Therefore:

$$\begin{aligned}\|u-u_h\|_{H^1} &\leq \frac{\alpha_{\max}}{\epsilon\alpha_{min}}\left(M\|u-v\|_{H^1} + c_p'\|A\|_{W^{1,\infty}(I)}\|u\|_{W^{1,p}(\Omega)}\|v-u_h\|_{H^1}\right)\\ &\leq \frac{\alpha_{\max}}{\epsilon\alpha_{\min}}\left(M\|u-v\|_{H^1} + c_p'\|A\|_{W^{1,\infty}(I)}\|u\|_{W^{1,p}(\Omega)}\left(\|v-u\|_{H^1} + \|u-u_h\|_{H^1}\right)\right)\end{aligned}$$

(Triangle inequality)

We find:

$$(1-\gamma)\|u-u_h\|_{H^1} \leq \left(\frac{\alpha_{\max}M}{\epsilon\alpha_{\min}} + \gamma\right)\|u-v\|_{H^1}$$

where

$$\gamma := \frac{\alpha_{\max}c_p'}{\epsilon\alpha_{\min}}\|A\|_{W^{1,\infty}(I)}\|u\|_{W^{1,p}(\Omega)}$$

Thus if $\gamma < 1$ we have the following result

$$\|u-u_h\|_{H^1} \leq \left(\frac{\alpha_{\max}M + \gamma\epsilon\alpha_{\min}}{\epsilon\alpha_{\min}(1-\gamma)}\right)\|u-v\|_{H^1} \tag{4.21}$$

which yields the result, where M and c_p satisfy following inequalities.

$$\|A(v)\|_{L^\infty(\Omega)} \leq M$$

$$\|v\|_{L^\infty} \leq c_p\|v\|_{W^{1,p}(\Omega)} \ \forall v \in W^{1,p}(\Omega)$$

□

Remark: Under the hypothesis of theorem.4.3 if $u \in W^{k,p}(\Omega)$ the following result is valid see [26]

$$\|u-u_h\|_{W^{1,p}} \leq Ch^{k-1}\|u\|_{W^{k,p}} \tag{4.22}$$

4.4 A posteriori estimates

For the a posteriori error estimates we assume that $\mathbf{f} \in L^2(\Omega)$ and we fix $\mathbf{f}_h$ a finite element approximation of it associated with $\mathcal{T}_h$. We denote by $\mathcal{E}_K$ the set of its edges not contained in the boundary $\partial\Omega$. The union of all $\mathcal{E}_K$, $K \in \mathcal{T}_h$ is denoted by $\mathcal{E}_h$. With each edge $e \in \mathcal{E}_h$, we associate a unit vector $\mathbf{n}_e$ normal to e and we denote by

$[\phi]_e$ the jump of the piecewise continuous function ϕ across e in the direction $\mathbf{n}_e$. For each $K \in \mathcal{T}_h$ we denote by h_K the diameter of K and we denote by h_e the diameter of e, where $e \in \mathcal{E}_K$.

Let $u_h \in X_h$ be the finite element approximation of u as in in (4.1). We propose following a posteriori residual error indicators as given in [12, 44, 88], which is an upper bound for error in $L^2(\Omega)$. For sake of simplicity we choose $\epsilon = 0$. For each element $K \in \mathcal{T}_h$ we define the error indicator η_K in L^p norm as

$$\begin{aligned}\eta_K^{p,q} &= h_K^{d+1-(\frac{d}{2}+\frac{d}{p})} \left\| I_{x_1}^2 u_h - \mathbf{f}_h \right\|_{L^p(K)} \\ &\quad + \frac{1}{2} \sum_{e \in \mathcal{E}_h} h_e^{d-\frac{1}{2}-(\frac{d-1}{2}+\frac{d-1}{q})} \left\| [\alpha\, a(\nabla u_h) \cdot \mathbf{n}_e]_e \right\|_{L^q(e)}\end{aligned} \tag{4.23}$$

From computational point of view it is more practical to present this above error indicator in $L^2(\Omega)$ norm, for $p = q = 2$ and $d = 2$ and we modify the definition of η_k taking into account α and obtain the indicators which are insensitive to jump in α.

$$\eta_K = \alpha_K^{-1/2}\, h_K \left\| I_{x_1}^2 u_h - \mathbf{f}_h \right\|_{L^2(K)} + \frac{1}{2} \sum_{e \in \mathcal{E}_h} \alpha_e^{-\frac{1}{2}}\, h_e^{\frac{1}{2}} \left\| [\alpha\, a(\nabla u_h) \cdot \mathbf{n}_e]_e \right\|_{L^2(e)} \tag{4.24}$$

Where h_K is the diameter of $K \in \mathcal{T}_h$ and h_e is denoted as size of edge $e \in \mathcal{E}_h$(set of edges in $\mathcal{T}_h$). $\mathbf{n}_e$ is denoted as unit vector normal to the edge e. $[\cdot]$ denotes the jump over the edge between two elements.

For simplicity we introduce the functions $B : \mathbb{R}^2 \longrightarrow \mathbb{R}$ and $a : \mathbb{R}^2 \longrightarrow \mathbb{R}^2$

$$B(p) = \sqrt{1 + |p|^2} \text{ and } a(p) = \frac{p}{\sqrt{1 + |p|^2}}$$

Let ω be the subdomain of Ω and following the same lines of [44] we introduce the following error notation $e_{\alpha,w}(u, v)$ as

$$e_{\alpha,\omega}(u, v) = \left(\int_\omega \alpha \left| N(\nabla u) - N(\nabla v) \right|^2 \frac{B(\nabla u) + B(\nabla v))}{2} + \int_\omega I_{x_1}(u - v)^2 \right)^{\frac{1}{2}} \tag{4.25}$$

Where $N(p) = (p, -1)/\sqrt{1 + |p|^2} \in \mathbb{R}^3$ for $p \in \mathbb{R}^2$. We assume here that $u \in W^{1,\infty}(\Omega)$. From the convexity of $J(u)$ we note that the following inequality holds see [75]

$$0 \leq J(u_h) - J(u) \leq e_\Omega(u_h, u)^2$$

where $J(u)$ is denoted as

$$J(u) = \int_\Omega \left(\alpha(x) B(u) + (I^2 u + I_t)^2 \right) d\mathbf{x}$$

Residual: Let $X = H^1$ equipped with the weighted norm $\|\cdot\|_{1,\alpha}$ associated to the scalar product:

$$(u, v)_\alpha = \int_\Omega \alpha \nabla u : \nabla v d\mathbf{x} + \int_\Omega u \cdot v d\mathbf{x}$$

We denote X^* as the dual norm of X as

$$\|v\|_* = \mathrm{Sup} \frac{(u, v)_\alpha}{\|u\|_{1,\alpha}}$$

We define the residual $R(u_{\alpha,h}) \in X^*$ as for $v \in X$

$$\langle \mathbf{R}(u_h), v \rangle = a_\alpha(u_h, v; u_h) - (\mathbf{f}, v) \tag{4.26}$$

equation (4.1) for u_h means

$$\forall v_h \in X_h \ \langle \mathbf{R}(u_h), v_h \rangle = 0 \tag{4.27}$$

From (4.26) we have

$$\forall v \in X, \ \langle \mathbf{R}(u_h), v \rangle = \int_\Omega \alpha(a(\nabla u_h) - a(\nabla u))\nabla v + \int_\Omega I_{x_1}^2 (u_h - u)\, v \, d\mathbf{x} \tag{4.28}$$

Thus

$$\langle \mathbf{R}(u_h), u - u_h \rangle = e_\Omega(u_h, u)^2 \tag{4.29}$$

Integrating by parts the equation (4.26) on each element K

(4.30)

$$\langle \mathbf{R}(u_h), v \rangle = \sum_{K \in \mathcal{T}_h} \int_K I_{x_1}^2 u \, v - \int_K \mathbf{f} \, v - \frac{1}{2} \sum_{K \in \mathcal{T}_h} \int_{\partial K} (\alpha \, a(\nabla u_h) \nabla u_h \cdot \mathbf{n}_e) \, v,$$

$$= \sum_{K \in \mathcal{T}_h} \int_K (I_{x_1}^2 u - \mathbf{f}_h) \, v + \int_K (\mathbf{f}_h - \mathbf{f}) \, v - \frac{1}{2} \sum_{e \in \mathcal{E}_h} \int_e (\alpha \, a(\nabla u_h) \cdot \mathbf{n}_e) \, v, \tag{4.31}$$

where Ω is partitioned in to elements K and $\mathbf{n}_e$ is the outward-pointing unit normal to the boundary of K is denoted as ∂K.

Note: That for linear elements the terms containing second order derivatives vanish.

where $e \in \mathcal{E}_h$, here $\mathcal{E}_h$ is the set of edges of triangulation $\mathcal{T}_h$. $[\cdot]$ denotes jump over the edge between two elements say K_1 and K_2

$$[\nabla u_h \cdot \mathbf{n}_e]_e = (\nabla u_h|_{K_1} - \nabla u_h|_{K_2}) \cdot \mathbf{n}_2$$

$$[\alpha a(\nabla u_h)\cdot \mathbf{n}_e]_e = (\alpha_{K_1} a(\nabla u_h)\nabla u_h|_{K_1} - \alpha_{K_2} a(\nabla u_h)\nabla u_h|_{K_2})\cdot \mathbf{n}_2$$

where K_1, $K_2 \in \mathcal{T}_h$ containing S and n_2 is exterior normal of K_2. The error orthogonality of the Galerkin method allows us to replace v on the left-hand side of (4.31) by $v - v_h$. To continue, we would like to choose v_h in such a way that we can bound $v - v_h$ for any $v \in X$, but we can not use a standard interpolant because it is not in general defined for $v \in X$. This is technical difficulty. To handle such difficulties we recall local interpolants [44].

Interpolant error estimates.

Let $\Pi_h : X \longrightarrow X_h$ be interpolation operator, to define such an interpolant and to formulate approximation error estimates, let us define the following notation:

- ω_K: the set of all elements that share at least one vertex with the element K.
- ω_e: the set of all elements that share at least one vertex with edge e.
- set: $\Pi_h v := \sum_j (P_j v)(x_j)\phi_j$ where $\{\phi_j\}$ is the usual nodal basis for X_h and P_j denotes the the $L^2(\omega_{x_j})$ projection from X to the space of the polynomial of degree at most one.

We assume that the triangulation is quasi-uniform, which implies that the number of elements in ω_K or ω_e is bounded by a fixed constant. We propose the the following standard local error estimates as given in [44]:

Proposition 4.9. For any $r, q \in [1, \infty[$, $K \in \mathcal{T}_h$ and $e \in \mathcal{E}_h$, we have $v \in X$ corresponds a local interpolant $\Pi_h\, v \in X_h$ such that

$$\|v - \Pi_h v\|_{0,r;K} \leq C'\, h_K^{1-d/q+d/r}\, |\nabla v|_{0,q;\omega_K} \text{ if } -d/r \leq 1 - d/q, \tag{4.32}$$

and

$$\|v - \Pi_h v\|_{0,q;e} \leq C''\, h_e^{1/q}\, |\nabla v|_{0,q;\omega_e} \text{ if } e \subset \mathcal{E}_h. \tag{4.33}$$

$\|\cdot\|_{m,p;\Omega}$ denotes the norm in $W^{m,p}$ Sobolev space over an arbitrary domain Ω [11]. With $d = q = r = 2$ we have

$$\|v - \Pi_h v\|_{0,2;K} \leq C' \alpha_K^{-\frac{1}{2}} h_K \left|\alpha^{\frac{1}{2}} \nabla v\right|_{0,2;\omega_K} \tag{4.34}$$

and

$$\|v - \Pi_h v\|_{0,2;e} \leq C'' \alpha_e^{-\frac{1}{2}} h_e^{\frac{1}{2}} \left|\alpha^{\frac{1}{2}} \nabla v\right|_{0,2;\omega_e} \tag{4.35}$$

4.4.1 An upper bound of error

From (4.29) and

$$\langle \mathbf{R}(u_h), u - u_h \rangle \leq \|\mathbb{R}(u_h)\|_* \left|\alpha^{1/2} \nabla (u - u_h)\right|_{0,2;\Omega} \tag{4.36}$$

let we assume that for some fixed $M > 0$, the following inequality holds

$$|\nabla (u_h - u)|_{0,\infty;\Omega} \leq M \tag{4.37}$$

then from the inequality

$$|s\nabla u_h + (1-s)\nabla u| \leq |\nabla u| + M \quad \text{for } s \in [0,1]$$

we deduce

$$e_\Omega^2(u_h, u) = \int_\Omega \int_0^1 \alpha D^2 B(s\nabla u_h + (1-s)\nabla u)\nabla(u_h - u) ds$$

we get

$$\inf \lambda^M(\nabla(u)) \left\|\alpha^{1/2} \nabla (u_h - u)\right\|_{0,2;\Omega}^2 \leq e_\Omega(u_h, u)^2 \tag{4.38}$$

where $\lambda(p)$ is the minimum eigenvalue of $D^2 B(p)$. With $rs \leq \frac{\epsilon}{2} r^2 + \frac{1}{2\epsilon} s^2$ where $r, s \geq 0, \epsilon > 0$ we get

$$\begin{aligned} \langle \mathbf{R}(u_h), u - u_h \rangle &\leq \underbrace{\lambda^{-1} \|\mathbf{R}(u_h)\|_*}_{s} \underbrace{\lambda \left\|\alpha^{1/2} \nabla (u_h - u)\right\|_{0,2;\Omega}}_{r} \\ &\leq \frac{1}{4} e_\Omega^2(u_h, u) + \lambda^{-1} \|\mathbf{R}(u_h)\|_*^2 \text{ with } \epsilon = 1/2 \end{aligned} \tag{4.39}$$

using (4.29) we have

$$e_\Omega(u_h, u) \leq \left(\frac{4}{3} \lambda^{-1} \|\mathbf{R}(u_h)\|_*^2\right)^{1/2} \tag{4.40}$$

Let $v \in X$ and $\Pi_h v$ to be its interpolant, using (4.27) and error estimates (4.34), (4.35) yield

$$
\begin{aligned}
(4.41) \qquad \langle \mathbf{R}(u_h), v\rangle &= \langle \mathbf{R}(u_h), v - \Pi_h v\rangle \\
&= \sum_{K\in\mathcal{T}_h} \int_K (I_{x_1}^2 u - \mathbf{f}_h)(v - \Pi_h v) + \int_K (\mathbf{f}_h - \mathbf{f})(v - \Pi_h v) \\
&- \frac{1}{2} \sum_{e\in\mathcal{E}_h} \int_e (\alpha\, a(\nabla u_h)\cdot \mathbf{n}_e)(v - \Pi_h v)
\end{aligned}
$$

hence

$$
\begin{aligned}
\langle \mathbf{R}(u_h), v\rangle &\le \sum_{K\in\mathcal{T}_h} \left\| I_{x_1}^2 u - \mathbf{f}_h \right\|_{0,2;K} \|v - \Pi_h v\|_{0,2;K} + \|\mathbf{f} - \mathbf{f}_h\|_{0,2;K} \|v - \Pi_h v\|_{0,2;K} \\
&+ \frac{1}{2} \sum_{e\in\mathcal{E}_h} \|\alpha\, a(\nabla u_h)\cdot \mathbf{n}_e\|_{0,2;e} \|v - \Pi_h v\|_{0,2;e} \cdot \\
&\le \sum_{K\in\mathcal{T}_h} c_1 \alpha_K^{-\frac{1}{2}} h_K \left\| I_{x_1}^2 u - \mathbf{f}_h \right\|_{0,2;K} \left\| \alpha^{\frac{1}{2}} \nabla v \right\|_{0,2;\omega_K} \\
&+ \sum_{K\in\mathcal{T}_h} c_1 \alpha_K^{-\frac{1}{2}} h_K \|\mathbf{f} - \mathbf{f}_h\|_{0,2;K} \left\| \alpha^{\frac{1}{2}} \nabla v \right\|_{0,2;\omega_K} \\
&+ \frac{1}{2} \sum_{e\in\mathcal{E}_h} c_2 \alpha_e^{-\frac{1}{2}} h_e^{\frac{1}{2}} \|\alpha\, a(\nabla u_h)\cdot \mathbf{n}_e\|_{0,2;e} \left\| \alpha^{\frac{1}{2}} \nabla v \right\|_{0,2;\omega_e} \\
&\le \max(c_1, c_2) \left\{ \sum_{K\in\mathcal{T}} \eta_K^2 + \alpha_K^{-\frac{1}{2}} h_K \|\mathbf{f} - \mathbf{f}_h\|_{0,2;K} \right\}^{\frac{1}{2}} \times \\
&\left\{ \sum_{K\in\mathcal{T}_h} \left\| \alpha^{\frac{1}{2}} \nabla v \right\|_{0,2;\omega_K} + \left\| \alpha^{\frac{1}{2}} \nabla v \right\|_{0,2;\omega_e} \right\}^{\frac{1}{2}} \\
(4.42) \qquad &\le C_{\mathcal{T}} \max(c_1, c_2) \left\{ \sum_{K\in\mathcal{T}} \eta_K^2 + \alpha_K^{-\frac{1}{2}} h_K \|\mathbf{f} - \mathbf{f}_h\|_{0,2;K} \right\}^{\frac{1}{2}} \left\| \alpha^{1/2} \nabla v \right\|_{0,2;\Omega}
\end{aligned}
$$

This bound is the upper bound for residual, where

$$
(4.43) \qquad \eta_K = \alpha_K^{-1/2} h_K \left\| I_{x_1}^2 u_h - \mathbf{f}_h \right\|_{L^2(K)} + \frac{1}{2} \sum_{e\in\mathcal{E}_h} \alpha_e^{-\frac{1}{2}} h_e^{\frac{1}{2}} \|[\alpha\, a(\nabla u_h)\mathbf{n}_e]_e\|_{L^2(e)}
$$

The error estimator η_K is computable, local and-by-its construction reliable. One can find some abstract theoretical results for upper and lower bounds of error $e_\Omega(u, u_h)$ in the terms of this local error indicator η_K for this particular class of nonlinear problems in [44, 88].

Combining the results (4.29),(4.36), (4.40), and (4.42) we have the following result

$$
(4.44) \qquad e_\Omega(u_h, u) \le \left(\frac{\sum_K \eta_K^2}{\inf_\Omega \lambda^M(\nabla u)} \right)^{\frac{1}{2}} + \frac{\alpha_K^{-\frac{1}{2}} h_K}{\inf_\Omega \lambda^M(\nabla u)} \left(\|\mathbf{f} - \mathbf{f}_h\|_{L^2(\Omega)} \right)
$$

where $\lambda^M(p) = [1 + (|p| + M)^2]^{-3/2}$

4.4.2 Lower bound for error:

We denote the $\Lambda(p)$ is denoted as the maximum eigenvalue of $D^2B(p)$. For lower bound we recall the following two results from [44, 88] and assume that following inequalities holds

$$\|\mathbf{R}(u_h), v\|_{*,\omega_K} \leq \sqrt{2}\sup_{\omega_K}\Lambda(\nabla u)^{1/2} e_\omega(u_h, u) \tag{4.45}$$

and the lower bound for residual

$$\eta_K \leq \|\mathbf{R}(u_h\|_{*,2,\omega_K} + \alpha_K^{-\frac{1}{2}} h_K \|\mathbf{f} - \mathbf{f}_h\|_{L^2(K)} \tag{4.46}$$

From (4.45) and (4.46) we have the following lower bound

$$\eta_K \leq \sqrt{2}\sup_{\omega_K}\Lambda(\nabla u)^{1/2} e_\omega(u_h, u) + \alpha_K^{-\frac{1}{2}} h_K \|\mathbf{f} - \mathbf{f}_h\|_{L^2(K)} \tag{4.47}$$

Theorem 4.10: Let u be the solution of weak problem (3.9) with assumption $u \in W^{1,\infty}(\Omega)$ and u_h be the solution of discrete problem (4.1), $\mathbf{f}_h$ be the finite approximation of $\mathbf{f}$ we have

(i) conditional upper bound if

$$\|\nabla(u_h - u)\|_{0,\infty,\Omega} \leq M$$

for some fixed $M > 0$, then

$$e_\Omega(u_h, u) \leq \left(\frac{\sum_K \eta_K^2}{\inf_\Omega \lambda^M(\nabla u)}\right)^{\frac{1}{2}} + \frac{\alpha_K^{-\frac{1}{2}} h_K}{\inf_\Omega \lambda^M(\nabla u)} \left(\|\mathbf{f} - \mathbf{f}_h\|_{L^2(\Omega)}\right) \tag{4.48}$$

(ii) Lower bound. For any $K \in \mathcal{T}_h$ we have

$$\eta_K \leq \sqrt{2}\sup_{\omega_K}\Lambda(\nabla u)^{1/2} e_\omega(u_h, u) + \alpha_K^{-\frac{1}{2}} h_K \|\mathbf{f} - \mathbf{f}_h\|_{L^2(K)} \tag{4.49}$$

Remark 4.11

The "constants" in the nonlinear case are less controllable and not good as in the linear case however the numerical experiments are very satisfactory.

4.5 Numerical Experiments

All numerical experiments are performed using FreeFem++ [43]. For experimental setup we follow the same lines of [12]. We do not optimize CPU time in our computations. This computational work is divided in two categories, in first part we compute the disparity map keeping initially the weight function α as fixed constant, we compute the regularized solution u_α by performing different tests using small values of α, the second part of computation is based on mesh adaption preformed by adaptive algorithm given in next section and an arbitrary weight function α depending on residual error indicator derived in section 4.4. In this category we initially choose the large values for α and apply our adaptive algorithm. To check the performance of our method we compare our results with a table on absolute average error given in the reference [20]. To achieve this goal, a computational parameter called average absolute error is also computed here.

4.6 Adaptive Strategy

Adaptive procedure given here is different from the usual mesh refinement because the geometric domain is given as of the image and it is already well refined. We start the adaption formally coarsening the initial grid. The algorithm is based on the following steps:

(1) We start with the cartesian grid $\mathcal{T}_h^0$ corresponding to the image.

(2) **Adaptivity steps:**

- Compute $u_{\alpha_0,h}$ on $\mathcal{T}_h^0$ with $\alpha = \alpha_0$ a large constant.
- We build and adapted isotropic mesh $\mathcal{T}_h^1$ (in the sense of the finite element method, i.e with respect to the parameter h) with the metric error indicator which is well suited for the disparity $u_{\alpha_0,h}$.
- we perform the local adaptive choice of $\alpha(x)$ on $\mathcal{T}_h^1$ and obtained a new function $\alpha_1(x)$.

(3) GO to step 2 and compute $u_{\alpha_{1,h}}$ on $\mathcal{T}_h^1$.

Let us give more details on the implementation of this algorithm. On the triangulation $\mathcal{T}_{h,n}$ we compute the solution u_{h,α_n} of problem (4.1) and the corresponding error indicators (4.43). In addition to the standard information on the error distribution on the computations of $u^{\alpha_n,h}$, the error indicators act as a confidence measure by locating the regions of large errors on the gradients (edges).

Note that all the meshes $\mathcal{T}_h^n$ are obtained by mesh adaptivity such that the minimal mesh sizes are greater than 1 which is size of pixel.

The principal of the adaptive regularization process is to decrease the values of α in the regions where the error indicator is large(edges) and to increase the values in the complementary regions. However, for the stability reasons we start with a relatively high initial guess and during the adaptive process α decreases. For automatic choice of α during the adaption we use following formula for α each triangle K

$$\alpha_K^{n+1} = \mathtt{max}\left(\frac{\alpha_K^n}{1+\kappa * \left(\left(\frac{\eta_K}{\|\eta\|_\infty}\right) - 0.1\right)^+}, \alpha_{trh}\right) \tag{4.50}$$

where α_{trh} is a threshold and κ is a coefficient chosen for the control the rate of decreasing of α, $(u^+) = \mathtt{max}(u, 0)$ and $\|\eta\|_\eta = \mathtt{max}_K(\eta_K)$

4.6.1 Example:1

We start with a famous example of stereo pair Pentagon. The aerial view of Pentagon stereo pair with gray value images were downloaded from
http:/vasc.ri.cmu.edu/idb/. In the first step we check the disparity map for different constant values of smoothing α, the value of small contrast parameter β is kept fixed for all experiments as $\beta = 0.00005$. Figure 4.2 shows the plots for computed disparity maps on various fixed values of α. As the value of α is decreased, the grid is refined almost every where on the domain. We observe that the brightness of computed disparity map decreases with very small values of α, consequently, some useful informations in disparity image become disappear. In the second part of our computations we use the given adaptive algorithm, we present the results for the disparity map, error indicator

(a) Left view Pentagon (b) Time derivative f1-f2

Figure 4.1: Pentagon stereo pair and Time derivative

η_K, and mesh $\mathcal{T}_{h,n}$ on various iterations of adaptive process performed by the given adaptive algorithm. The initial value of α in this part is selected very large as $\alpha = 1000$. As the pentagon is a textured image therefore one can observe from our approximated results that the given algorithm in this case have not performed very well as compared to computations given for α as fixed on the domain. The algorithm is refining the grid uniformly in all directions of disparity image domain. Therefore we have repeated this experiment in second part of this chapter with improved version of variational model with modified data term. In this case the performance of the algorithm is improved significantly, which fulfills the requirement of our claim, specially for this image scene. **Note:** Reader should note that in this example, some of the plots for error indicator η_K are given as color images, now to identify the greater and smaller values for corresponding parameters the darker(rich) colors show the greater values and lighter colors show the smaller values for given parameters.

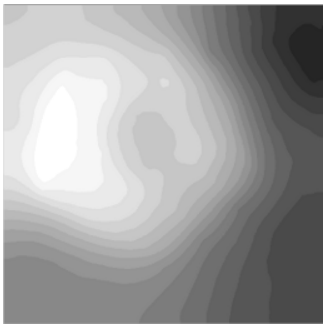

(a) Diaprity map with $\alpha = 1000$

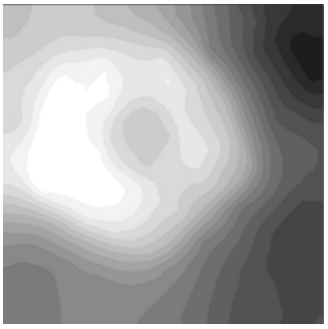

(b) Diaprity map with $\alpha = 500$

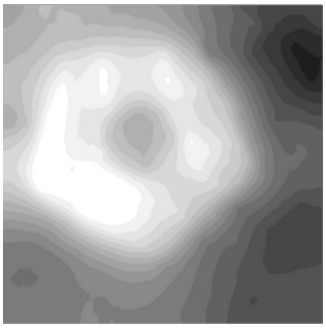

(c) Diaprity map with $\alpha = 200$

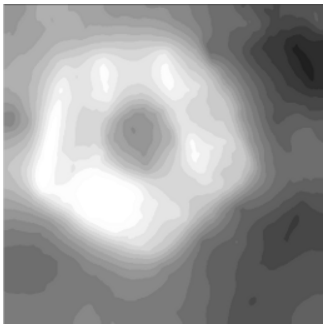

(d) Diaprity map with $\alpha = 100$

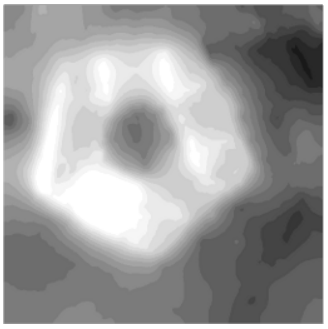

(e) Diaprity map with $\alpha = 50$

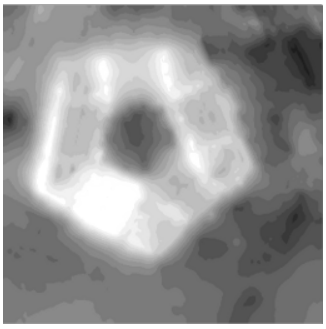

(f) Diaprity map with $\alpha = 20$

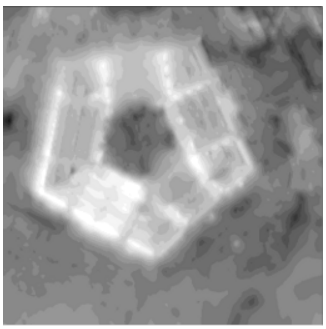

(g) Diaprity map with $\alpha = 5$

(h) Diaprity map with $\alpha = 0.9$

(i) Diaprity map with $\alpha = 0.5$

(j) Diaprity map with $\alpha = 0.1$

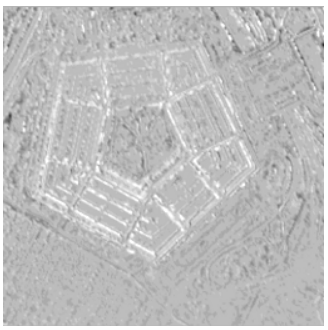

(k) Diaprity map with $\alpha = 0.01$

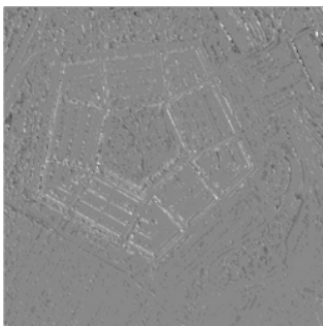

(l) Diaprity map with $\alpha = 0.001$

Figure 4.2: Example 1. Disparity map given for various values of α as fixed constant on the whole domain.

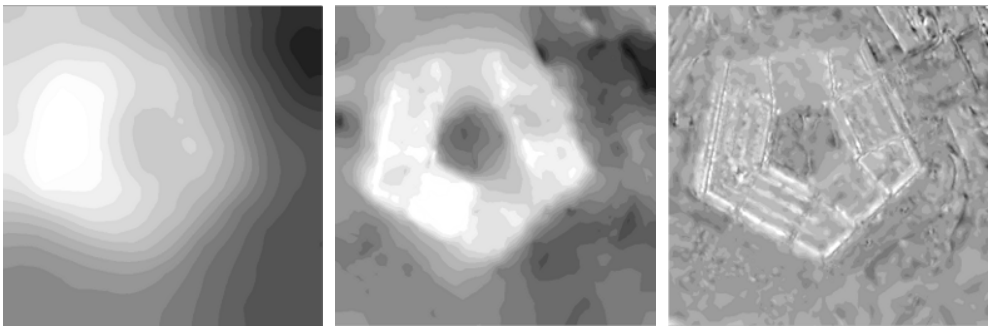

(a) Computed disparity on initial mesh

(b) Computed disparity after first iteration

(c) Computed disparity after second iteration

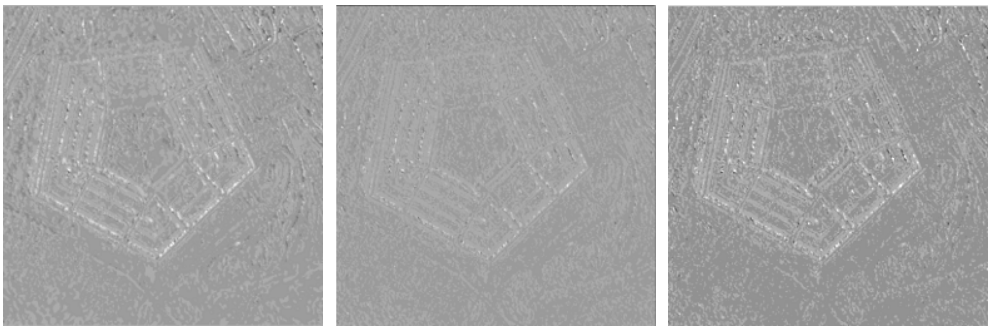

(d) Computed disparity after third t iteration iteration

(e) Computed disparity after fourth iteration

(f) Computed disparity after fifth iteration

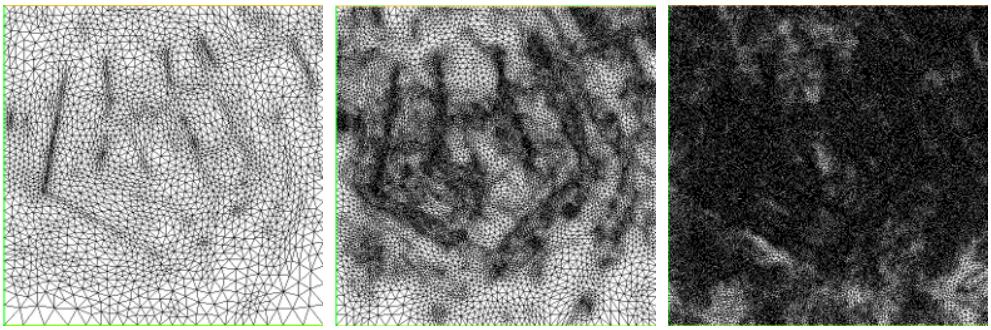

(g) Mesh after first iteration

(h) Mesh after second iteration

(i) Mesh after third iteration

Figure 4.3: Some iterations of adaptive process for disparity map computations using Pentagon stereo pair with adaptive algorithm.

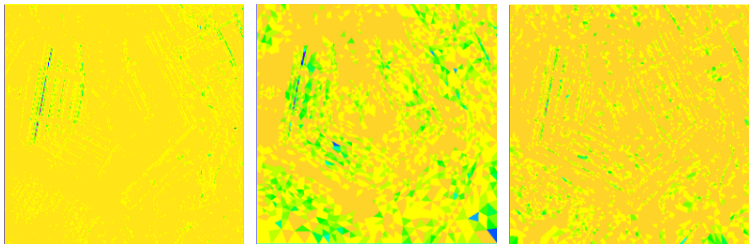

(a) Error density η_K iter0 (b) Error density η_K iter1 (c) Error density η_K iter2

Figure 4.4: Example 1. Error density on various iterations

4.6.2 Example:2

In this example we consider the grey version of stereo pair portal church available at http://cmp.felk.cvut.cz/ cechj/GCS/stereo-images/. For this stereo pair we test mesh adaption algorithm for 10 iterations. We consider initially the large value for α as $\alpha = 1000$ and test the adaptation procedure with algorithm given above, the value of small contrast parameter β is kept fixed as $\beta = 0.00005$. In this example we have observed that adaptive algorithm performs slightly better as compared to pentagon image scene, we observe that adaptation improves the solution on each next adaptive iteration and the regularization parameter α increases the number of grid points beside discontinuities like edges and keeps stable or decreases the grid points away from edges of the disparity images. We obtained the following numerical results.

(a) Left view Portal stereo pair

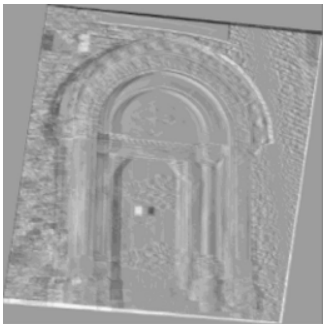

(b) Time derivative f1-f2

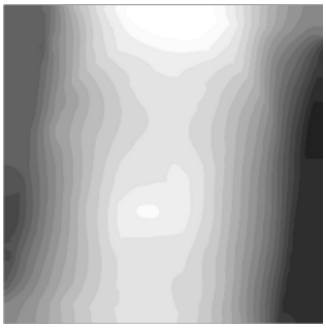

(c) Disparity iter0

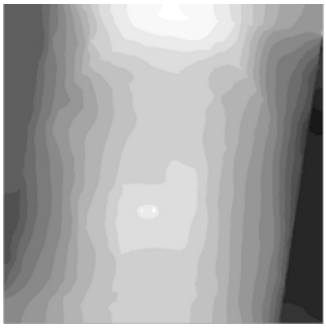

(d) Disparity iter1

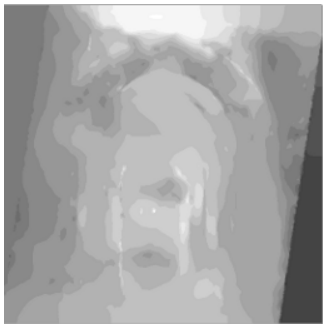

(e) Disparity iter2

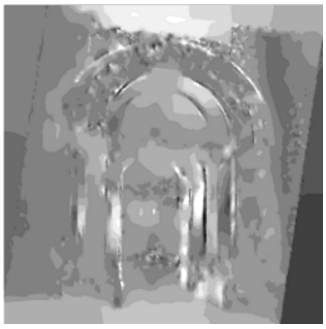

(f) Disparity iter3

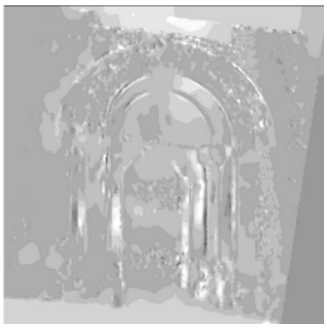

(g) Disparity iter4

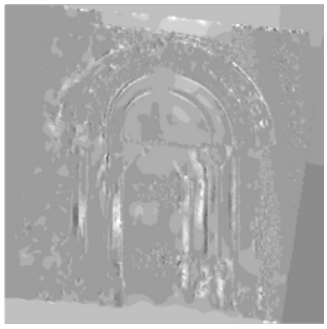

(h) Disparity iter5

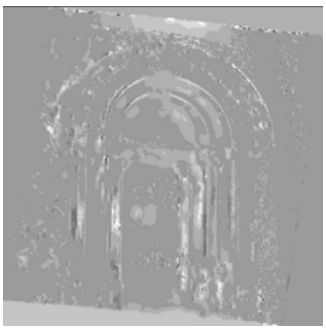

(i) Disparity iter6

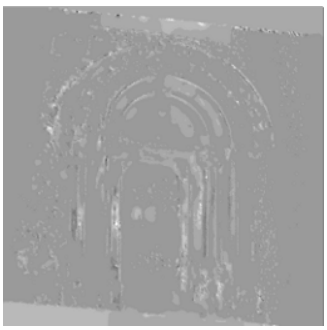

(j) Disparity iter7

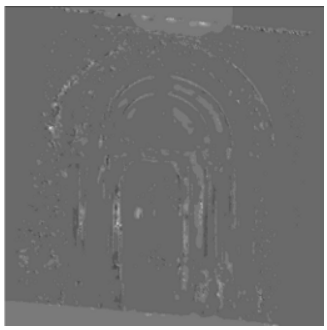

(k) Disparity iter8

Figure 4.5: Example 2, TV regularization and Portal church image scene

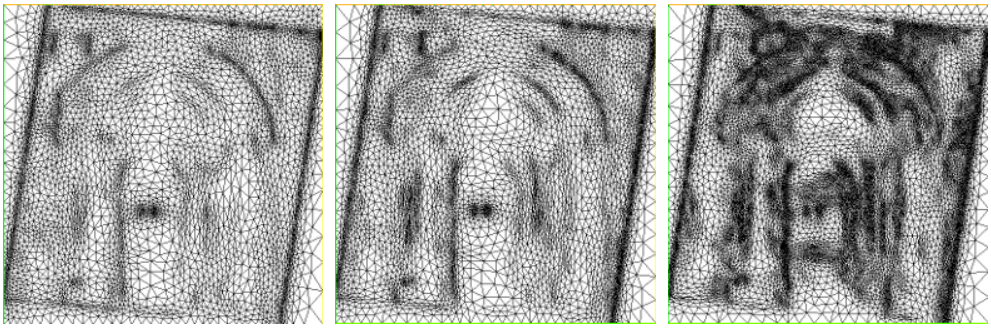

(a) Mesh iter0 (b) Mesh iter1 (c) Mesh iter2

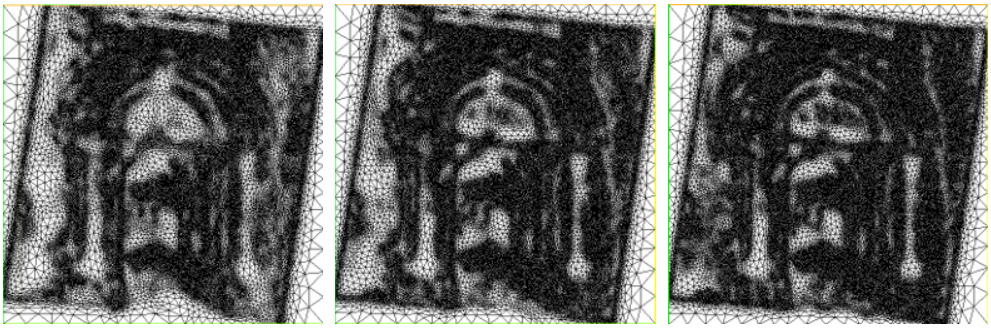

(d) Mesh iter3 (e) Mesh iter4 (f) Mesh iter5

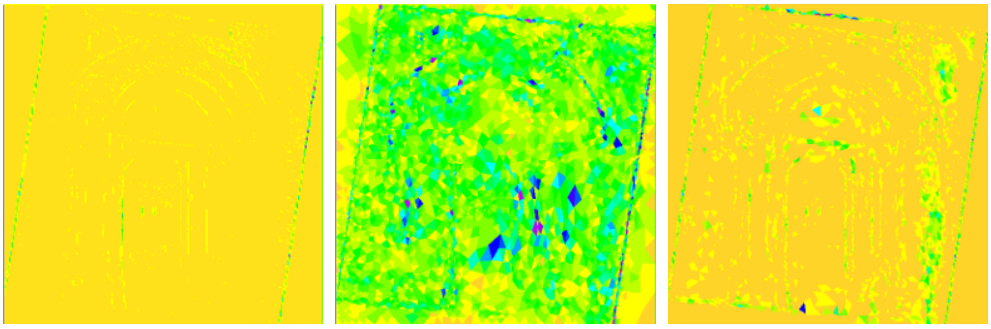

(g) Error density η_K iter0 (h) Error density η_K iter1 (i) Error density η_K iter3

Figure 4.6: Example 2, TV regularization and Portal church image scene

4.6.3 Example:3

In the example 3 we have considered the grey version of the Teddy stereo pair which is taken from the Middlebury bunch mark (http://vision.middlebury.edu/stereo/). This is a synthetic image sequence with given ground truth disparity. We perform six adaptive iterations, initializing with the large value of $\alpha = 1000$. The small parameter β is kept fixed and very small for all experiments as $\beta = 0.00005$. The reader should note that we have given some plots in the color images showing the regularization procedure by α, the color scales are not available because of some technical reasons therefore the reader is suggested that the darker colors show the smaller values of α and the lighter colors show the larger values of α.

To check the convergence performance of our method we compute the absolute average disparity error(AADE) at each adaptive iteration. Moreover to compare our results with existing methods we compare the absolute error at first iteration with a given table of the results for some existing methods given in [20].

Average absolute disparity error(AADE) We recall the following formula for AADE as

$$\text{AADE}(u, u^{gt}) = \frac{1}{|\Omega|} \sum_{i=1}^{N} \left| u_{\alpha,h,i} - u^{gt} i \right| \tag{4.51}$$

where u^{gt} is ground truth disparity , N is the number of pixels. Figures 4.8 and 4.9 shows the numerical results for computed disparity map . The following table 4.1 shows the AAD error on some adaptive iterations and the figure 4.7 shows the convergence and efficiency of the given adaptive algorithm for Teddy stereo pair. We compare the

Table 4.1: Absolute average disparity error results for five adaptive iterations

Iteration	1	2	3	4	5
AADE	0.3879	0.3844	0.3824	0.3789	0.3791

the performance of our method with the given table1 of [20]. We recall their table of results here

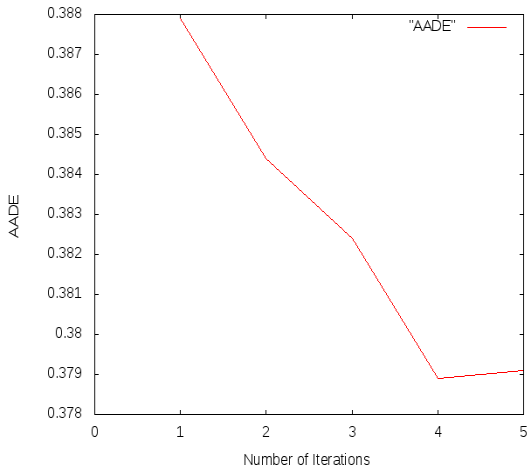

(a) Average Absolute Disparity Error

Figure 4.7: AADE on various iterations for Tedy stereo pair

Table 4.2: Comparison of average absolute error results with existing methods

Pair	GC [89]	Isotropic [81]	Anisotropic [20]	Our Method
Teddy	1.49	0.64	0.61	0.38

(a) Left view of Teddy stereo pair

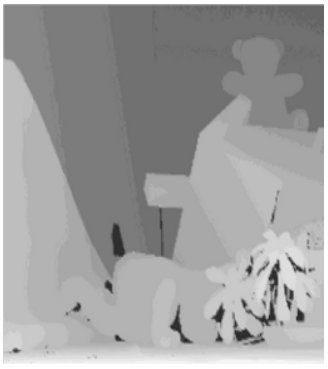

(b) Ground truth disparity

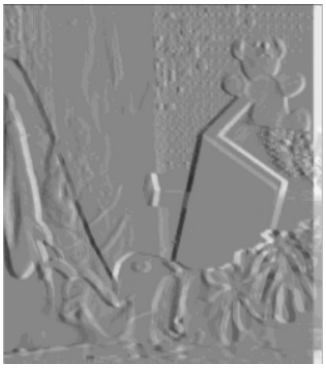

(c) Time derivative f1-f2

(d) Disparity iter0

(e) Disparity with iter1

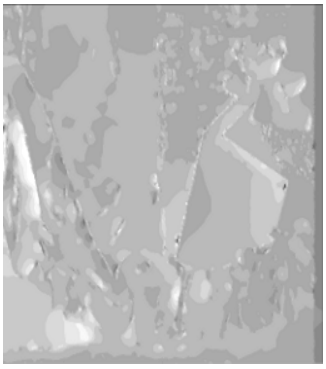

(f) Disparity with iter2

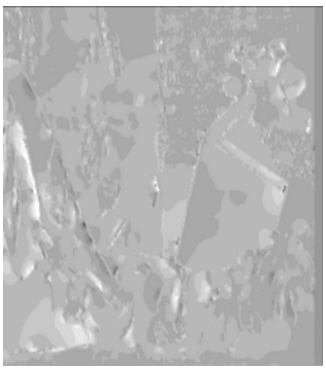

(g) Disparity with iter3

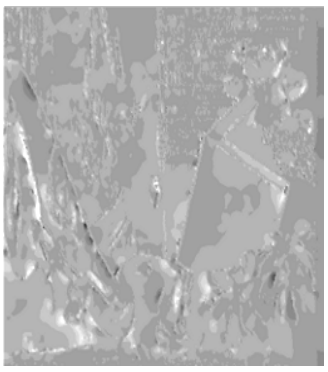

(h) Disparity with iter4

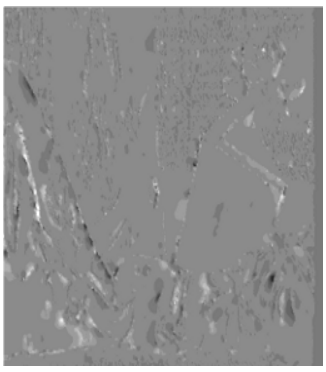

(i) Disparity with iter5

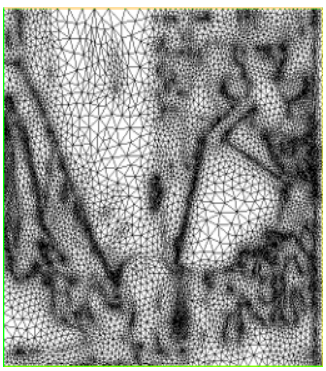

(j) Mesh iter 1

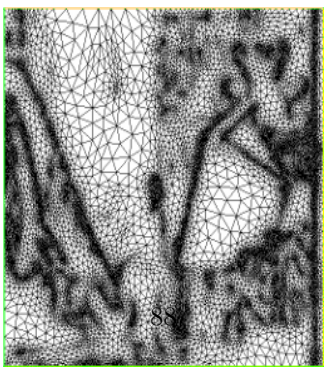

(k) Mesh iter 2

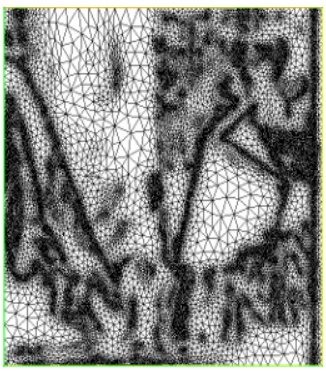

(l) Mesh iter 3

Figure 4.8: Example 3, Teddy stereo pair and TV regularization

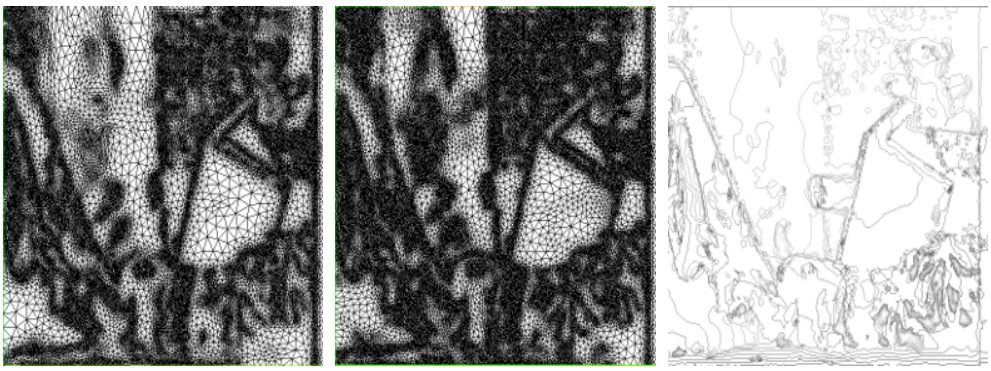

(a) Mesh iter 4 (b) Mesh iter 5 (c) Absolute Error map after iteration 3

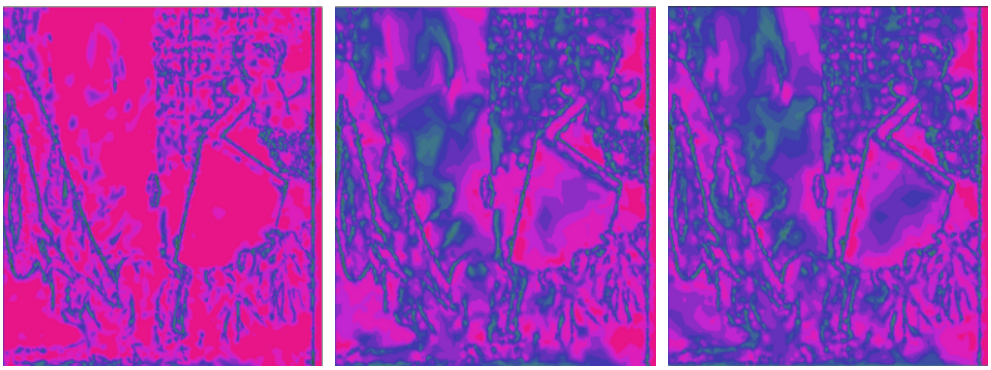

(d) $Log(\alpha)$ after iteration 0 (e) $Log(\alpha)$ after iteration 2 (f) $Log(\alpha)$ after iteration 3

Figure 4.9: Example 3, Teddy stereo pair and TV regularization

4.7 TV stereo Model with modified data term

In this part of our work we improve the TV stereo model by normalizing the data term. We consider the minimization of following improved version of energy functional to compute the horizontal depth information from a given stereo pair.

$$\mathbf{E}(u) = \int_\Omega \left(\alpha(\mathbf{x}) \sqrt{\beta^2 + |\nabla u|^2} \right) d\mathbf{x} + \int_\Omega \frac{1}{|\mathbf{grad}\, I|^2 + \zeta^2} (I_{x_1} u + I_t)^2 \Bigg) d\mathbf{x} \tag{4.52}$$

Where $I : \Omega \times \mathbb{R} \longrightarrow \mathbb{R}$, models the stereo image pair in a stereo scene, $\mathbf{x} := (x_1, x_2)^T \in \Omega$.

Euler-Lagrange Equation: It follows from calculus of variation that minimizer of of $E(u)$ satisfies the so-called Euler-Lagrange equation

$$0 = -\mathtt{div} \left(\frac{\alpha(\mathbf{x}) \nabla u}{\sqrt{\beta^2 + |\nabla u|^2}} \right) + \frac{1}{|\mathbf{grad}\, I|^2 + \zeta^2} (I_{x_1}^2 u + I_{x_1} I_t) \quad in \quad \Omega \tag{4.53}$$

where $\frac{\partial u}{\partial n} = 0$, on $\partial\Omega$ and β, ζ are a small regularization parameters, used here to avoid the division by zero in numerical computations.

4.8 Variational Formulation

A commonly used frame work to solve equation (4.53) using finite element method is variational formulation which consists in defining a bilinear form $a_\alpha(u, v; u)$ and a linear form $(\mathbf{f}, v)$ such that the equation (4.53) is associated to following weak formula. The weak formulation of (4.53) reads

Find a unction u in a Soblev space $H^1(\Omega; \mathbb{R})$ such that

$$\begin{cases} \text{Find } u \in H^1(\Omega; \mathbb{R}) \qquad \text{such that} \\ \int_\Omega \frac{\alpha(\mathbf{x}) \nabla u : \nabla v}{\sqrt{\epsilon^2 + |\nabla u|^2}} d\mathbf{x} + \int_\Omega \frac{1}{|\mathbf{grad}\, I|^2 + \zeta^2} I_{x_1}^2 u \cdot v d\mathbf{x} = \int_\Omega \frac{1}{|\mathbf{grad}\, I|^2 + \zeta^2} \mathbf{f} \cdot v d\mathbf{x} \qquad \forall v \in H^1 \end{cases} \tag{4.54}$$

4.9 Discrete Problem

The discrete problem reads

$$\begin{cases} \text{Find } \; u_h \in X_h \; \text{ such that} \\ a_{\alpha,h}(u_h, v_h; w_h) = (\mathbf{f}, v_h) \qquad \forall v_h \in X_h \end{cases} \tag{4.55}$$

where

$$a_\alpha(u_h, v_h; w_h) = \int_\Omega \alpha\, A(w_h)\nabla u_h : \nabla v_h \, d\mathbf{x} + \int_\Omega \theta\, I^2_{x_1} u_h \cdot v_h \, d\mathbf{x} \tag{4.56}$$

where the function θ is defined as

$$\theta = \frac{1}{|\mathbf{grad}\, I|^2 + \zeta^2}$$

The formula for the error indicator η_K is given as

$$\eta_K = \sum_{K\in\tau} \alpha_K^{-\frac{1}{2}}\, h_K \left\|\mathbf{f}_h - \theta\, I^2_{x_1 u_h}\right\|_{L^2(K)} + \frac{1}{2}\sum_{e\in S_h} \alpha^{-\frac{1}{2}} h_e^{\frac{1}{2}} \left\|[\alpha A(u_h)\nabla u_h \mathbf{n}_e]_e\right\|_{L^2(e)} \tag{4.57}$$

4.10 Numerical Experiments

4.10.1 Example:4

In This example we consider the famous stereo pair of the synthetic image scene corridor available at http://www.uni-bonn.de/ uzs75l/MRTStereo/. We test our algorithm for complementary stereo model (4.52). We apply 20 iterations of the mesh adaption, keeping small parameters β and ζ fixed as 0.00005. One can observe from the computed stereo disparity and given mesh on various iterations that with the improved version of stereo model we have achieved some improved results specially sharp edges as compared to the computations in previous section for simple TV stereo version. Though the edges are improved but as observed from the disparity results that the grid looks coarsening or remain stable on flat and smooth surfaces, which results in the missing of some useful informations in the flat and smooth regions, where as from our adaptive strategy a significant regularization control is obtained along nonsmooth regions like edges. Reader can observe that our computed meshes reasonably justify our claim that how the function α (as function of space) controls the adaptation procedure and improves the disparity map on each iteration of adaptation which is the main goal. Moreover one can see the experimental observations for error density η_K map computed from various iterations, that the error density decreases as the regularization procedure starts its work. The regularization process controlled by α sharpens the edges of disparity image.

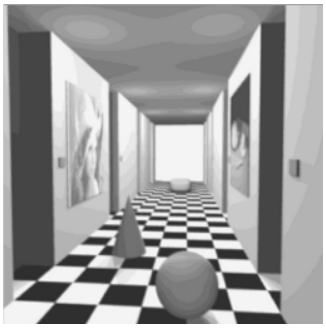

(a) Left view of corridor stereo pair

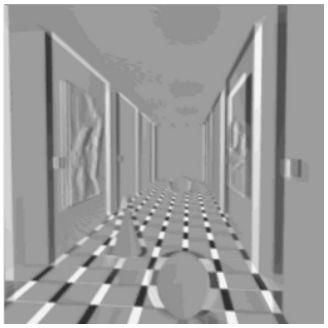

(b) Time derivative f1-f2

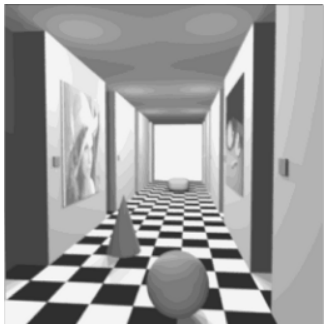

(c) Right view of corridor stereo pair

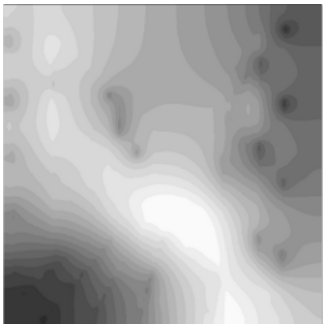

(d) Disparity iter0

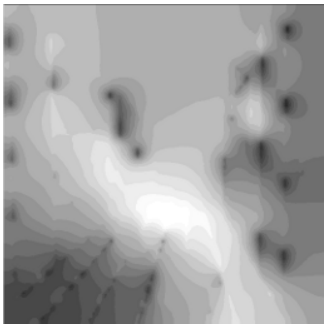

(e) Disparity iter1

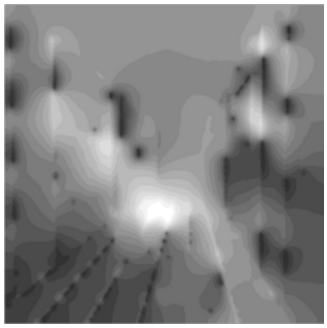

(f) Disparity iter2

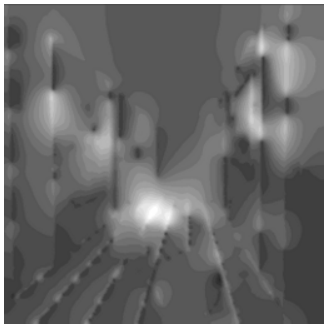

(g) Disparity iter3

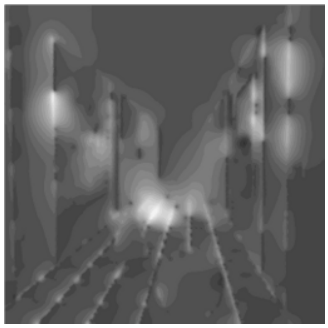

(h) Disparity iter4

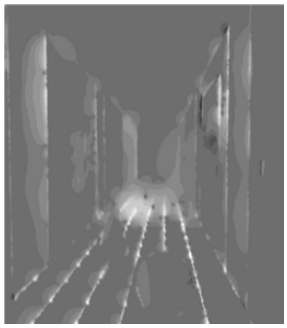

(i) Disparity iter7

Figure 4.10: Example:4 Corridor image scene and TV regularization with modified data term

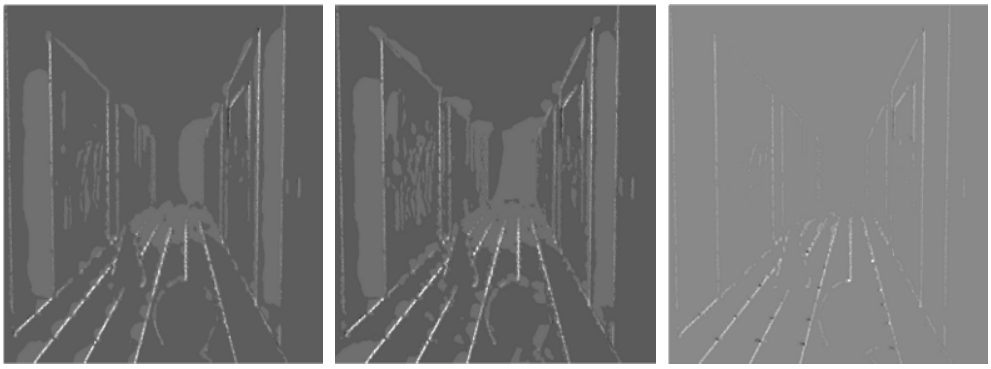

(a) Disparity iter12 (b) Disparity iter13 (c) Disparity iter19

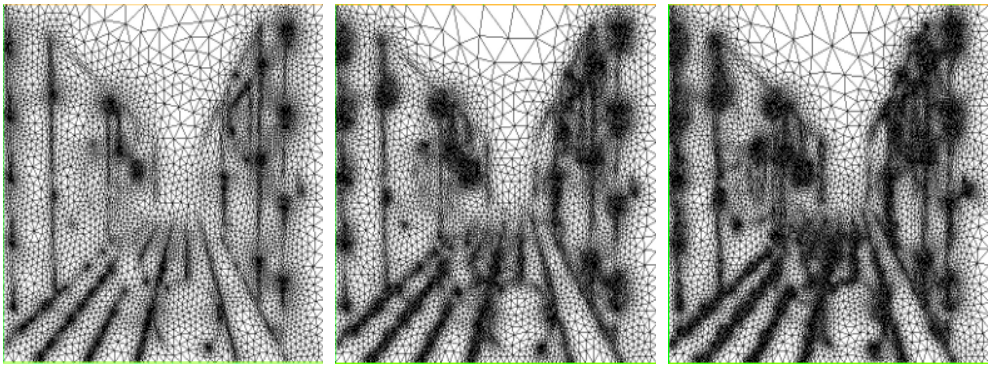

(d) Mesh iter0 (e) Mesh iter1 (f) Mesh iter2

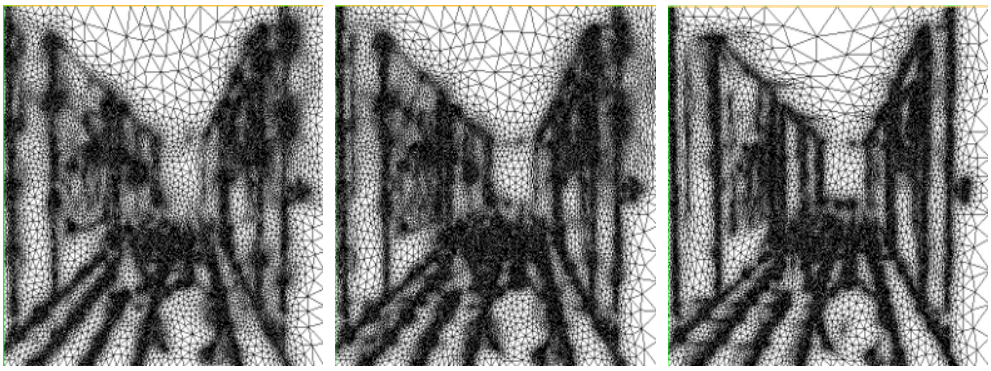

(g) Mesh iter3 (h) Mesh iter4 (i) Mesh iter7

Figure 4.11: Example:4 Corridor image scene and TV regularization with modified data term

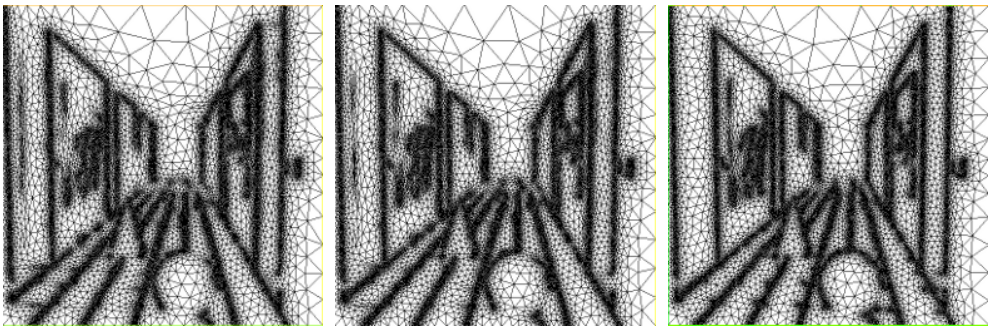

(a) Mesh iter12 (b) Mesh iter13 (c) Mesh iter19

(d) Error density η_K iter 1 (e) Error density η_K iter 13 (f) Error density η_K iter 19

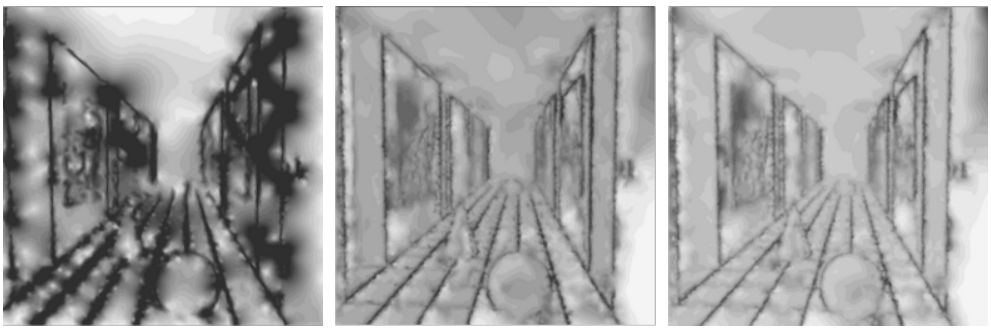

(g) $Log(\alpha)$ after iteration 0 (h) $Log(\alpha)$ after iteration 13 (i) $Log(\alpha)$ after iteration 19

Figure 4.12: Example:4 Corridor image scene and TV regularization with modified data term

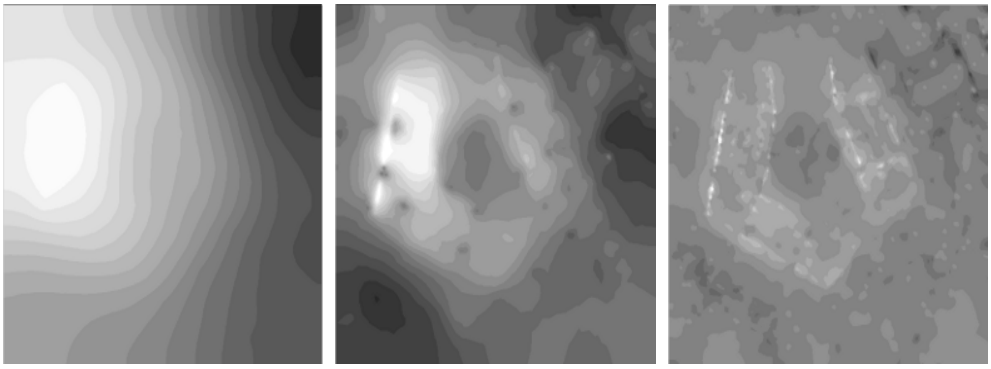

(a) Disparity iter0 (b) Disparity iter2 (c) Disparity iter4

Figure 4.13: Example: 5 Pentagon stereo pair and TV regularization with modified data term

4.10.2 Example:5

In this example we repeat the example of stereo pair Pentagon which is already given in the previous examples. The small parameters β and ζ are kept fixed for all experiments as $\beta, \zeta = 0.00005$. We test our adaptive algorithm for 20 iterations of mesh adaption. We have observed from our experiments that in the case of modification in the data term along with TV regularization, the sharp edges appear as compared to the previous experiments on pentagon image scene. The algorithm is designed in such a way that the α is allowed to increase or remain constant in the regions where error is small and decrease in the regions where the error indicator is large. As we observe from the plots showing the regularization effects by α on various adaptive iterations, that the results given in this case for α justify this above statement for the given algorithm. The results in this case are better than the previous case, the reason behind this is the normalization of data term.

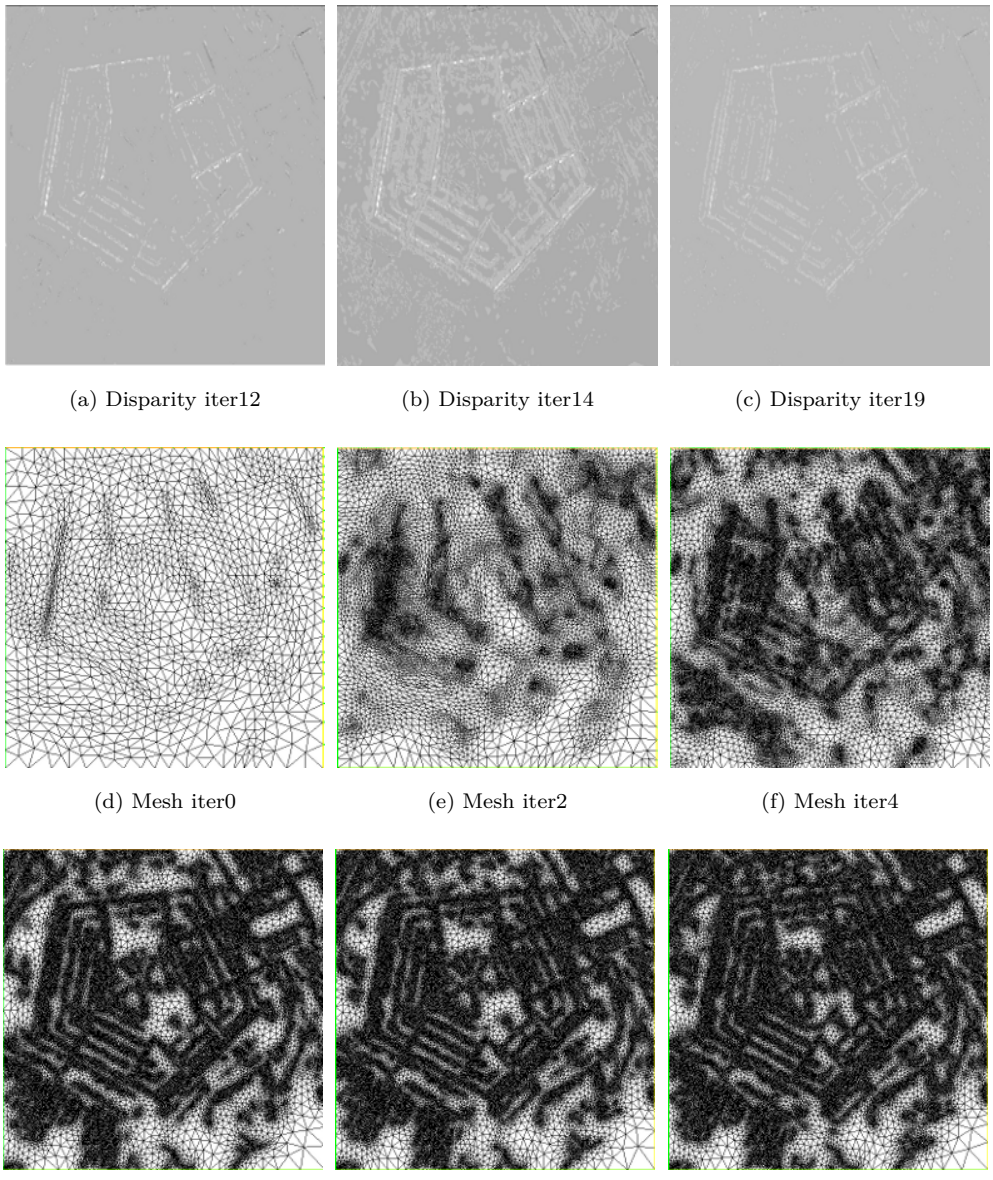

(a) Disparity iter12 (b) Disparity iter14 (c) Disparity iter19

(d) Mesh iter0 (e) Mesh iter2 (f) Mesh iter4

(g) Mesh iter12 (h) Mesh iter14 (i) Mesh iter19

Figure 4.14: Example: 5 Pentagon stereo pair and TV regularization with modified data term

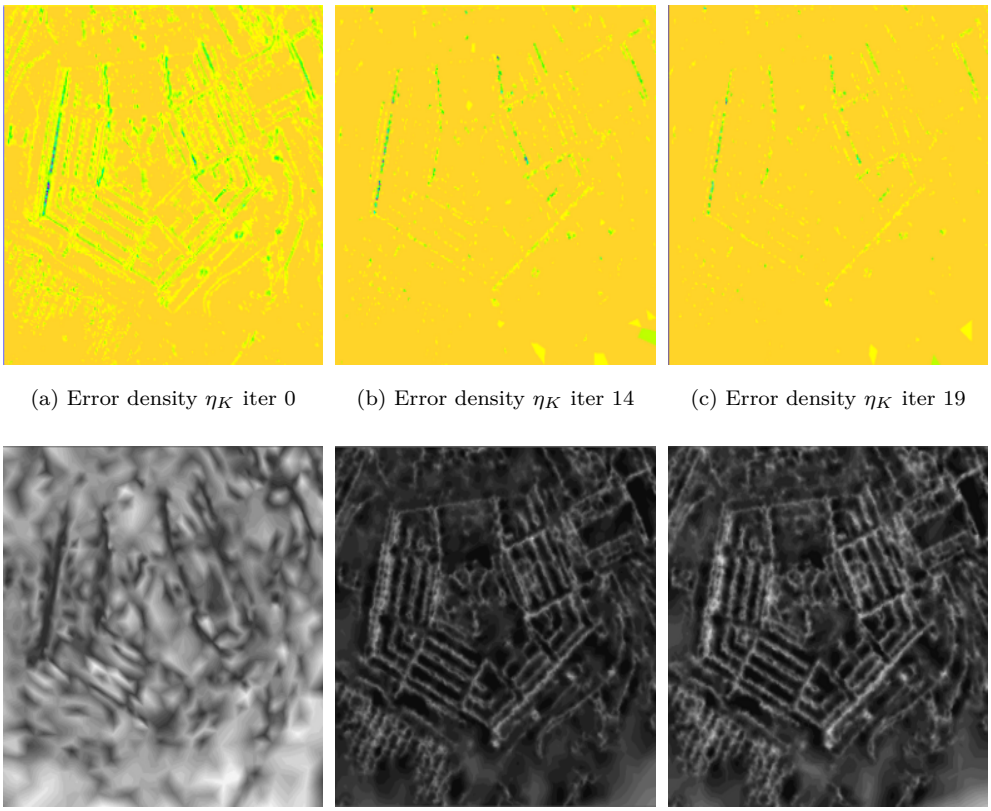

(a) Error density η_K iter 0 (b) Error density η_K iter 14 (c) Error density η_K iter 19

(d) $Log(\alpha)$ after iteration 0 (e) $Log(\alpha)$ after iteration 14 (f) $Log(\alpha)$ after iteration 19

Figure 4.15: Example: 5 Pentagon stereo pair and TV regularization with modified data term

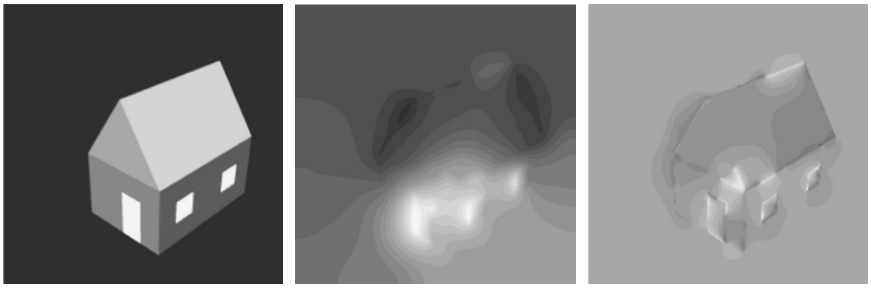

(a) Left view (b) Disparity map iter1 (c) Disparity map iter3

Figure 4.16: TV Regularization For House Stereo Pair

4.10.3 Local adaptation and TV regularization for texture-less simple stereo pairs

As we have seen from our results, that mostly the stereo pairs considered in the chapter four are textured images and the plots of the disparity map and disparity meshes are not very clear for the most of the results in the case of TV model except in the case if the data term is improved, keeping this fact in view we have considered a new stereo pair named house1 taken from the Vision and Autonomous Systems Center's Image Database http://www.ius.cs.cmu.edu/idb/. The the images are simple and texture-less. We have performed five adaptive iterations keeping the same settings as we have considered in the Pentagon stereo pair without normalizing the data term in TV stereo model. In this case our results are almost clear with improved visual quality. The color images are given for the error indicator η_k, scales are given(difficult to read) the dark colors show the greater values and lighter colors show the smaller values for η_K. The regularization effects by α are very clearly shown in grey value images(brighter regions show higher values and darker regions show the smaller values). Results are shown in the figures 4.16 and 4.17.

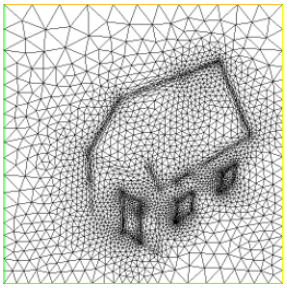

(a) Mesh after first adaption

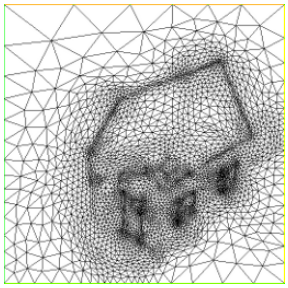

(b) Mesh after 2nd adaption

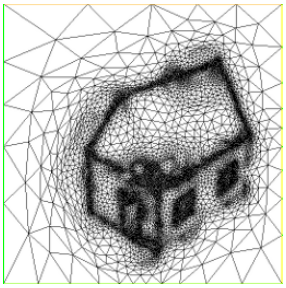

(c) Mesh after third adaption

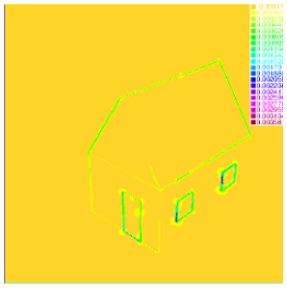

(d) η_K iter0

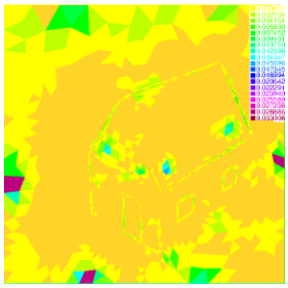

(e) η_K iter1

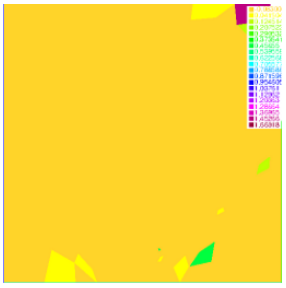

(f) η_K iter3

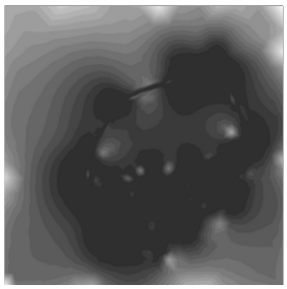

(g) $log(\alpha)$ iter0

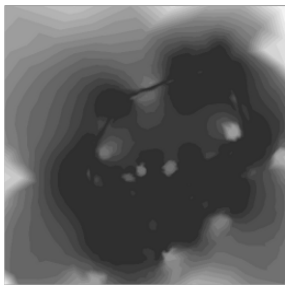

(h) $log(\alpha)$ iter1

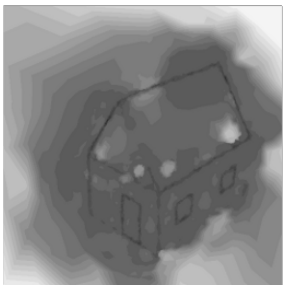

(i) $log(\alpha)$ iter3

Figure 4.17: TV Regularization For House Stereo Pair

4.10.4 Conclusion

From the overall performance of our method for the computation of stereo depth from a given stereo pair, it is observed that the efficiency of the given adaptive algorithm reduces in the case of textured and noisy image scenes. In the case of variational model with improved data term, the algorithm performs better even in the case of textured image scenes.The TV regularization with normalized data term approach yields sharp disparity as compared to the TV regularization without normalization of the data term. The local adaptive strategy by the regularization function α shows significant regularization effects on disparity domain and the adaptive process yields the sharp edges. The method discussed in this chapter performs good in the case of the simple stereo pairs, for example if we see the quality of disparity image and the given meshes in the case of house stereo pair(the last example).

Chapter 5

Extension of the method To TV Regularization Variational Models for Optic Flow Estimation

5.1 introduction

TV regularization is one of the robust approaches to compute the optic flow as well as widely used in other PDE's based image processing variational techniques [32, 19, 18, 20, 55]. In the chapter two we presented an adaptive control of regularization for a variational model with a quadratic regularizer as a smoothness term. It is observed that the quadratic regularizers do not perform very well in the neighborhood of moving the discontinuities like edges in the images. Extra smoothness property of quadratic regularizers attracts image researchers to think of a regularization approach, with which one can cope with discontinuities and regularized solution of ill-posed problems simultaneously. TV regularizer has such properties to solve these difficulties of extra smoothness along edges. This method of regularization seems to be more appropriate than the quadratic regularization approach, since it does not enforce the optical flow to be very smooth every where along the edges of moving objects and reconstructs the dense optical flow field while preserving its discontinuities.

This chapter is based on two parts, in the first part we present two different aspects of TV regularization which are established using isotropic and anisotropic approaches. We observe from our numerical results, specially for the example of taxi sequence, that in the case of TV regularization, we obtained more sharpness along edges of computed optic flow field as compared to the previous case of quadratic regularization. In the second part of this chapter we propose a nonlinear isotropic model with an improved data term. In this non-linear case we repeat the numerical experiment for mini-cooper image sequence and compare with the results obtained from isotropic case(without improved data term). We have given a short summary for each experiment and numerical observations.

From the above discussion one can say that this chapter is proposed as an adaptive control of regularization and efficient numerics for some nonlinear variational problems based on TV regularization. Our goal is to show the adaptive control and regularization effects for various nonlinear optic flow models using adaptive algorithm as given in the chapter two. The dramatic effects of the regularization on each iteration of adaption appear with remarkable improvements in producing dense flow field by reducing the

error density on each adaptive iteration which is of central interest and a novel computational setup for image researchers. The optimal choice of regularizing parameter α on an unstructured image grid is an automatic procedure of regularization which is performed by derived a posteriori error indicators.

We have already discussed in last chapters, that how to design an energy functional for the optical flow and stereo vision variational problems, moreover we have also discussed that how to construct a data term using optical flow constraint modeled from grey value constancy assumption. We consider the following energy functionals associated with the optic flow recovery by variational methods.

5.2 Isotropic case:

In the isotopic case we propose the minimization of the following energy functional to compute the optic flow.

$$E(\mathbf{u}) = \int_{\Omega} \left(\mathbf{u}^T J_{\varrho} \mathbf{u} + \alpha(\mathbf{x}) \left| \nabla \mathbf{u} \right| \right) d\mathbf{x} + \int_{\Omega} \mathbf{f} \cdot \mathbf{u} \, d\mathbf{x} \tag{5.1}$$

where α is a given, strictly positive scalar valued, continuous function on Ω. Accordingly, we consider a disjoint partition into a finite number of subdomains $\Omega_l, 1 \leq l \leq L$, such that the function α is equal to α_l on each Ω_l. The variational optic flow problem consists of: Find $\mathbf{u}$ such that

$$E\mathbf{u} = \inf E(\mathbf{v}) \tag{5.2}$$

We denote by J_{ϱ} the matrix $K_{\varrho} * (\mathbf{grad}\, f \mathbf{grad}\, f^T)$, where we use the spatial gradient $(\frac{\partial}{\partial x_1}, \frac{\partial}{\partial x_2})$

$$J_{\varrho} = \begin{pmatrix} K_{\varrho} * f_{x_1}^2 & K_{\varrho} * f_{x_1} f_{x_2} \\ K_{\varrho} * f_{x_1} f_{x_2} & K_{\varrho} * f_{x_1}^2 \end{pmatrix}.$$

and $K_{\varrho}(x, y)$ is a Gaussian kernel with standard deviation ϱ, $*$ stands for convolution. Given a vector field $\mathbf{v}$ we denote

$$\nabla \mathbf{v} = \begin{pmatrix} \frac{\partial v_1}{\partial x_1} & \frac{\partial v_1}{\partial x_2} \\ \frac{\partial v_2}{\partial x_1} & \frac{\partial v_2}{\partial x_2} \end{pmatrix}$$

We set $\mathbf{f} = (-f_{x_1} f_t, f_{x_2} f_t)^T$, and $\mathbf{u} = (u_1, u_2)^T$, where f_{x_1}, f_2 and f_t stands for the derivatives with respect to x_1, x_2 and t. For the sake of brevity we will denote by $\mathbf{u}^T J_\varrho \mathbf{u}$, $J_\varrho \mathbf{u}^2$ or $|J_\varrho^{\frac{1}{2}} \mathbf{u}|^2$ the product $(J_\varrho \mathbf{u}, \mathbf{u})$ where $(.,.)$ is the scalar product in $\mathbb{R}^2$.

The minimization problem (5.1) is solved as constraint optimization problem in the space of functions in $\mathbb{R}^2$ of bounded variations i.e. the space of functions $\mathbf{v} = (v_1, v_2)$ such that

$$\int_\Omega (|\nabla v_1| + |\nabla v_2|) d\mathbf{x} \leq +\infty$$

subject to the following optical flow constraint

$$f_t + f_{x_1} u_1 + f_{x_2} u_2 = 0 \tag{5.3}$$

Since the smoothing term is convex, we have the following result.

Theorem 5.1. Assuming that the data $\mathbf{f} \in H^1$, the minimization problem (5.1) admits the unique minimum which depends continuously on the data [53].

Using the direct results from the calculus of variation [53, 19] the minimization of energy functional (5.1) yields following Euler-Lagrange equations

$$\begin{cases} \operatorname{div}\left(\alpha(\mathbf{x}) \frac{\nabla u_1}{\sqrt{\epsilon^2 + |\nabla \mathbf{u}|^2}}\right) - \left(f_{x1}^2 u_1 + f_{x1} f_{x2} u_2 + f_{x1} f_t\right) = 0 \,\text{in}\, \Omega \\ \operatorname{div}\left(\alpha(\mathbf{x}) \frac{\nabla u_2}{\sqrt{\epsilon^2 + |\nabla \mathbf{u}|^2}}\right) - \left(f_{x1} f_{x2} u_1 + f_{x2}^2 u_2 + f_{x2} f_t\right) = 0 \,\text{in}\, \Omega \\ \frac{\partial u_1}{\partial n} = \frac{\partial u_2}{\partial n} = 0, \text{ on } \partial\Omega \end{cases} \tag{5.4}$$

where ϵ is a small parameter, which is used to avoid the division by zero during numerical experiments.

The weak formulation of (5.4) reads:

$$\begin{cases} \text{Find } \mathbf{u} \in H^1(\Omega) \text{ such that} \\ \int_\Omega \frac{\alpha(\mathbf{x}) \nabla \mathbf{u} : \nabla \mathbf{v}\, d\mathbf{x}}{\sqrt{\epsilon^2 + |\nabla \mathbf{u}|^2}} + \int_\Omega J_\varrho \mathbf{u} \cdot \mathbf{v}\, d\mathbf{x} = \int_\Omega \mathbf{f} \cdot \mathbf{v}\, d\mathbf{x}\ \forall \mathbf{v} \in H^1(\Omega) \end{cases} \tag{5.5}$$

We introduce the notations: for $\mathbf{u}, \mathbf{v} \in H^1(\Omega)$

$$a_\alpha(\mathbf{u}, \mathbf{v}; \mathbf{u}) = \int_\Omega \frac{\alpha(\mathbf{x}) \nabla \mathbf{u} : \nabla \mathbf{v}\, d\mathbf{x}}{\sqrt{\epsilon^2 + |\nabla \mathbf{u}|^2}} + \int_\Omega J_\varrho \mathbf{u} \cdot \mathbf{v}\, d\mathbf{x} \tag{5.6}$$

$$(\mathbf{f}, \mathbf{v}) = \int_\Omega \mathbf{f} \cdot \mathbf{v}\, d\mathbf{x}$$

Thus, problem (5.5) consists of finding $\mathbf{u} \in H^1(\Omega)$, such that:

$$a_\alpha(\mathbf{u}, \mathbf{v}; \mathbf{u}) = (\mathbf{f}, \mathbf{v})\ \forall \mathbf{v} \in H^1(\Omega) \tag{5.7}$$

5.2.1 Problem Discretization

Suppose that the domain Ω is polygonal and let we consider a regular family of triangulations $\mathcal{T}_h$ made up of elements which are triangles (or quadrilaterals) with maximum size $h > 0$, satisfying the usual admissibility assumptions, i.e:

Admissibility: the intersection of two different elements is either empty, a vertex, or a whole edge.

Shape regularity: The ratio of the diameter of any element $T \in \mathcal{T}_h$ to the diameter of its largest inscribed ball is bounded by a constant σ independent of T and h.

$$X_h := \left\{ \mathbf{v}_h \in C(\bar{\Omega}) | \forall K \in \mathcal{T}_h, \mathbf{v}_{h|T} \in P_1(K)^2 \right\}$$

We denote by $J_{\varrho,h}$ a finite element approximation of the matrix $J_{\varrho,h}$ obtained as follows: for any $K \in \mathcal{T}_h$ we denote by $J_{\varrho,h,K}$ the matrix where the coefficients.

$$(J_{\varrho,h,K})_{i,j} = \frac{1}{|K|} \int_K (J_{\varrho,})_{i,j} \, d\mathbf{x}, \; 1 \leq i,j \leq 2$$

are the mean values of the coefficients of J_ϱ on K. The matrix $J_{\varrho,h}$ is the piecewise constant matrix which take the value $J_{\varrho,h,K}$ on the element K.

The discrete problem reads

$$\begin{cases} \text{Find } \mathbf{u}_{\alpha,h} \in X_h \text{ such that} \\ a_{\alpha,h}(\mathbf{u}_h, \mathbf{v}_h; \mathbf{u}_h) = (\mathbf{f}, \mathbf{v}_h) \qquad \forall \mathbf{v}_h \in X_h \end{cases} \tag{5.8}$$

Where

$$a_{\alpha,h}(\mathbf{u}_h, \mathbf{v}_h; \mathbf{u}_h) = \int_\Omega \frac{\alpha(\mathbf{x}) \nabla \mathbf{u}_h : \nabla \mathbf{v}_h \, d\mathbf{x}}{\sqrt{\epsilon^2 + |\nabla \mathbf{u}_h|^2}} + \int_\Omega J_{\varrho,h} \mathbf{u}_h \cdot \mathbf{v}_h \, d\mathbf{x}$$

and

$$(\mathbf{f}, \mathbf{v}_h) = \int_\Omega \mathbf{f} \cdot \mathbf{v}_h \, d\mathbf{x}$$

5.3 Anisotropic case:

We propose the following anisotropic energy model for the determination of optic flow.

$$E(\mathbf{u}) = \int_\Omega \left(\mathbf{u}^T J_\varrho \mathbf{u} + \alpha_1(\mathbf{x}) \left| \nabla u_1 \right| + \alpha_2(\mathbf{x}) \left| \nabla u_2 \right| \right) d\mathbf{x} + \int_\Omega \mathbf{f} \cdot \mathbf{u} \, d\mathbf{x} \tag{5.9}$$

where α_1 and α_2 are given strictly positive, scalar valued, continuous functions on Ω. Since the smoothing term is convex, we have the following result.

Theorem 5.2. Assuming that the data $\mathbf{f} \in H^1$, the minimization problem (5.9) admits the unique minimum which depends continuously on the data [53].

Using the direct results from the calculus of variation [53, 19] the minimization of energy functional (5.9) yields following Euler-Lagrange equations.

$$\begin{cases} \operatorname{div}\left(\alpha_1(\mathbf{x})\,\frac{\nabla u_1}{\sqrt{\epsilon^2+|\nabla u_1|^2}}\right) - \left(f_{x1}^2 u_1 + f_{x1}f_{x2}u_2 + f_{x1}f_t\right) = 0 \,\text{in}\,\Omega \\ \operatorname{div}\left(\alpha_2(\mathbf{x})\,\frac{\nabla u_2}{\sqrt{\epsilon^2+|\nabla u_2|^2}}\right) - \left(f_{x1}f_{x2}u_1 + f_{x2}^2 u_2 + f_{x2}f_t\right) = 0 \,\text{in}\,\Omega \\ \frac{\partial u_1}{\partial n} = \frac{\partial u_2}{\partial n} = 0, \text{ on } \partial\Omega \end{cases} \tag{5.10}$$

where ϵ is a small parameter used to avoid the division by zero during numerical experiments.

Weak formulation of (5.10) reads:

$$\begin{cases} \text{Find } \mathbf{u} \in H^1(\Omega) \text{ such that} \\ \int_\Omega \begin{pmatrix} \frac{\alpha_1(\mathbf{x})}{\sqrt{\epsilon^2+|\nabla u_1|^2}} & 0 \\ 0 & \frac{\alpha_2(\mathbf{x})}{\sqrt{\epsilon^2+|\nabla u_2|^2}} \end{pmatrix} \nabla\mathbf{u} : \nabla\mathbf{v}\, d\mathbf{x} + \int_\Omega J_\varrho \mathbf{u}\cdot\mathbf{v}\, d\mathbf{x} = \int_\Omega \mathbf{f}\cdot\mathbf{v}\, d\mathbf{x}\ \forall \mathbf{v} \in H^1(\Omega) \end{cases} \tag{5.11}$$

The discrete problem reads

$$\begin{cases} \text{Find } \mathbf{u}_{\alpha,h} \in X_h \text{ such that} \\ a_{\alpha,h}(\mathbf{u}_h, \mathbf{v}_h; \mathbf{u}_h) = (\mathbf{f}, \mathbf{v}_h) \qquad \forall \mathbf{v}_h \in X_h \end{cases} \tag{5.12}$$

where

$$a_{\alpha,h}(\mathbf{u}_h, \mathbf{v}_h; \mathbf{u}_h) = \int_\Omega \begin{pmatrix} \frac{\alpha_1(\mathbf{x})}{\sqrt{\epsilon^2+|\nabla u_{1h}|^2}} & 0 \\ 0 & \frac{\alpha_2(\mathbf{x})}{\sqrt{\epsilon^2+|\nabla u_{2h}|^2}} \end{pmatrix} \nabla\mathbf{u}_h : \nabla\mathbf{v}_h\, d\mathbf{x} + \int_\Omega J_{\varrho,h}\mathbf{u}_h\cdot\mathbf{v}_h\, d\mathbf{x}$$

and

$$(\mathbf{f}, \mathbf{v}_h) = \int_\Omega \mathbf{f}\cdot\mathbf{v}_h\, d\mathbf{x}$$

5.4 Residual error indicator:

We propose the following a posteriori residual error indicator as given in [12, 44, 88], which is an upper bound for error in $L^2(\Omega)$ norm as shown in [12]. For each element

$K \in \mathcal{T}_h$ the the residual error indicator η_K in L^2 norm is given as.

(1.) **Isotrpic case:**

$$\eta_K = \alpha_K^{-1/2} h_K \left\| \mathbf{f}_h - J_{\varrho,h}\mathbf{u}_h \right\|_{L^2(K)^2} + \frac{1}{2}\sum_{e\in S_h} \alpha_e^{-\frac{1}{2}} h_e^{\frac{1}{2}} \left\| [\frac{\alpha \nabla \mathbf{u}_h \cdot \mathbf{n}_e}{\sqrt{\epsilon^2 + |\nabla \mathbf{u}_h|^2}}]_e \right\|_{L^2(e)^2} \tag{5.13}$$

(2.) **Anisotropic case case:**

$$\begin{aligned}\eta_K = \alpha_K^{-1/2} h_K \left\| \mathbf{f}_h - J_{\varrho,h}\mathbf{u}_h \right\|_{L^2(K)^2} &+ \frac{1}{2}\sum_{e\in S_h} \alpha_e^{-\frac{1}{2}} h_e^{\frac{1}{2}} \left\| [\frac{\alpha_1 \nabla u_{1h} \cdot \mathbf{n}_e}{\sqrt{\epsilon^2 + |\nabla u_{1h}|^2}}]_e \right\|_{L^2(e)} \\ &+ \frac{1}{2}\sum_{e\in S_h} \alpha_e^{-\frac{1}{2}} h_e^{\frac{1}{2}} \left\| [\frac{\alpha_2 \nabla u_{2h} \cdot \mathbf{n}_e}{\sqrt{\epsilon^2 + |\nabla u_{2h}|^2}}]_e \right\|_{L^2(e)}\end{aligned} \tag{5.14}$$

Where h_K is the diameter of $K \in \mathcal{T}_h$ and h_e is denoted as size of edge $e \in S_h$(set of edges in $\mathcal{T}_h$). $\mathbf{n}_e$ is denoted as unit vector normal to the edge e. $[\cdot]$ denotes the jump over the edge between two elements.

5.5 Adaptive control and numerical experiments

The procedure for adaptation control is same as given in the chapter two for linear model. We perform our numerical experiments using FreeFem++, for details of mesh adaption and computational procedure we refer the reader to review the manual [43]. We use following algorithm to control our adaptation procedure and achieve our goal.

- Compute $\mathbf{u}_{\alpha_0,h}$ on $\mathcal{T}_h^0$ with $\alpha = \alpha_0$ a large constant.
- We build and adapted isotropic mesh $\mathcal{T}_h^1$ (in the sense of the finite element method, i.e with respect to the parameter h) with the metric error indicator which is well suited for the disparity $\mathbf{u}_{\alpha_0,h}$.
- we perform the local adaptive choice of $\alpha(\mathbf{x})$ on $\mathcal{T}_h^1$ and obtained a new function $\alpha_1(\mathbf{x})$.

(3) GO to step 2 and compute $\mathbf{u}_{\alpha_{1,h}}$ on $\mathcal{T}_h^1$.

For automatic choice of α during the adaption we use following formula for each triangle K

$$\alpha_K^{n+1} = \mathtt{max}\left(\frac{\alpha_K^n}{1+\kappa * \left(\left(\frac{\eta_K}{\|\eta\|_\infty}\right) - 0.1\right)^+}, \alpha_{trh}\right) \tag{5.15}$$

where α_{trh} is a threshold and κ is a coefficient chosen for the control the rate of decreasing of α, $(u^+) = \mathtt{max}(\mathbf{u}, 0)$ and $\|\eta\|_\infty = \mathtt{max}_K(\eta_K)$.
Using above model (5.1) we apply our method method to perform experiments on two real world sequences. Results are given in following two examples.

5.5.1 Example:1

In this example we consider the taxi sequence and perform seven iterations of adaption. Initially we consider $\alpha = 1000$ and the parameter ϵ is kept very small throughout all the examples. With TV regularization model we observed that the improved dense flow field with preserved discontinuities is obtained. This example is specially repeated to compare the efficiency of two different models, one with quadratic regularization approach(chapter two) and other using TV regularization approach (the chapters four and five). One can observe from the various numerical experiments that the requirement of our claim for the given adaptive algorithm is justified. Though our method works reasonably and justify our claim for both the cases as linear and nonlinear models but due to the strong discontinuity preserving properties of TV regularization the flow field is obtained improved with sharp edges as compared to the quadratic regularization(chapter two). Our experiments show that how the α automatically refine and coarse the grid in the various regions of flow filed, moreover the error density reduces at each iteration of adaptation, by allowing the improvement in the dense flow field, the reader should note here that some numerical results are given in the color images(for example in the case of η_k or α) where as the color scales are not shown this is because of some technical reasons therefore we suggest the readers that these given color images take the greater values in the regions with darker color and smaller values in the regions with lighter color(this statement is valid in general for all the given color images in this thesis).

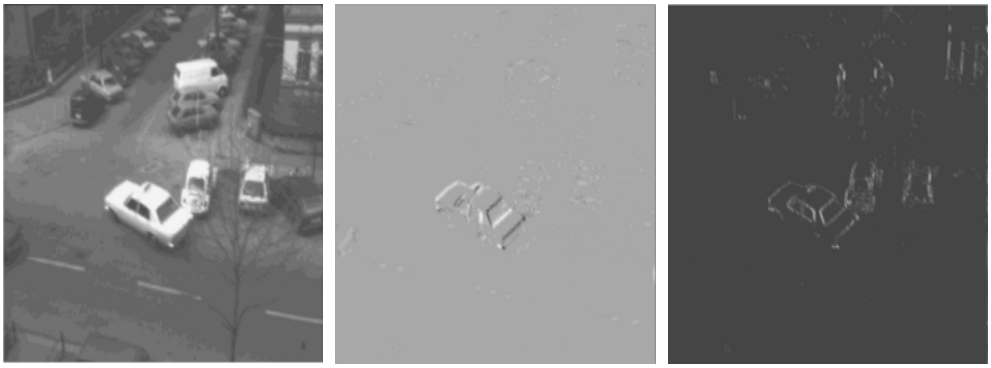

(a) Taxi sequence first frame (b) Time derivative f1-f2 (c) Structure tensor J_ϱ

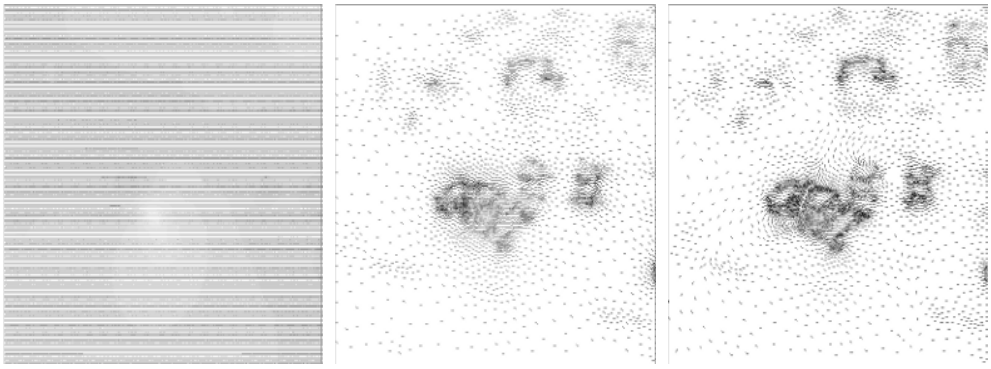

(d) Flow vector iter0 (e) Flow vector iter1 (f) Flow vector iter2

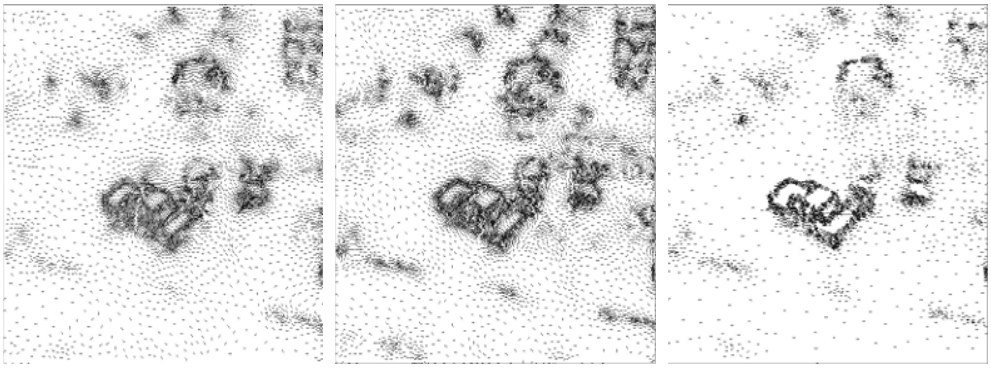

(g) Flow vector iter3 (h) Flow vector iter4 (i) Flow vector iter5

Figure 5.1: Taxi sequence example with TV regularization and isotropic case.

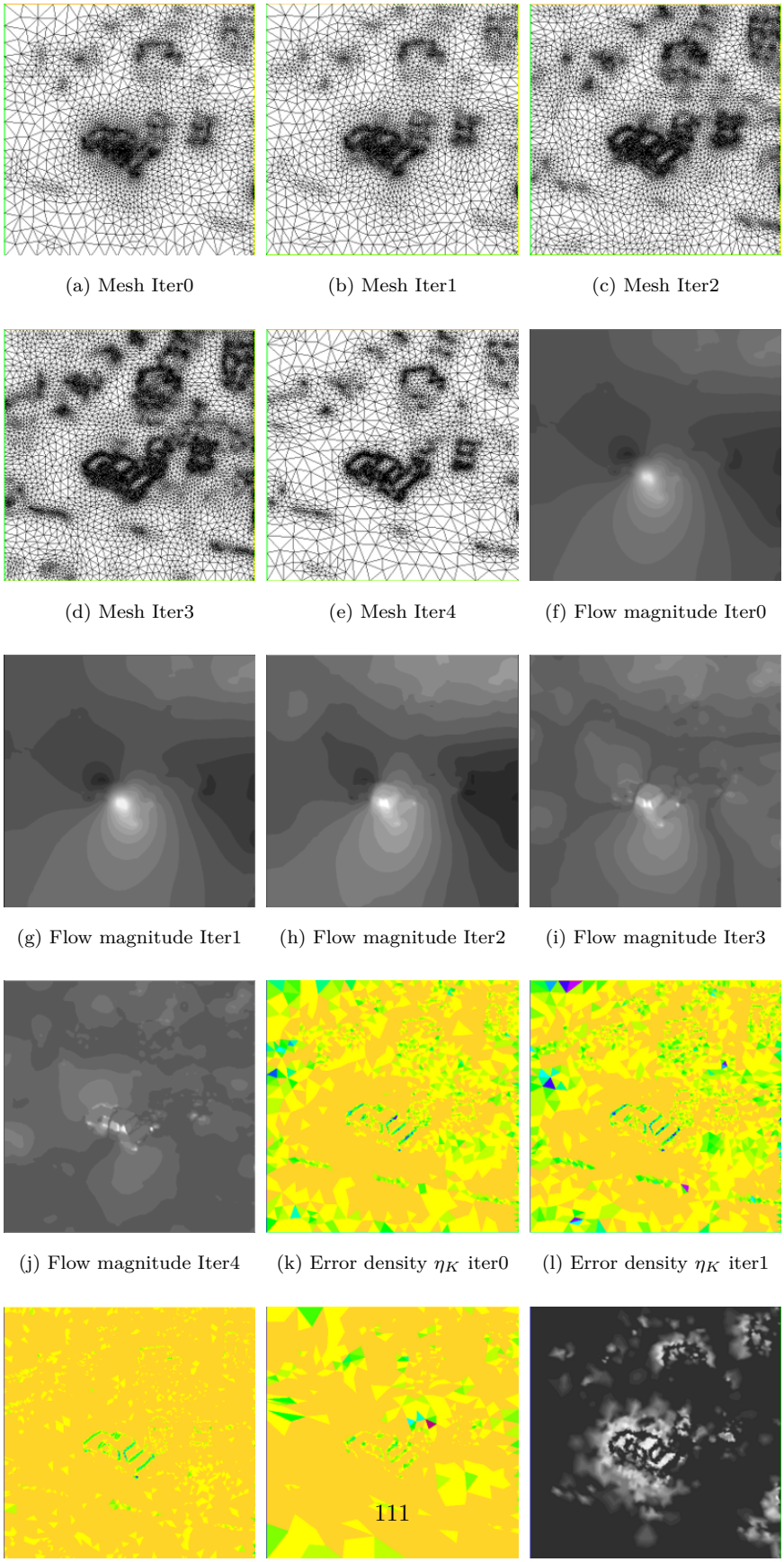

(a) Mesh Iter0 (b) Mesh Iter1 (c) Mesh Iter2

(d) Mesh Iter3 (e) Mesh Iter4 (f) Flow magnitude Iter0

(g) Flow magnitude Iter1 (h) Flow magnitude Iter2 (i) Flow magnitude Iter3

(j) Flow magnitude Iter4 (k) Error density η_K iter0 (l) Error density η_K iter1

(m) Error density η_K iter3 (n) Error density η_K iter4 (o) α iter0

Figure 5.2: Taxi sequence example with TV regularization and isotropic case.

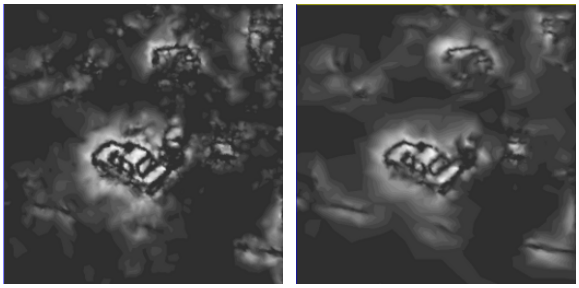

(a) α iter2 (b) α iter5

Figure 5.3: Taxi sequence example with TV regularization and isotropic case.

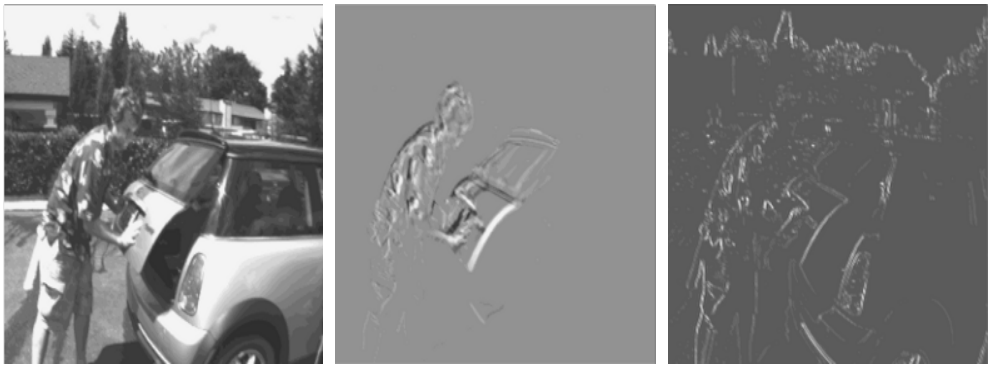

(a) Mini cooper sequence 8th frame (b) Time derivative f1-f2 (c) Structure tensor J_ϱ

Figure 5.4: Mini cooper image sequence and TV regularization with isotropic case.

5.5.2 Example: 2

In this example we test our algorithm with TV regularization for the mini cooper image sequence available at $http://vision.middlebury.edu/flow/data/$. We select the large initial value of α as $= 1000$. We preform four iteration of mesh adaptation. The dramatic improvement in optic flow field is observed at each iteration of adaption with sharp edges. The α controls the adaptive procedure with automatic decrease in the regions where the error density is large and it remains stable or increase in the smooth or flat regions of the flow field. The given meshes for the various iterations are given to show the adaptive procedure, moreover the results for residual error indicator are given for some iterations to show the control of the error density at each next iteration. The numerical results are given below.

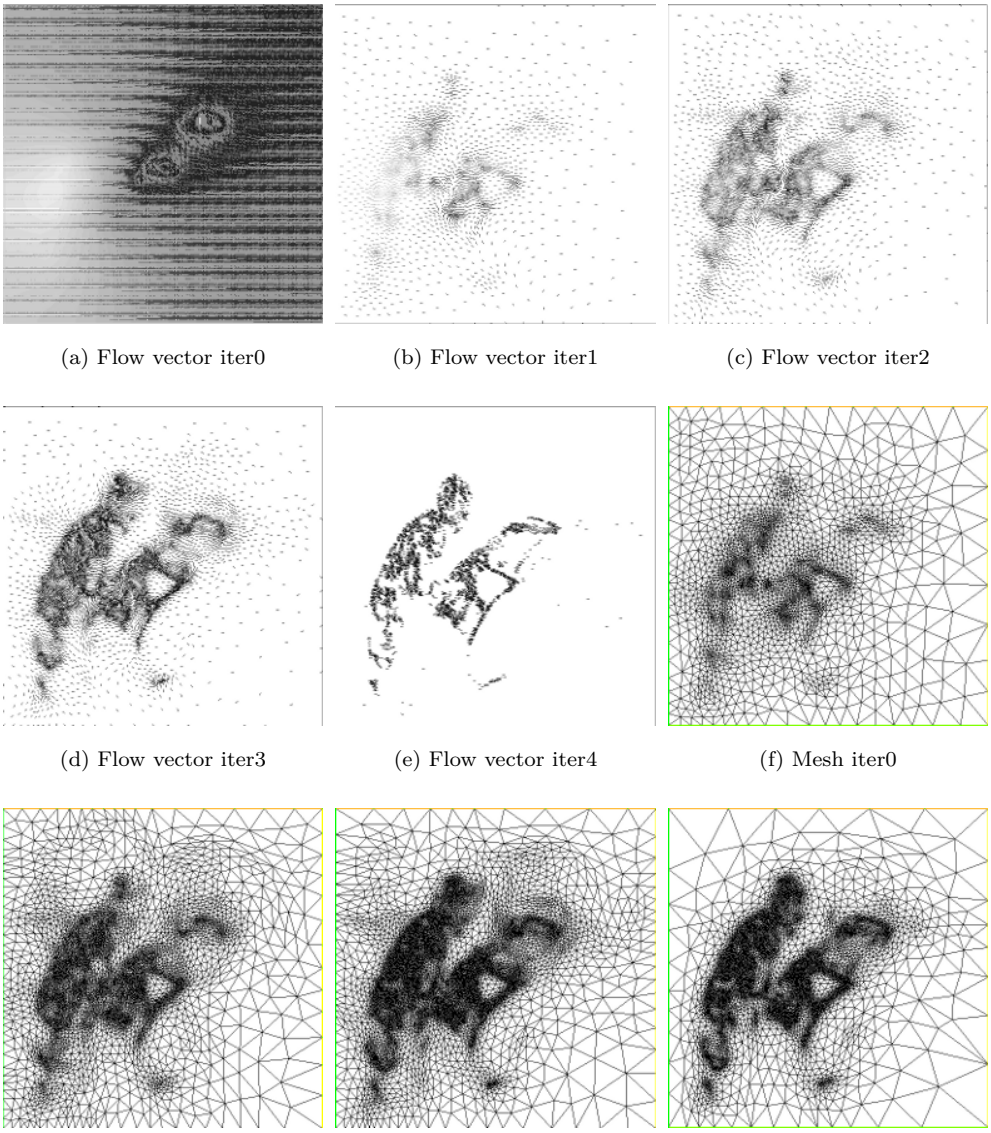

(a) Flow vector iter0 (b) Flow vector iter1 (c) Flow vector iter2

(d) Flow vector iter3 (e) Flow vector iter4 (f) Mesh iter0

(g) Mesh iter1 (h) Mesh iter2 (i) Mesh iter4

Figure 5.5: Mini cooper image sequence and TV regularization with isotropic case.

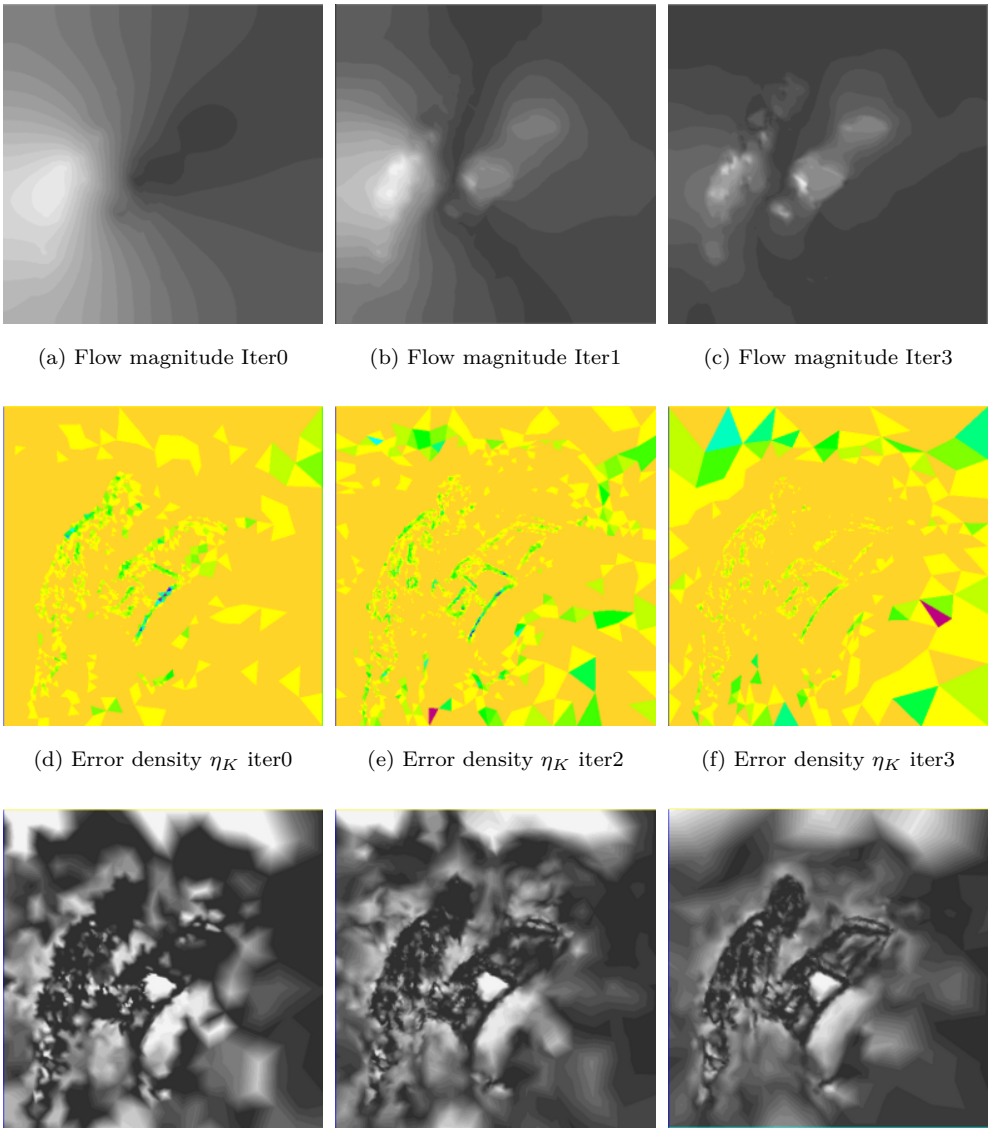

(a) Flow magnitude Iter0 (b) Flow magnitude Iter1 (c) Flow magnitude Iter3

(d) Error density η_K iter0 (e) Error density η_K iter2 (f) Error density η_K iter3

(g) α iter0 (h) α iter1 (i) α iter3

Figure 5.6: Mini cooper image sequence and TV regularization with isotropic case.

5.5.3 Convergence by angular error and comparison with existing methods

In the isotropic case we have tested an very famous grey value synthetic image sequence with given ground truth velocity components available at the Institute of bio and geosciences(IBG) (http://www2.fz-juelich.de) and
Middlebury bunch mark(http://vision.middlebury.edu/flow/data/).

Average angular Error(AAE)

To evaluate the performance of our method for optic flow(two dimensional disparity map) we recall the average angular formula

$$AAE = arccos\left(\frac{u_c u_e + v_c v_e + 1}{\sqrt{(u_c^2 + v_c^2 + 1)(u_e^2 + v_e^2 + 1)}}\right) \tag{5.16}$$

where (u_c, v_c) is denoted as computed flow and (u_e, v_e) is denoted as exact flow(Ground truth). We evaluate the performance of our novel computational approach using isotropic variational model for the famous Yosemite image sequence without clouds given with ground truth flow field which is already analyzed by some image motion practitioners, we refer the reader to see the evaluation tables for average angular error in [19].

Initially we select the value of $\alpha = 1000$, the value of $\beta = 0.005$ is kept very small for all our experiments for TV regularization. From the table 5.1, we observe that AAE decreases on each adaptive iteration with improvement in obtaining the dense flow field, on the first iteration $AAE = 4.630$ and on the 9th iteration $AAE = 4.42^0$, if we compare our result with 2-DCLG nonlinear table.2 of [19](for $\alpha = 1000$ $AAE = 4.57^0$) which is slightly less than the error of our method on first iteration but greater as compared to the angular error at converged solution, if we compare our results with 2-DCLG nonlinear table.3 of [19](for $\alpha = 1000$ $AAE = 8.37^0$), in this case our method outer performs as compared to their method, though their AAE evaluation is based on sensitivity of various parameters other than α, moreover from the visual quality point of view one can observe from figure 5.7 the 100% dense flow field is obtained after 9th adaptive iteration with better visual quality as compared to the flow field plots for

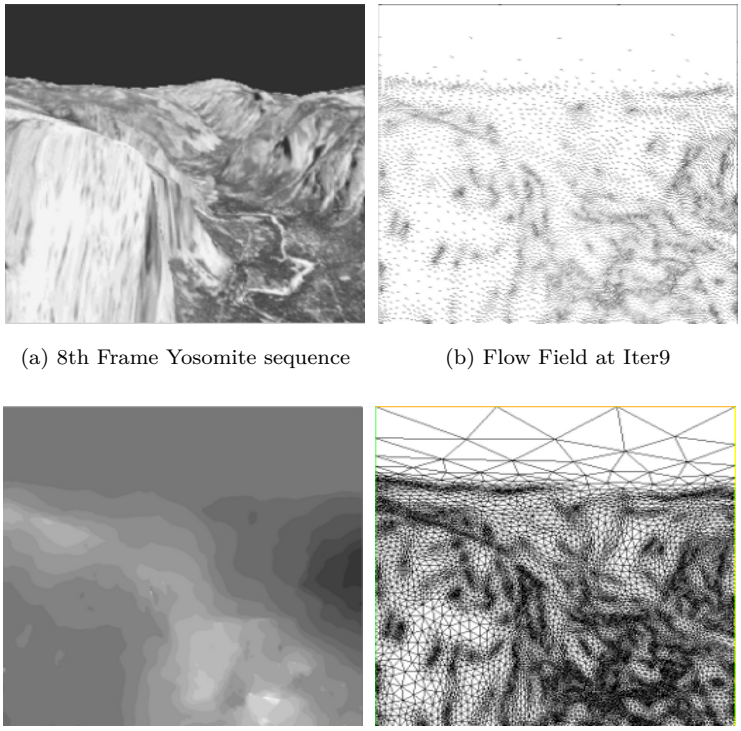

(a) 8th Frame Yosomite sequence (b) Flow Field at Iter9

(c) Magnitude Iter9 (d) Mesh Iter9

Figure 5.7: Computed optic flow field for Yosemite image sequence(Isotropic TV model) at 9th adaptive iteration

Yosemite sequence without clouds are given in [19]. The results are given in figure5.7

Table 5.1: Average Angular Error at various adaptive iterations

Iter	1	2	4	8	9
AAE	4.63^0	4.61^0	4.51^0	4.50^0	4.42^0

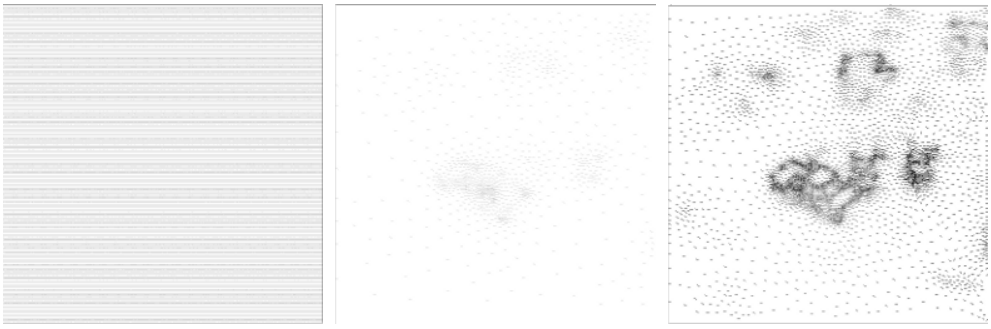

(a) Flow vector iter0 (b) Flow vector iter1 (c) Flow vector iter4

Figure 5.8: Taxi sequence with TV regularization and anisotropic case.

5.5.4 Numerical Results for anisotropic case

Example 3:

In this example we again consider the taxi image sequence to check the performance of the anisotropic model (5.9). Initially we consider $\alpha_1 = 2000$ and $\alpha_2 = 500$. We observed some improvement in sharpness of flow field as compared with isotropic case using TV regularization. The sharp results observed with enhanced edges. One can also compare these results with the computed results using optic flow model given in chapter two (quadratic regularization), a significant improvement is achieved in estimation of dense flow field with sharp edges. The adaptive procedure is improved as compared to the previous isotropic case.The increase in the number of adaptive iterations(adaptive time of algorithm) improved the regularization effects by α_1 and α_2 in different directions separately (anisotropic property), which enhanced the performance of the regularization algorithm and the robustness in the adaptive control of regularization. In the anisotropic case, the α_1 is given in the form of color images where the darker color takes smaller values and lighter color takes larger values. Reader should note that at this stage we are not interested in optimization of convergence time, but our goal is to obtained a better adaptive control of regularization for the existing models. In this experiment we perform 8 iterations of adaptation, the results are given with captions.

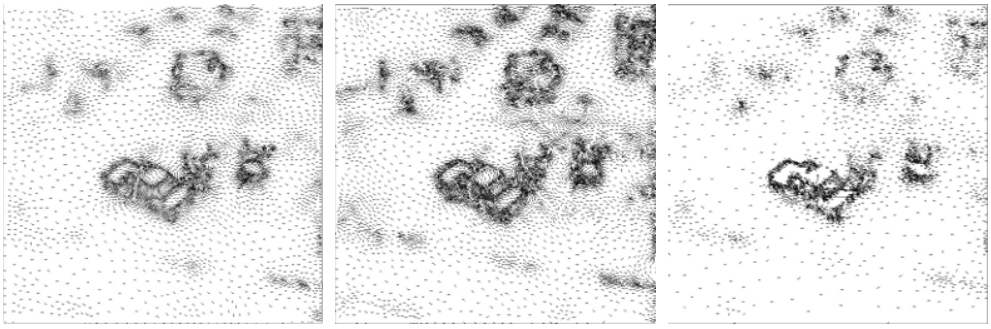

(a) Flow vector iter5 (b) Flow vector iter6 (c) Flow vector iter7

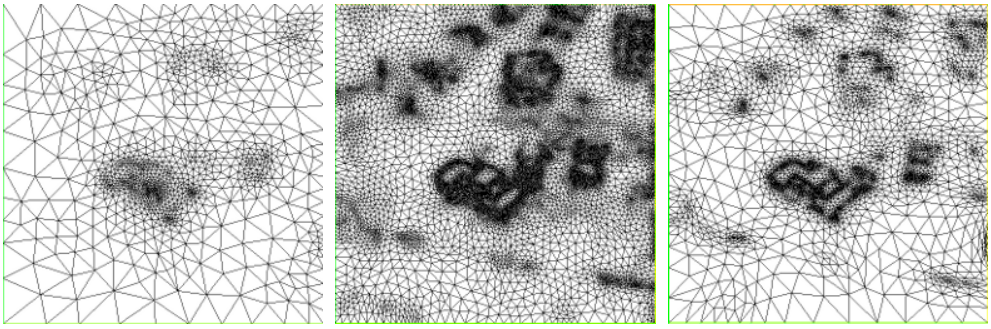

(d) Mesh Iter0 (e) Mesh Iter5 (f) Mesh Iter7

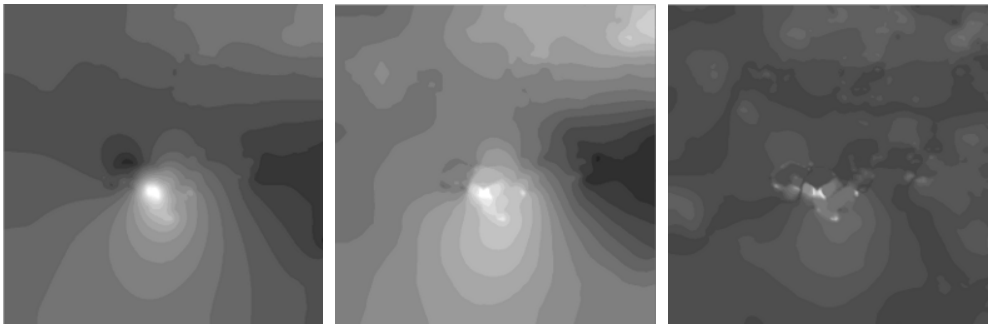

(g) Flow magnitude Iter0 (h) Flow magnitude Iter2 (i) Flow magnitude Iter5

Figure 5.9: Taxi sequence with TV regularization and anisotropic case.

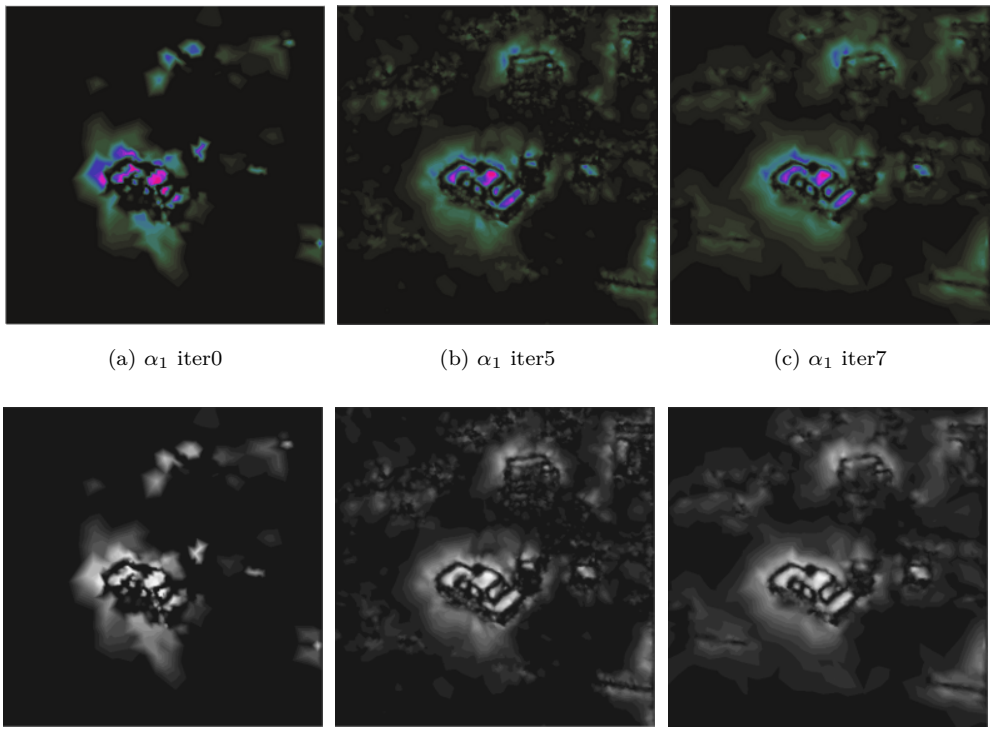

(a) α_1 iter0 (b) α_1 iter5 (c) α_1 iter7

(d) α_2 iter0 (e) α_2 iter5 (f) α_2 iter7

Figure 5.10: Taxi sequence with TV regularization and anisotropic case.

Example 4:

In this example we have considered the moving marble block image sequence, downloaded from the website $http://i21www.ira.uka.de/image_sequences/$ and tested for the anisotropic model (5.9). If we observe from original image which shows three marble blocks but in optic flow just only two blocks appear, the reason is the fulfillment of the actual definition of the optic flow as separation of moving objects from static objects in the video scene. Here in this video image pair only two blocks move and third one is static which is not appeared in the estimated optic flow. Though the TV regularization has robust edge enhancement properties but as the adaptive control of regularization given in this thesis is a novel numerical method for computer vision problems, therefore we have conducted various experiments to justify the claim of our numerical strategy. In the case of marble image sequence with the anisotropic model we have obtained an improved adaptive process and accuracy in the dense flow field with sharp edges. Initially we consider a very large value of alpha as $\alpha_1 = 5000$ and second as smaller than previous as $\alpha_2 = 500$. One can observe the robustness of the algorithm specially in this case where a coarse grid with larger sized triangles is controlled by the smoothness functions α_1, α_2 and the refinement occurs in various directions by an automatic adaptive control of regularization. We have observed that the anisotropy in the adaptive procedure improves the quality of the numerical solution of the given nonlinear model. We perform the eight iterations of adaption in this case. The results on various iterations are given with captions. The scales of values for color images should be considered as said in the previous examples.

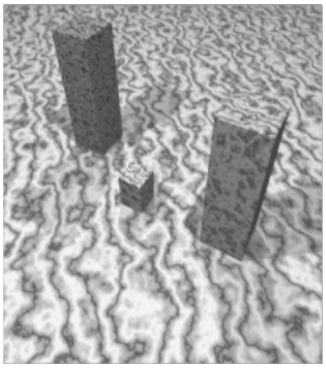

(a) Marble image sequence 43rd frame

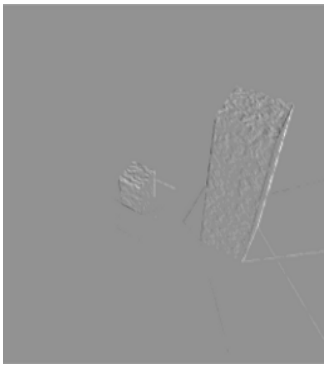

(b) Time derivative f1-f2

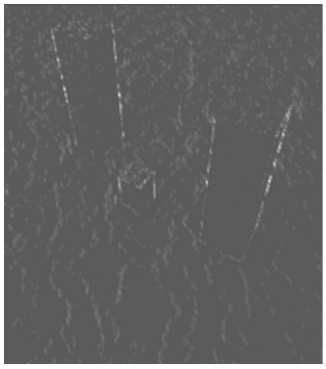

(c) Structure tensor J_ϱ

(d) Flow field iter2

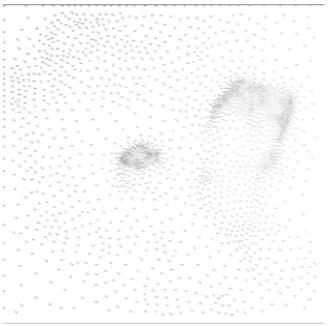

(e) Flow field iter4

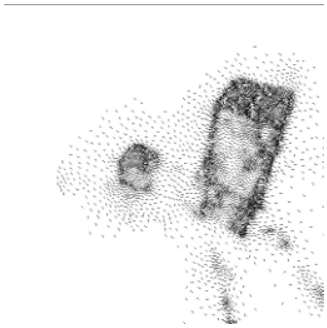

(f) Flow field iter7

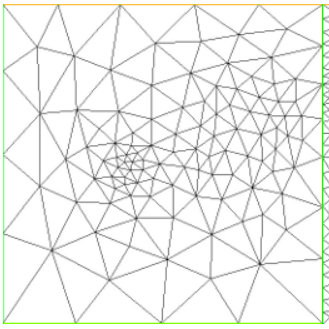

(g) Mesh after iter0

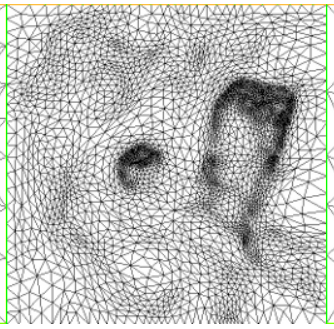

(h) Mesh after iter4

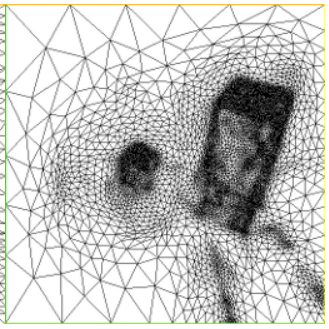

(i) Mesh after iter6

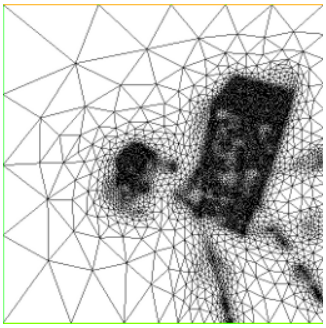

(j) Mesh after iter7

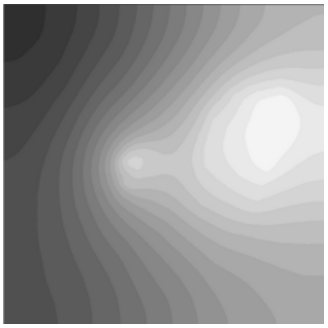

(k) Magnitude flow field iter0

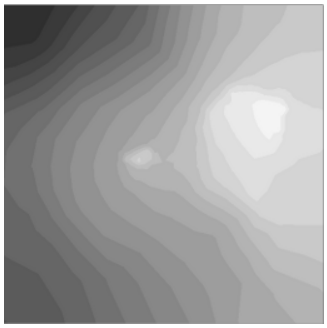

(l) Magnitude flow field iter2

Figure 5.11: Marble image sequence and TV regularization with anisotropic case.

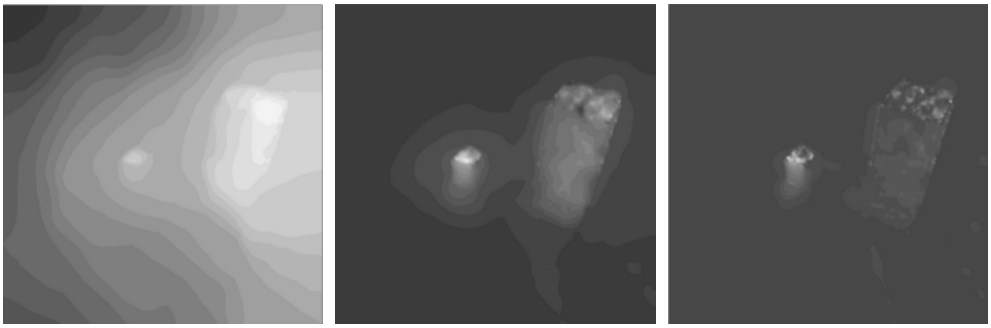

(a) Magnitude flow field iter4 (b) Magnitude flow field iter6 (c) Magnitude flow field iter7

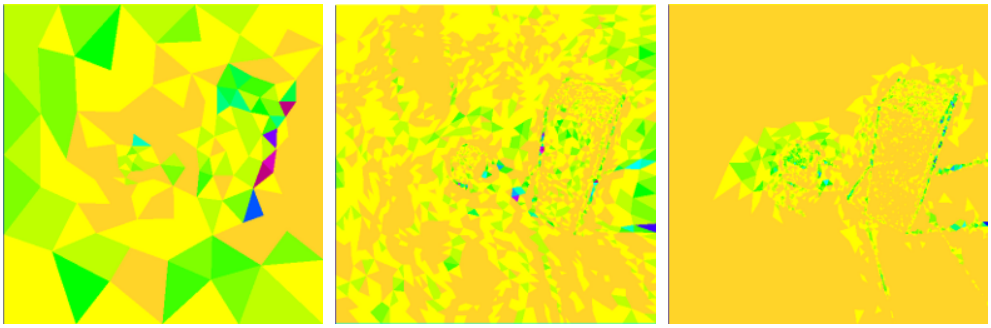

(d) Error indicator η_K after iter0 (e) Error indicator η_K after iter4 (f) Error indicator η_K after iter7

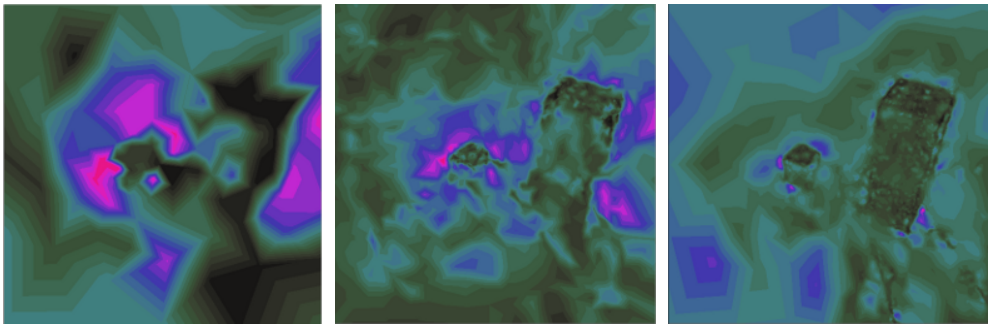

(g) α_1 after iter0 (h) α_1 after iter4 (i) α_1 after iter7

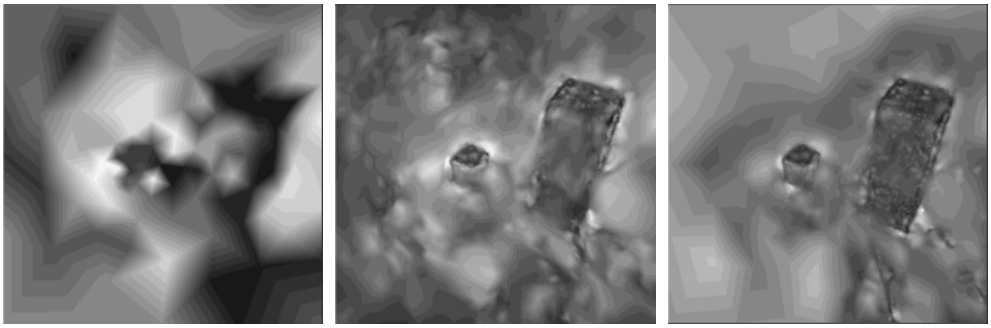

(j) α_2 after iter0 (k) α_2 after iter4 (l) α_2 after iter7

Figure 5.12: Marble image sequence and TV regularization with anisotropic case.

5.6 TV regularization with regularized data term

We consider a nonlinear model in this section which is given by the following energy functional.

$$\mathbf{E}(\mathbf{u}) = \int_\Omega \left(\psi_1(\mathbf{u}^T J_\varrho(\nabla f)\mathbf{u}) + \alpha(\mathbf{x})\psi_2(|\nabla \mathbf{u}|^2)\right) d\mathbf{x}, \tag{5.17}$$

with

$$\psi_i(s^2) = \beta_i^2\sqrt{1+\frac{s^2}{\beta_i^2}},\ i = 1, 2. \tag{5.18}$$

where β_i are the small regularization parameters used for technical reasons from computational point of view and α is a given strictly positive, scalar valued, continuous function on Ω.

The minimization problem (5.17)-(5.18) is solved as constraint optimization problem in the space of functions in $\mathbb{R}^2$ of bounded variations i.e. the space of functions $\mathbf{v} = (v_1, v_2)$ such that

$$\int_\Omega (|\nabla v_1| + |\nabla v_2|)d\mathbf{x} \leq +\infty$$

subject to the following optical flow constraint

$$f_t + f_{x_1}u_1 + f_{x_2}u_2 = 0 \tag{5.19}$$

The nonlinear problem (5.17)-(5.18) is used in order to preserve discontinuities. Since the penalizing functions are convex, the next theorem follows from the direct methods of calculus of variations.

Theorem 5.3.. Assuming that the data $\mathbf{f} \in H^1$, the minimization problem (5.1) admits the unique minimum which depends continuously on the data [53].

Using the direct results from the calculation of variation [53], the minimization of energy functional (5.1) is associated to the following Euler-Lagrange equations.

$$\begin{cases} \operatorname{div}(\alpha(\mathbf{x})\psi_2'(|\nabla \mathbf{u}|^2)\nabla u_1) - (\psi_1'(\mathbf{u}^T J_\varrho(\nabla f)\mathbf{u})\left(f_{x1}^2 u_1 + f_{x1}f_{x2}u_2 + f_{x1}f_t\right) = 0 \,\text{in}\,\Omega \\ \operatorname{div}(\alpha(\mathbf{x})\psi_2'(|\nabla \mathbf{u}|^2)\nabla u_2) - (\psi_1'(\mathbf{u}^T J_\varrho(\nabla f)\mathbf{u})\left(f_{x1}^2 u_1 + f_{x1}f_{x2}u_2 + f_{x2}f_t\right) = 0 \,\text{in}\,\Omega \\ \frac{\partial u_1}{\partial n} = \frac{\partial u_2}{\partial n} = 0,\ \text{on}\ \partial\Omega \end{cases} \tag{5.20}$$

where $\psi_i'(s^2) = \frac{1}{\sqrt{1+\frac{s^2}{\beta_i^2}}}$, i=1,2

We set $\mathbf{f} = (-\psi_1'(\mathbf{u}^T J_\varrho(\nabla f)\mathbf{u})\, f_{x_1} f_t, -\psi_1'(\mathbf{u}^T J_\varrho(\nabla f)\mathbf{u})\, f_{x_2} f_t)^T$, and $\mathbf{u} = (u_1, u_2)^T$,

where f_{x_1}, f_2 and f_t stands for the derivatives with respect to x_1, x_2 and t.

The weak formulation of (5.20) reads:

$$\left\{\begin{array}{c} \text{Find } \mathbf{u} \in H^1(\Omega) \text{ such that} \\ \int_\Omega \alpha(\mathbf{x})\psi_2'(|\nabla \mathbf{u}|^2)\nabla \mathbf{u} : \nabla \mathbf{v} d\mathbf{x} + \int_\Omega \psi_1'(\mathbf{u}^T J_\varrho \mathbf{u}) J_\varrho \mathbf{u} \cdot \mathbf{v}\, d\mathbf{x} = \int_\Omega \psi_1'(\mathbf{u}^T J_\varrho \mathbf{u})\mathbf{f} \cdot \mathbf{v} d\mathbf{x} \\ \forall \mathbf{v} \in H^1(\Omega) \end{array}\right. \quad (5.21)$$

We introduce the notations: for $\mathbf{u}, \mathbf{v} \in H^1(\Omega)$

$$(5.22) \qquad a_\alpha(\mathbf{u}, \mathbf{v}; \mathbf{u}) = \int_\Omega \alpha(\mathbf{x})\psi_2'(|\nabla \mathbf{u}|^2)\nabla \mathbf{u} : \nabla \mathbf{v} d\mathbf{x} + \int_\Omega \psi_1'(\mathbf{u}^T J_\varrho \mathbf{u}) J_\varrho \mathbf{u} \cdot \mathbf{v}\, d\mathbf{x}$$

$$(\mathbf{f}, \mathbf{v}) = \int_\Omega \psi_1'(\mathbf{u}^T J_\varrho \mathbf{u})\mathbf{f} \cdot \mathbf{v} d\mathbf{x}$$

Thus, problem (5.21) consists of finding $\mathbf{u} \in H^1(\Omega)$, such that:

$$(5.23) \qquad a_\alpha(\mathbf{u}, \mathbf{v}; \mathbf{u}) = (\mathbf{f}, \mathbf{v}) \ \forall \mathbf{v} \in H^1(\Omega)$$

5.7 Problem Discretization

Suppose that the domain Ω is polygonal and let we consider a regular family of triangulations $\mathcal{T}_h$ made up of elements which are triangles (or quadrilaterals) with maximum size $h > 0$, satisfying the usual admissibility assumptions, i.e:

Admissibility: The intersection of two different elements is either empty, a vertex, or a whole edge.

Shape regularity: The ratio of the diameter of any element $T \in \mathcal{T}_h$ to the diameter of its largest inscribed ball is bounded by a constant σ independent of T and h.

$$X_h := \left\{\mathbf{v}_h \in C(\bar{\Omega}) | \forall K \in \mathcal{T}_h, \mathbf{v}_{h|T} \in P_1(K)^2\right\}$$

We denote by $J_{\varrho,h}$ a finite element approximation of the matrix $J_{\varrho,h}$ obtained as follows: for any $K \in \mathcal{T}_h$ we denote by $J_{\varrho,h,K}$ the matrix where the coefficients.

$$(J_{\varrho,h,K})_{i,j} = \frac{1}{|K|}\int_K (J_{\varrho,})_{i,j}\, d\mathbf{x},\ 1 \le i,j \le 2$$

are the mean values of the coefficients of J_ϱ on K. The matrix $J_{\varrho,h}$ is the piecewise constant matrix which take the value $J_{\varrho,h,K}$ on the element K.

The discrete problem reads

$$\begin{cases} \text{Find } \mathbf{u}_{\alpha,h} \in X_h \text{ such that} \\ a_{\alpha,h}(\mathbf{u}_h, \mathbf{v}_h; \mathbf{u}_h) = (\mathbf{f}, \mathbf{v}_h) \qquad \forall \mathbf{v}_h \in X_h \end{cases} \tag{5.24}$$

where

$$a_\alpha(\mathbf{u}_h, \mathbf{v}_h; \mathbf{u}_h) = \int_\Omega \alpha(\mathbf{x})\psi_2'(|\nabla \mathbf{u}_h|^2)\nabla \mathbf{u}_h : \nabla \mathbf{v}_h d\mathbf{x} + \int_\Omega \psi_1'(\mathbf{u}_h^T J_{\varrho,h}\mathbf{u}_h) J_{\varrho,h}\mathbf{u}_h \cdot \mathbf{v}_h \, d\mathbf{x}$$

and

$$(\mathbf{f}, \mathbf{v}_h) = \int_\Omega \psi_1'(\mathbf{u}_h^T J_{\varrho,h}\mathbf{u}_h)\mathbf{f} \cdot \mathbf{v}_h d\mathbf{x}$$

5.8 Residual error indicator

We propose the following a posteriori residual error indicator as given in [12, 44, 88], which is an upper bound for the error in $L^2(\Omega)$ norm as shown in [12]. For each element $K \in \mathcal{T}_h$ we define the error indicator η_K in L^2 norm as

(5.25)

$$\eta_K = \alpha_K^{-1/2} h_K \left\| \mathbf{f} - \psi_1'(\mathbf{u}_h^T J_{\varrho,h}\mathbf{u}_h) J_{\varrho,h}\mathbf{u}_h \right\|_{L^2(K)^2} + \frac{1}{2} \sum_{e \in S_h} \alpha_e^{-\frac{1}{2}} h_e^{\frac{1}{2}} \left\| [\alpha \psi_2'(|\nabla \mathbf{u}_h|^2)\nabla \mathbf{u}_h \cdot \mathbf{n}_e]_e \right\|_{L^2(e)^2}$$

Where h_K is the diameter of $K \in \mathcal{T}_h$ and h_e is denoted as size of edge $e \in S_h$(set of edges in $\mathcal{T}_h$). $\mathbf{n}_e$ is denoted as unit vector normal to the edge e. $[\cdot]$ denotes the jump over the edge between two elements.

5.9 Adaptive control and numerical experiments

We apply our algorithm as given in section the 5.5 and solve the nonlinear model to compute the optic flow $\mathbf{u}$ and show the mesh adaption procedure on grid for various adaptive iterations. We perform our experimental work on the two different real world sequences, results are given below.

5.9.1 Example 5:

In this example we consider a traffic intersection video sequence available at http://i21www.ira.uka.de/image-sequences/. We perform the adaptive control of regularization using 15 iterations of adaption and check the performance of our method for the nonlinear variational model (5.17)(TV regularization with regularized data term). One can observe that the regularization of data term in this model is different from the linear model as given in chapter two which is base on complementary approach. The regularization parameters β_i are kept very small to avoid the division by zero and dominating regularization effects on the parameter α. From our simulations we observe the efficiency of our algorithm as well as the numerical contribution by the improvements in variational models simultaneously. The improved version of variational model yields more betterment in the visualization quality of the dense flow field which is justified from the various examples in this thesis. The simulation results are given on the same pattern as in the previous examples. One can compare the results for different models given in this thesis and for different image sequences considered so for. Though we have not introduced any new model in this thesis but using exiting ones, our work falls in the category of advanced computational strategies for variational models in image processing. The numerical results are given below.

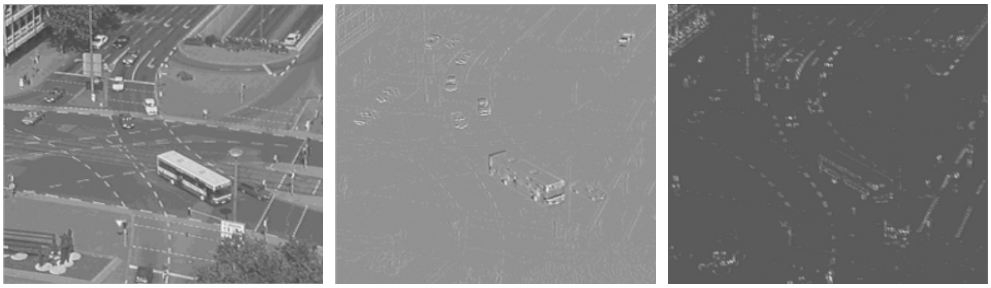

(a) Traffic intersection image sequence, sixth frame

(b) Time derivative f1-f2

(c) Structure tensor J_ϱ

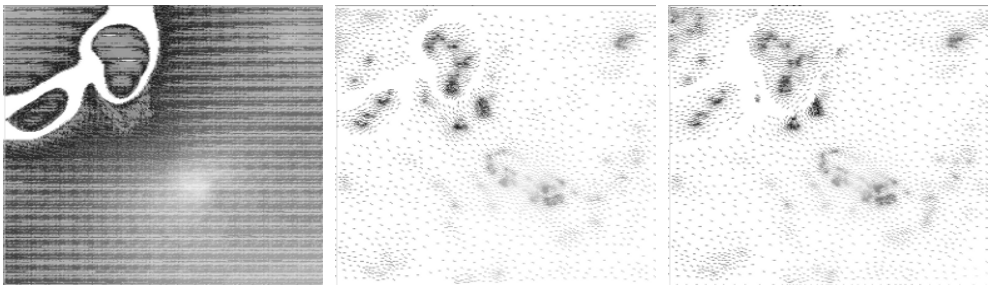

(d) Optic flow iter0

(e) Optic flow iter1

(f) Optic flow iter2

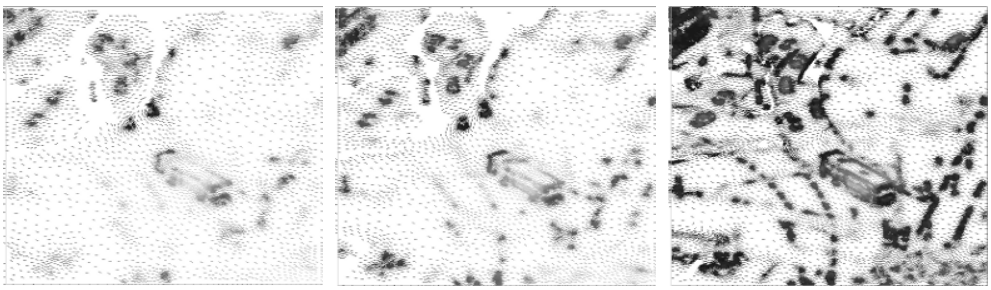

(g) Optic flow iter3

(h) Optic flow iter5

(i) Optic flow iter8

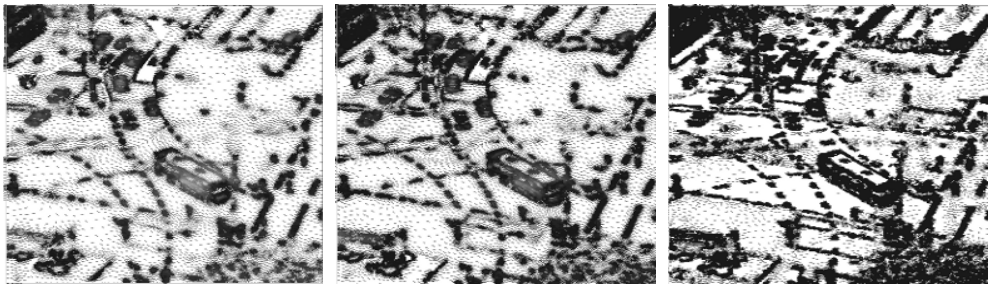

(j) Optic flow iter9

(k) Optic flow iter10

(l) Optic flow iter12

Figure 5.13: Traffic intersection image sequence and and TV regularization with improved data term.

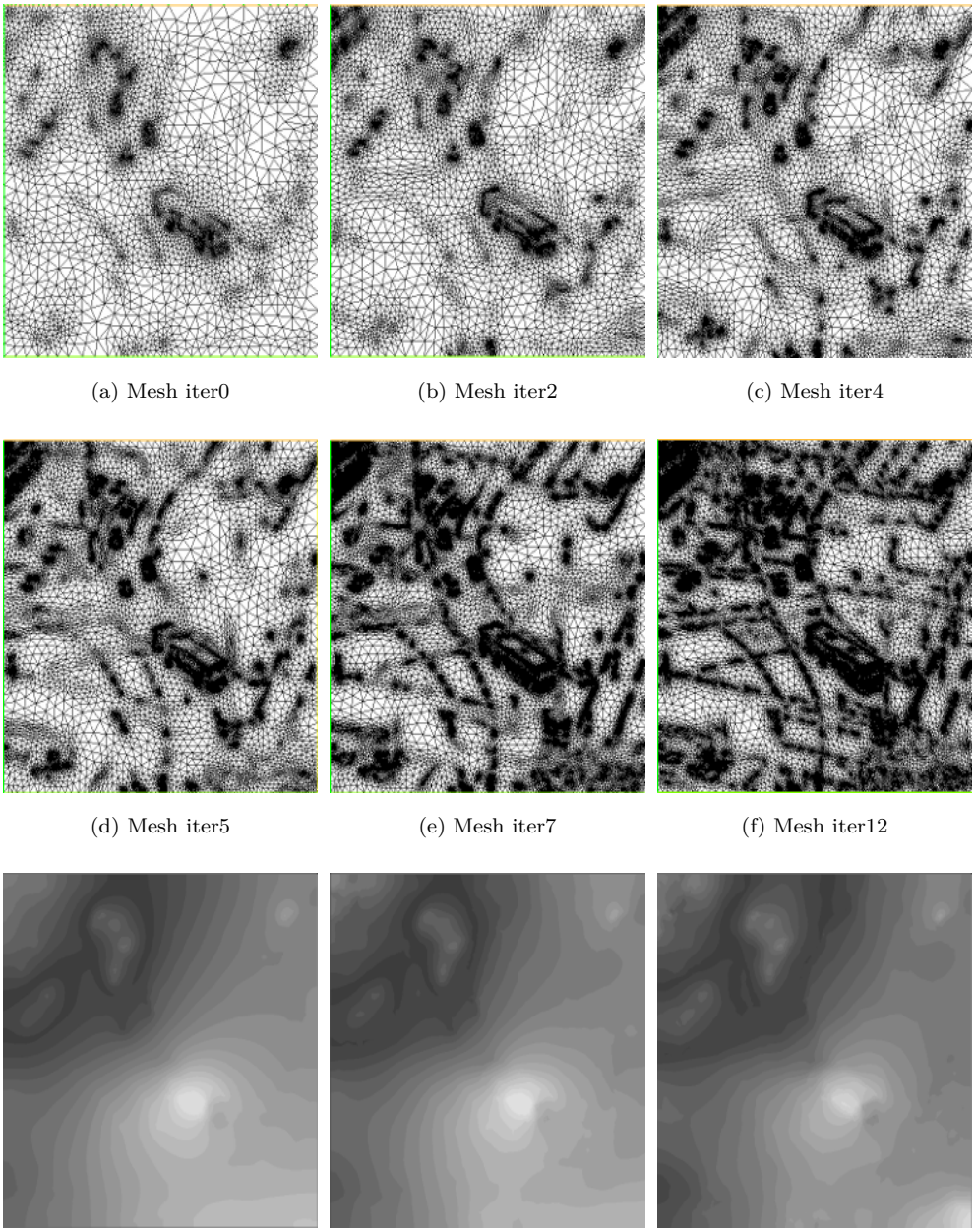

(a) Mesh iter0 (b) Mesh iter2 (c) Mesh iter4

(d) Mesh iter5 (e) Mesh iter7 (f) Mesh iter12

(g) Magnitude optic flow iter0 (h) Magnitude optic flow iter1 (i) Magnitude optic flow iter2

Figure 5.14: Traffic intersection image sequence and TV regularization with improved data term.

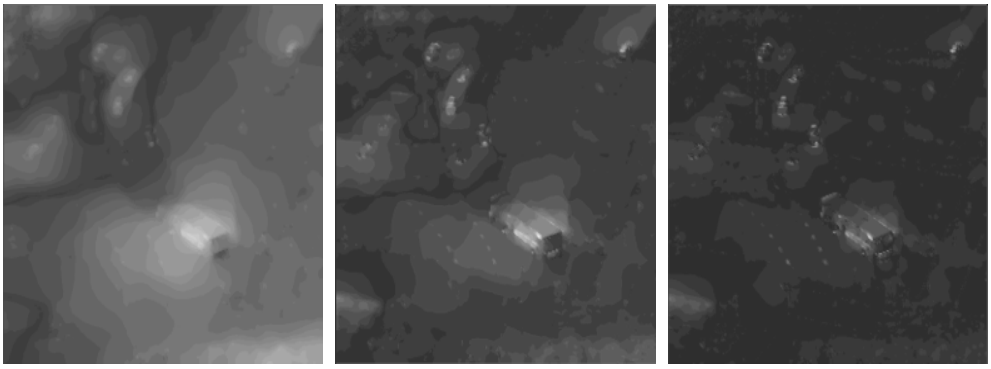

(a) Magnitude optic flow iter6 (b) Magnitude optic flow iter9 (c) Magnitude optic flow iter12

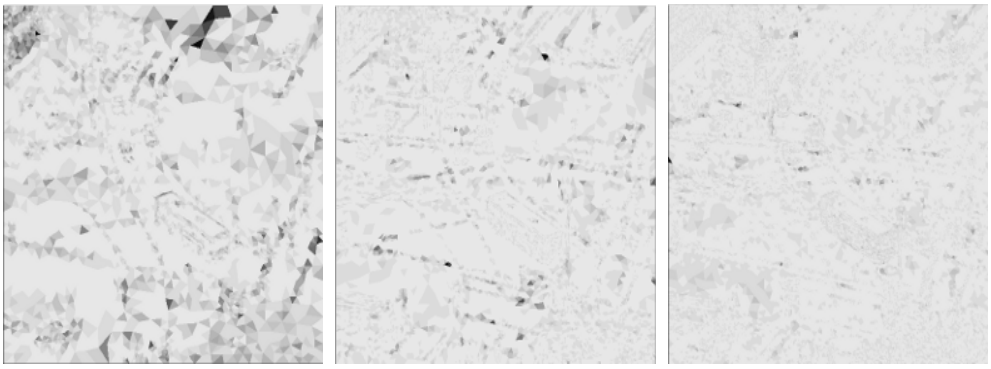

(d) Error density η_K iter0 (e) Error density η_K iter6 (f) Error density η_K iter12

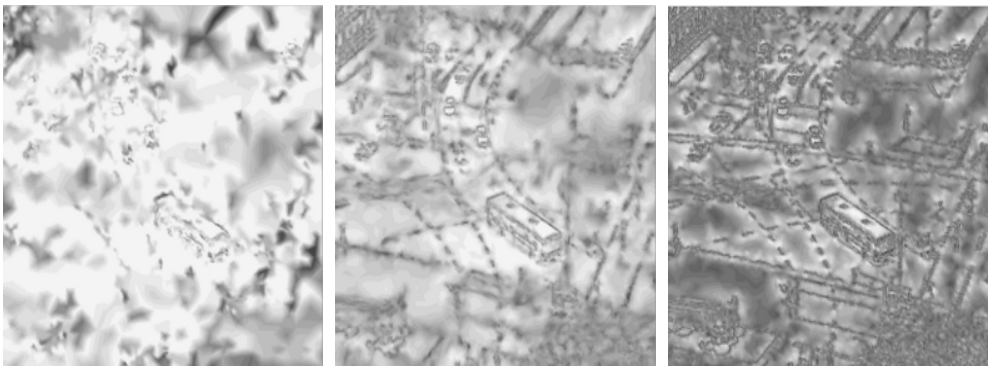

(g) Distribution of $log(\alpha)$ iter0 (h) Distribution of $log(\alpha)$ iter6 (i) Distribution of $Log(\alpha)$ iter12

Figure 5.15: Traffic intersection image sequence and TV regularization with improved data term.

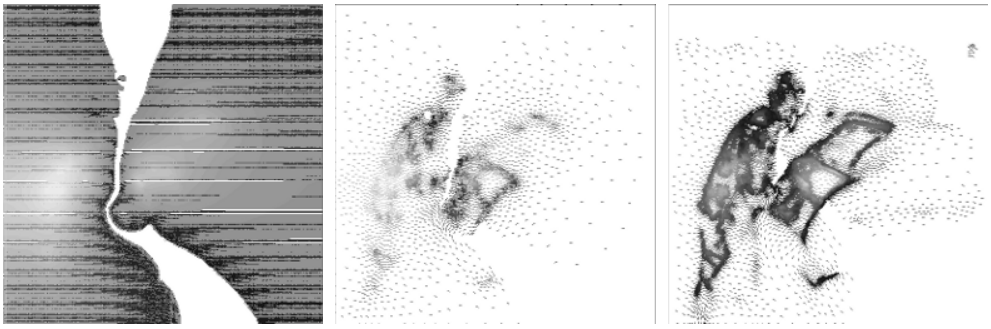

(a) Flow vector iter0 (b) Flow vector iter2 (c) Flow vector iter6

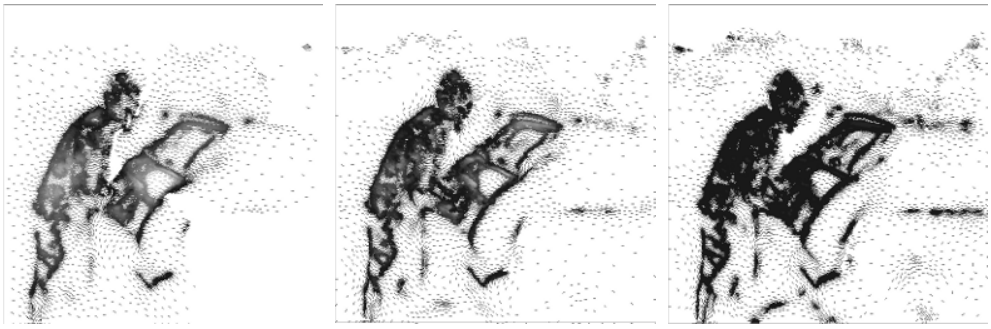

(d) Flow vector iter8 (e) Flow vector iter10 (f) Flow vector iter12

Figure 5.16: Minicooper image sequence and TV regularization with improved data term.

5.9.2 Example 6:

In this example we consider the mini-cooper image sequence and compute the optic flow using the nonlinear model (5.17). Our interest for this example is to compare the performance of TV regularization using isotropic case with the TV regularization using improved data term. We perform thirteen adaptive iterations. From the experimental observations given below we observe that the TV optic flow model with regularized version of data term yields the significant improvement in the sharpness of dense flow field.

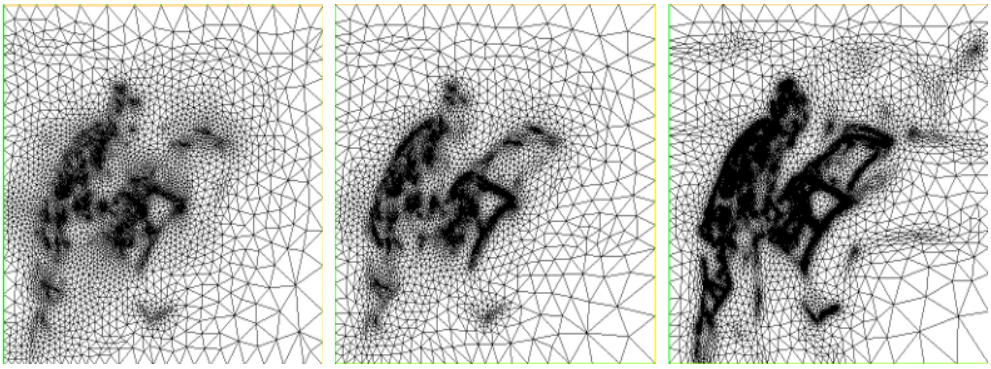

(a) Mesh iter0 (b) Mesh iter2 (c) Mesh iter6

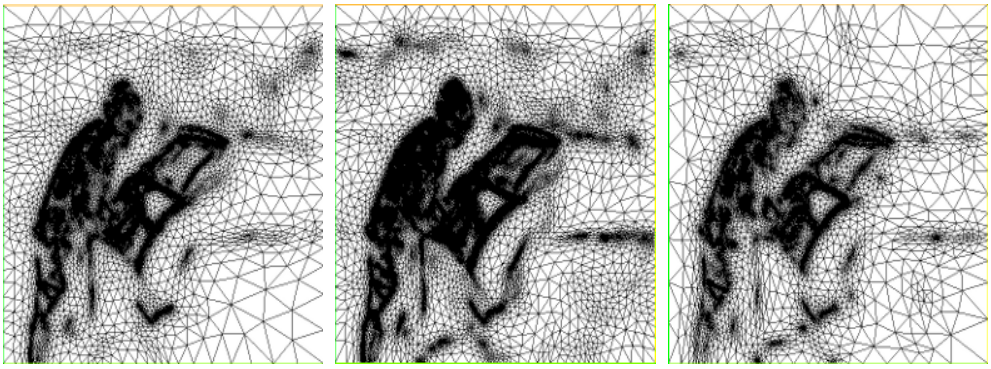

(d) Mesh iter8 (e) Mesh iter10 (f) Mesh iter12

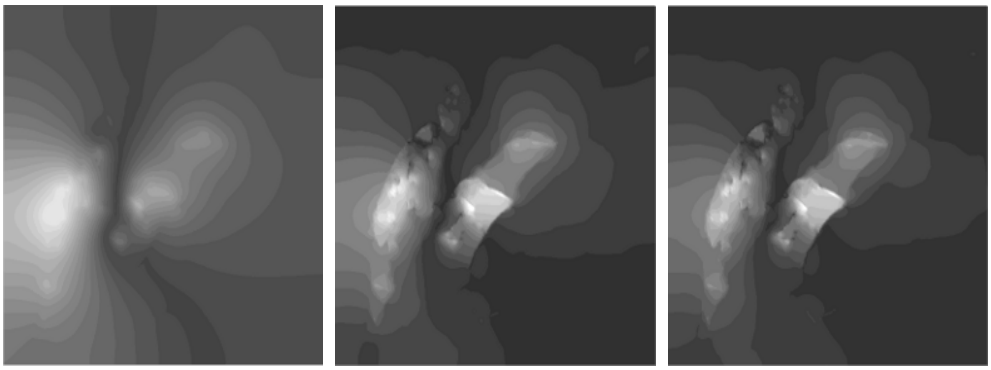

(g) Magnitude of flow field iter0 (h) Magnitude of flow field iter4 (i) Magnitude of flow field iter6

Figure 5.17: Mini-cooper image sequence and TV regularization with improved data term.

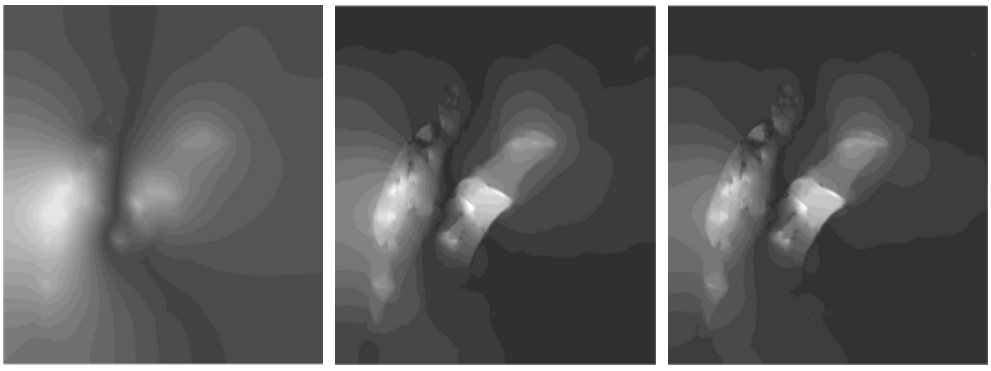

(a) Magnitude of flow field iter0 (b) Magnitude of flow field iter4 (c) Magnitude of flow field iter6

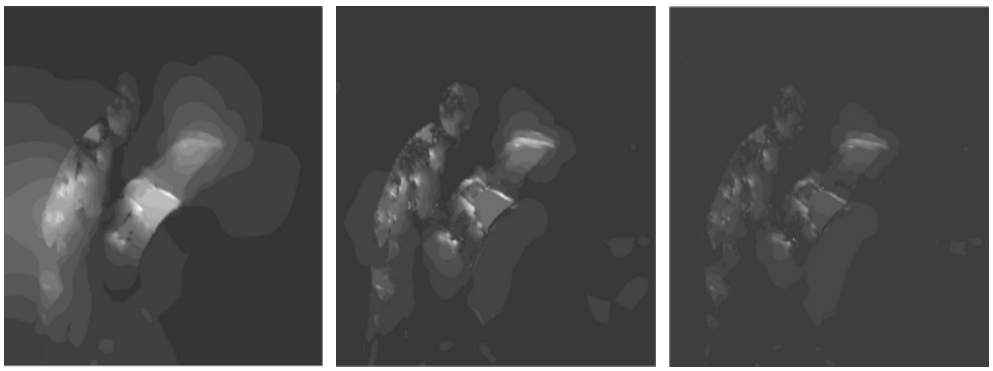

(d) Magnitude of flow field iter8 (e) Magnitude of flow field iter10 (f) Magnitude of flow field iter12

Figure 5.18: Mini-cooper image sequence and TV regularization with improved data term.

5.10 Conclusion

The novel adaptive algorithm given in this thesis was tested on various variational models for computation of optic flow. From the overall performance of the adaptive procedure one can observe that the algorithm performs reasonably well in achieving a robust adaptive control of the regularization specially for the image motion problems based on the various variational approaches discussed in this thesis (claim of algorithm is reasonably justified for all linear and nonlinear models considered in this thesis). The TV regularization (isotropic case) yields improved results with justification of the discontinuity preservation claim as compared to linear model for complementary optic flow(results with smoothed edges). The TV regularization with anisotropic approach improved the quality of the given algorithm with sharp results, specifically if we see the moving marble blocks video sequence example, that a significant improvement in the sharpness is observed. Specially the case of the regularization from a very coarse grid is of interest, when the dramatic regularization effects appear on every next adaptive iteration (the case with very large initial value of the α_1). For the conformation one can see the mesh after iter0(initial iteration) in the computations for the marble sequence where we have obtained a very coarse grid (with the elements of large sizes), which is controlled by the anisotropic adaptive process. A significant improvement in the dense flow field with sharp edges is achieved in the case of TV regularization with anisotropic case if we compare with quadratic regularization model given in chapter two. An improvement is observed in the sharpness of optic flow field in the case of TV regularization using improved data term vs TV regularization with isotropic case. From the overall performance the TV regularization is a robust approach as compared to the quadratic regularization. Moreover the improved data term yields the improvement in the sharpness of dense flow field.

Chapter 6

An Adaptive control for Perona-Malik equation and its Applications in Image Denoising

6.1 Introduction

In the preceding chapters we discussed some regularization techniques for ill-posed problems in image motion, where we have successfully applied our local adaptive strategy on various image motion problems. We are interested to extend our idea for other image processing problems, keeping this in view, we propose an adaptive control for a denoising problem. Though the experimental results in this case are looking satisfactory but this novel adaptive approach is still at its beginning stage, since the regularization strategy we have discussed in this thesis is not conformed for the denoising problems and still is under progress. Moreover we are applying here this idea on the energy functional which is nonconvex, therefore the choice of local adaptive parameters is still doubtful.

6.1.1 Denoising Problem

In this chapter we discuss the problem of image reconstruction of an original image u from a given noisy image f on some open and bounded domain $\Omega \subset \mathbb{R}^d$. We assume that image f was generated from image u by adding noise $\mathbf{n}$, we can write:

$$f = u + \mathbf{n}. \tag{6.1}$$

Image denoising problem is of crucial importance in the area of image processing and a lot of research is conducted on this subject during last two decades[76, 32, 30, 83, 84, 38, 95, 74]. The credit of much interest in PDE's based approach for the denoising initially goes to the pioneering proposal of Rudin, Osher, and Fatemi [76], where they proposed TV regularization approach for image restoration. This method has been applied to a wide range of applications in the computer vision and image processing. We have already brought in to consideration the approach of TV regularization for stereo vision and optic flow problems in previous chapters.

This chapter reviews the main application, namely the smoothing and restoration of images. We propose some regularization strategies for numerical solution of the Perona-Malik equation. The Perona-Malik equation is originated from image segmentation

problem [74]. We apply this diffusion model on denoising problem and propose a numerical algorithm based on adaptive finite element method using unstructured grid as discrete domain for the given image. In this chapter we discuss the Perona-malik functional and some of its mathematical expectations and approximations. We propose the following parabolic problem to separate the signal $u :\longrightarrow \mathbb{R}^+ \times \Omega$ from a given noisy image f.

$$\partial_t u = \mathtt{div}(\alpha(\mathbf{x})\mathrm{g}(|\nabla u|^2)\nabla u) \text{ in } \mathbb{R}^+ \times \Omega \tag{6.2}$$

$$u(0, \mathbf{x}) = f(\mathbf{x}) \text{ on } \Omega$$

$$\frac{\partial u}{\partial \nu} = 0 \text{ on } \mathbb{R}^+ \times \Omega$$

where $\Omega \subseteq \mathbb{R}^d$ is a bounded open set. The $\alpha(\mathbf{x})$ is strictly positive scalar valued continuous smoothing function on domain Ω. The problem (6.2) uses diffusivities that are decreasing in $|\nabla u|$, e.g the Charbonnier diffusivity [95]

$$\mathrm{g}(s^2) := \frac{1}{\sqrt{1 + s^2/\lambda^2}} \tag{6.3}$$

The Charbonnier diffusivity (6.3) is inherited from the regularized version of total variation minimization problem an discussed for TV stereo problem in chapter three and four. An other fast decreasing is called Perona-Malik diffusivity (6.4).

$$\mathrm{g}(s^2) := \frac{1}{1 + s^2/\lambda^2} \tag{6.4}$$

λ is a contrast parameter and can be termed as threshold between diffusion and edge enhancement processes. We proceed further with some mathematical discussion on problem (6.2) using Perona-Malik diffusivity (6.4).

6.2 One-dimensional case$(d = 1)$

$$\partial_t u = \left(\frac{u_x}{1 + u_x^2}\right)_x, \; u(0) = u_0 \tag{6.5}$$

in $I \times (0, T)$, $I = (0, l) \subset \mathbb{R}$. We have assumed for simplicity the regularization parameters $\lambda = 1$ and $\alpha = 1$. In one-spatial dimension the equation is the gradient flow of

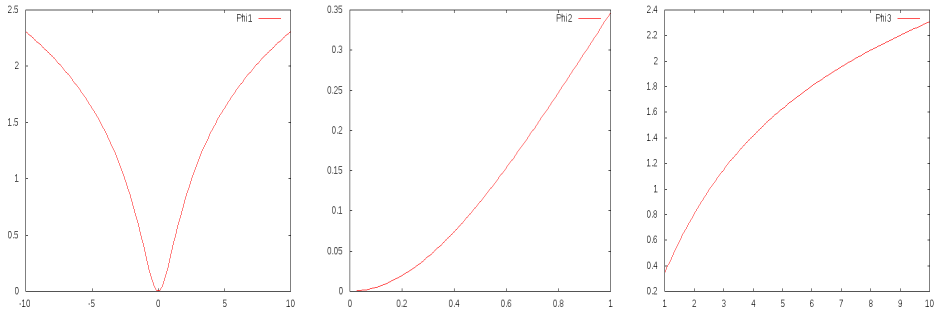

Figure 6.1: plots for the function $\phi(s)$

on various intervals.

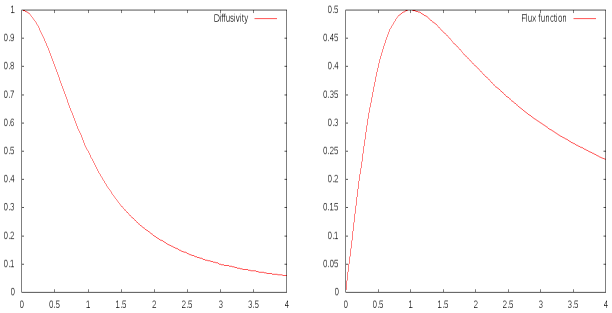

Figure 6.2: Plots for Perona-malik diffusivity g(s) and flux function $\Phi(s)$.

nonconvex functional

$$F^{\phi}(u) = \int_I \phi(u_x)dx \quad \phi(s) := \frac{1}{2}\log(1+s^2) \tag{6.6}$$

$\phi(s)$ is shown in following figure 6.2.

Remark 6.1: On can observe the convexity of $\phi(s)$ beside zero and convex-concave behavior away from zero. The convex-concave behavior of the function $\phi(s)$ depends on whether $|s|$ is smaller or larger than one. As in the case of (6.5), the main qualitative features of ϕ are sublinearity at infinity, the strict convexity for $|s|$ small and strict concavity for $|s|$ large.

From diffusivity (6.4) it follows that the flux function

$$\Phi(s) := s\,\mathrm{g}(s^2) \tag{6.7}$$

satisfies

$$\Phi'(s) \geq 0 \text{ for } |s| \leq 1 \text{ (Forward diffusion)}$$

and

$$\Phi'(s) < 0 \text{ for } |s| > 1 \text{ (Backward diffusion)}$$

See the figure 6.2.

Remark 6.2: Inspite of nonnegative diffusivity Perona-Malik equation is forward parabolic type for $|u_x| \leq 1$ and of backward parabolic type for $|u_x| > 1$. Indeed, the backward parabolic character of equation (6.5) in the regions where $|u_x| > 1$ makes the equation ill-posed.

The ill-posed behavior of Perona-malik diffusion is interesting in the case of two dimensional signals specially for the image restoration and edge detection problems, where the forward diffusion regions and backward diffusion regions are separated by λ, on the left of λ we are in diffusion mode and on the right hand side of λ one is therefore in the edge enhancing mode. Let we describe the Perona-Malik equation in the higher dimensional case.

6.3 Two-dimensional case$(d \geq 2)$

Perona-Malik functional in two-dimensional case:

$$F(u) = \frac{1}{2}\int_{\Omega} \log(1 + \alpha(\mathbf{x})\,|\nabla u|^2)d\mathbf{x} \tag{6.8}$$

the gradient of (6.8) can be written as [60, 50]

$$\nabla F(u) = -\mathtt{div}(\alpha(\mathbf{x})\mathrm{g}(|\nabla u|^2)\nabla u) \tag{6.9}$$

The gradient flow

$$\partial_t u = -\nabla F(u) \tag{6.10}$$

Thus the gradient flow of equation $F(u)$ is the Perona-Malik equation:

$$\partial_t u = \mathtt{div}(\alpha(\mathbf{x})\mathrm{g}(|\nabla u|^2)\nabla u) \text{ in } \Omega \times \mathbb{R}^+ \tag{6.11}$$

In the case of $d \geq 2$ diffusion process depends on the Hessian matrix of the function $\log(1+|\nabla u|^2)$. The function is convex for $|\nabla u| \leq 1$ and gives forward diffusion, when $|\nabla u| > 1$ function is neither convex nor convex therefore it will give one negative eigenvalue of Hessian matrix value in radial direction and $d-1$ positive eigenvalues in orthogonal directions.

Remark 6.3 In this above convex-concave behavior of Perona-Malik equation when $|\nabla u| \leq 1$ we are in subcritical zone where we have forward diffusion and in second case when $|\nabla| > 1$ we are in supercritical zone where we have the backward diffusion in the direction of gradient which yields in result the enhancement of edges. For more detailed discussion on Perona-Malik diffusion we refer the reader to [74, 60, 50, 95, 27].

6.4 Solution of Nonlinear problem (6.2)

There are different possible numerical strategies to solve the given non-linear problem, mostly the numerical practitioners use finite difference schemes using the rectangular grids to solve the problems in the image processing and computer vision, instead we propose the adaptive finite element method with triangular grids. Moreover we propose an implicit finite element discrete scheme which is unconditionally stable.

Proposition 6.3 Our numerical strategy is base on variational method which consists in defining a bilinear form $a(u,v)$ and a linear form (f,v). We propose that the problem (6.2) admits a weak solution and solving the evolution problem (6.2) is equivalent to solve associated variational problem

$$\begin{cases} \text{Find } \ u \in H^1 \ \text{ such that} \\ (\frac{\partial u}{\partial t}, v) + a(u, v; u) = (f, v) \qquad \forall v \in H^1 \end{cases} \tag{6.12}$$

where

$$a(u,v;u) = \int_\Omega \alpha(\mathbf{x}) \mathrm{g}(|\nabla u|^2) \nabla u : \nabla v d\mathbf{x} \tag{6.13}$$

$$(f,v) = \int_\Omega f\, v d\mathbf{x} \tag{6.14}$$

6.5 Discretization

Suppose that the domain Ω is polygonal and let we consider a regular family of triangulations $\mathcal{T}_h$ made up of elements which are triangles (or quadrilaterals) with maximum size $h > 0$, satisfying the usual admissibility assumptions, i.e:

Admissibility: the intersection of two different elements is either empty, a vertex, or a whole edge.

Shape regularity: The ratio of the diameter of any element $K \in \mathcal{T}_h$ denoted by h_K to the diameter of its largest inscribed ball denoted by ρ_K is bounded independently of K. We denoted the shape parameter as $C_\tau = \max_{K\in\tau} \frac{h_K}{\rho_K}$. Given element $K \in \mathcal{T}$, we define K^* as the union of all elements in $\mathcal{T}_h$ that share atleast one side with K, and $B_h(K)$ as union of all elements in $\mathcal{T}_h$ that have empty intersection with K. We introduce the following discrete space as $X_h \subset X$, which denotes the space of continuous piecewise affine finite elements over $\mathcal{T}_h$, that is

$$X_h := \left\{ v_h \in C^0(\bar{\Omega}) | \forall K \in \mathcal{T}_h, v_{h|T} \in P_1(K) \right\}$$

where $P_1(K)$ denotes space of all polynomials in $\mathbb{R}^2$ of degree equal to one.

The discrete form reads an implicit time dependent discrete scheme as

$$(\frac{u_h^{k+1} - u_h^k}{\tau}, v_h) + \tilde{a}(u_h^{k+1}, v_h; u_h^k) = (f, v_h) \qquad \forall v_h \in X_h \tag{6.15}$$

where the time dependent bilinear form $\tilde{a}(u_h^{k+1}, v_h; u_h^k)$ is denoted as

$$\tilde{a}(u_h^{k+1}, v_h; u_h^k) = \int_\Omega \frac{\alpha^k}{1 + ((\partial_x u_h^k)^2 + (\partial_x u_h^k)^2)/\lambda^2} \nabla u_h^{k+1} \nabla v_h \tag{6.16}$$

This time dependent bilinear form is symmetric and positive definite. We control the numerical diffusion process in two different ways where in the first category we keep the α and λ as two small constant smoothing parameters throughout the diffusion time T, in this case if we increase the value of λ means we should obtain more diffusion and with decrease in the value of λ we expect the enhancement in the edges of degraded image. In the second experimental strategy we keep λ as small constant and α as space variable which is allowed to be refreshed with time, in this case we propose a novel adaptive algorithm for the time dependent problem where the diffusion occurs in the

time and controlled by the diffusion parameter α. We write the implicit scheme (6.15)

$$(I + \tau A_{k+1}))U^{k+1} = (U^k + \tau L) \tag{6.17}$$

where $U = [u_1, u_2 \cdots u_N]$, the diffused grey value at N (number of nodes). The vector L is obtained from the evaluation of the linear form (f, v). This numerical scheme is unconditionally stable. At each time step sparse linear system is solved using conjugate gradient algorithm, computations in this case are made using FreeFem++[43].

6.6 Numerical experiments

6.6.1 Example.1:

We consider the camera man image available at www.imageprocessingplace.com. The image is degraded with white noise of the standard deviation 20. We test our proposed implicit scheme using FreeFem++ [43]. In this example we keep the threshold $\lambda = 8$, $\alpha = 0.001$ and diffusion process is is tested for the different times, we denote the parameter T as the number of time iterations for diffusion process. The results are given for this experiment on various time iterations. As one can observe that with increase in the diffusion time the smoothness increases with the missing of some useful informations from back ground and even from the foreground of the image.

(a) Original image Camera man (b) Noise added SD=20

(c) Denoised $\lambda = 8$ and T=2 (d) Denoised $\lambda = 8$ and T=5 (e) Denoised $\lambda = 8$ and T=20

Figure 6.3: Example 1: Camera man image and diffusion with constant smoothness parameters.

6.6.2 Adaptive strategy

As we know that the original solution is known a priori, therefore it is more convenient to replace the residual error indicator as discussed in last chapters by the L^2 error estimate which is computable quantity and easily fits in our regularization frame work. We define the error estimate E_K on any element K in the L^2 norm as

$$E_K = \|u - u_h\|_{L^2(K)} \tag{6.18}$$

where u is the original solution and u_h is the computed solution. We control the diffusion process by following adaptive algorithm

(1) We start with the cartesian grid $\mathcal{T}_h^0$ corresponding to the image.

(2) **Adaptivity steps:**

- Compute $u_{\alpha_0^0,h}$ on $\mathcal{T}_h^0$ with $\alpha = \alpha^0$ a large constant on initial time $k = 0$. For k=1 to n
- Compute $u_{\alpha^k,h}$ on $\mathcal{T}_h^k$ with $\alpha = \alpha^k$ where we propose the following formula for local choice of α

  The principal of the adaptive regularization process is to decrease the values of α in the regions where the L^2 is large(edges) and and keep it stable in the in the complementary regions. However, for the stability reasons we start with a relatively high initial guess and during the adaptive process α decreases with increase in the time. For automatic choice of α during the adaption we use following formula for each triangle K

  $$\alpha_K^{k+1} = \texttt{max}\left(\frac{\alpha_K^k}{1 + \kappa * ((E_K) - 0.1)^+}, \alpha_{trh}\right) \tag{6.19}$$

  where α_{trh} is a threshold and κ is a coefficient chosen to control the rate of decreasing in α, $(u^+) = \texttt{max}(u, 0)$.

6.6.3 Example 2:

In this example we consider Lenna image and degraded with white noise of standard deviation 40 , we performed 5(time) iterations of diffusion with our adaptive

(a) Original image Lena (b) Added noise SD=40 (c) Diffusion after iter0

(d) Diffusion after iter1 (e) Diffusion after iter2 (f) Diffusion after iter3

Figure 6.4: Lenna image and adaptive process

algorithm given above where the initial value of $\alpha = 200$ and the value of $\lambda = 0.01$ is kept constant throughout the diffusion process. We observed that the adaptive algorithm shows strong and fast diffusion performance with respect to diffusion time which yields high blurring effects, resulting in the missing of some useful informations quickly after two iterations. Though one can see from the L^2 error which is larger at edges and adaptive parameter α automatically decreases and controls the rise of error during the diffusion process. As the problem is ill-posed and very sensitive in contrast parameter λ acting as threshold of diffusion, therefore our numerical strategy still need some more improvements to achieve our goal in obtaining the sharp results with automatic control of regularization on extra blurring effects with respect to the long time diffusion. The results are given with the captions on the various time iterations.

(a) Diffusion after iter4

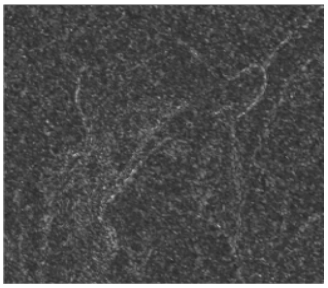

(b) Error after iter0

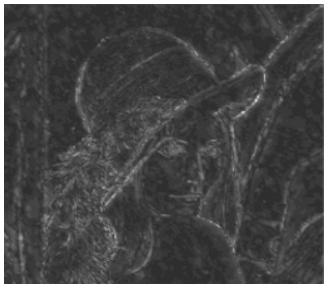

(c) Error after iter1

(d) Error after iter2

(e) Error after iter3

(f) Error after iter4

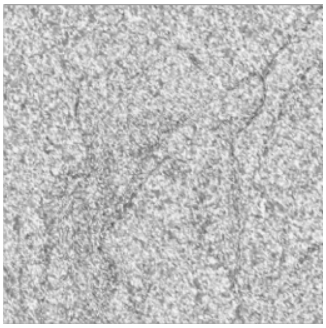

(g) Choice of α after iter0

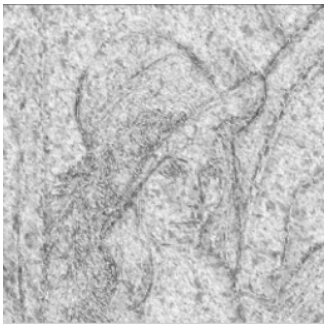

(h) α after iter1

(i) α after iter2

(j) α after iter3

(k) α after iter4

Figure 6.5: Lenna image and adaptive process

Chapter 7

Conclusion

7.1 Conclusion

In this thesis we have studied the problems of computing the disparity map in stereo-vision and the estimation of the optic flow with variational methods. Our main contribution is to extend the method of the adaptive control of the regularization parameters, introduced in [12] for the linear CLG model, to TV regularization. We started the work with a linear model which is an improved version of the CLG method consisting in the enhancement of the data term of the energy functional. We showed with numerous simulations and examples that the initial approach of [12] performs better when the model is improved and thus furnishes a general tool which could be used with many existing models in the literature of computer vision problems. We also showed that the use of high order finite element increases the accuracy, as it is expected in modern variational approximation theory. The computation of the errors and the convergence profiles allow to compare our results with well rated existing methods used in this field.

The extension of the method to the nonlinear framework is the largest and novel part of the thesis. We have used TV regularization which is widely used in image analysis, particularly because it allows for edge preserving treatment [76]. We studied this functional, and its regularized version which is more suited for numerical computations [76]. We established well posdness results and we performed the discretization of the associated Euler-Lagrange equations by finite element method. A crucial part of the work at this step is to define the "good" error indicators and to obtain sharp estimates for them. This is done with the use of a norm which is not the energy norm, but which is well suited to prove the equivalence of such error indicators and the discretization error with sharp constants. We derive an algorithm, in the spirit of the linear case, which allows for efficient computations of dense flow with high accuracy and its sparsification in adaptive way. The numerical results confirm the theoretical predictions and improve, as expected, the results obtained with the linear models. The strategy for adaptivity to select the regularization parameter, furnishes a distribution

of α which reveals the precise effects of the regularization term allowing for an efficient computation of the flow. Consequently, the reduction of the cost of computations with preserving accuracy constitute a nice future of the method and open some perspectives for its application in many fields (compression of video images, tracking motions, medical imaging, ...). Before that, implementing an optimized code with efficient scientific computing tools is a short term objective.

Even if the performances of the method are clearly pointed out by the numerical experiments of chapter 4 and 5, we should mention that they decrease for textured images. Such effects are well known and common to most known methods. The use of linear models or TV models are responsible of that, in a significant way, since they are favorable to smooth or cartoons images (i.e. H^1 or BV functions) and are less suited for textured images. But, in addition, our method based on the use of the error indicators, which tend to distribute uniformly the error on the computational domain increases this bad behavior near the textured regions. We think that this undesired effect could be corrected by using well suited models and by using the adaptive strategy only for the BV part of the image. One way to achieve this goal, is to use some decomposition strategy of the flow field. This is another perspective to our work.

Another improvement of the results comes from the use of anisotropic regularization, that we have introduced in chapter 5. Indeed, in this case, we use a matrix as regularization parameter instead of scalar function, the numerical results, in this case, are enhanced compared with the isotropic case, even in the textured regions. This work should be pursued and numerical experiments with real world images will be performed in near future.

7.2 Conclusion de la Thèse

Dans cette thèse, nous avons abordé le calcul des cartes de disparité en stéréovision et l'estimation du flot optique par des méthodes variationnelles. Notre contribution essentielle est d'étendre la méthode du contrôle adaptatif des paramètres de régularisation introduite dans [12], pour le modèle linéaire CLG pour calculer le flot optique, à la régularisation par variation totale. Nous commençons par un modèle linéaire, qui est une version améliorée de la méthode GLC induisant une amélioration du terme de données de la fonctionnelle énergie. Nous montrons, via de nombreuses simulations et exemples, que l'approche initiale [12] est meilleure lorsque le modèle est amélioré, et fournit alors un outil général qui peut ètre utilisé avec de nombreux modèles existant dans la littérature relative aux problèmes de vision par ordinateur. Nous montrons également que l'usage d'éléments finis d'ordres élevés augmente la précision, comme on s'y attend eu égard à la théorie de l'approximation variationnelle.

Le prolongement de la méthode au cadre non linéaire constitue la partie majeure de la thèse. Nous avons utilisé la régularisation par variation totale car elle est largement utilisée en analyse d'images, et permet de préserver les arêtes [76]. Nous étudions la fonctionnelle et sa version régularisée qui est plus favorable aux calculs numériques. Nous établissons le caractère bien posé des problèmes, et nous effectuons la discrétisation des équations d'Euler-Lagrange par la méthode des éléments finis. Une part essentielle du travail à ce stade est de définir les bons indicateurs d'erreur et l'erreur de discrétisation avec des constantes précisées. Les résultats numériques confirment les prédictions théoriques et améliorent, comme attendu, les résultats issus des modèles linéaires. La stratégie pour la séléction adaptative du paramètre de régularisation fournit une distribution de α qui traduit l'effet précis du terme de régularisation pour une sparsification du flot. En conséquence, la réduction du coût des calculs conjointe à la préservation de la précision constitue un atout notable de la méthode, et ouvre des perspectives pour ses applications dans de nombreux domaines (compresion d'images vidéo,

détection de mouvement, imagerie médicale...). Avant cela, développer un code optimisé pour l'implémentation de la méthode avec des outils efficients de calcul scientifique est un objectif à court terme.

Même si les performances de la méthode sont clairement illustrées par les tests numériques des chapitres 4 et 5, nous remarquons cependant qu'elles diminuent pour des images texturées. De tels effets sont bien connus et communs à la plupart des méthodes. L'usage de modèles linéaires ou de modèles à variation totale sont plus favorables à des images régulières (H^1) ou "cartoons" (BV) et moins bonnes pour des images bruitées ou hautement texturées. Cependant, notre méthode basée sur l'usage des indicateurs d'erreur, qui tendent à distribuer uniformément les erreurs sur le domaine de calcul, améliore la situation à proximité des régions texturées. Nous pensons que l'effet indésirable pourrait être corrigé en utilisant des modèles favorables et en utilisant une stratégie adaptative uniquement pour la partie BV de l'image. C'est une perspective supplémentaire issue de notre travail.

Une autre amélioration des résultats provient de l'usage de la régularisation anisotropique, introduite au chapitre 5. En effet, dans ce cas, nous utilisons une matrice pour le paramètre de régularisation au lieu de fonctions scalaires ; les résultats numériques sont améliorés comparés au cas isotrope, même dans les régions texturées. Le travail devrait se poursuivre, et des tests numériques avec des images issues du monde réel seront effectués dans un futur proche.

Appendix A

A.1 Finite difference method for Perona-Malik diffusion model

In this appendix we present finite difference method using an explicit numerical scheme. For the detailed discussion on this method we refer the reader to [94]. we consider the same problem as in chapter 6.

$$\partial_t u = \mathtt{div}(\mathrm{g}(|\nabla u|^2)\nabla u) \text{ in } \mathbb{R}^+ \times \Omega \tag{A.1}$$

$$u(0, \mathbf{x}) = f(\mathbf{x}) \text{ on } \Omega$$

$$\frac{\partial u}{\partial \nu} = 0 \text{ on } \mathbb{R}^+ \times \Omega$$

where $\Omega \subseteq \mathbb{R}^d$ is a bounded open set. where

$$\mathrm{g}(s^2) := \frac{1}{1 + s^2/\lambda^2} \tag{A.2}$$

A.2 Problem Discretization

A.2.1 One dimensional case

Discrete operators: We discretized the given derivatives using following formulas for finite difference operators, where D^- is denoted as backward operator and $D^+$is denoted as forward difference operator. The central difference operator is given by D^-D^+.

$$(D_h^- u)_i = \frac{1}{h}(u_i - u_{i-1}),\ i \in \{1, \dots N\} \tag{A.3}$$

$$(D_h^+ u)_i = \frac{1}{h}(u_{i+1} - u_i),\ i \in \{1, \dots N\} \tag{A.4}$$

$$\left(D_h^- D_h^+ u\right)_i = \frac{1}{h^2}\left(u_{i+1} - 2u_i + u_{i-1}\right) \tag{A.5}$$

The N is number of nodes on rectangular grid. The discrete form of time derivative is given as

$$\partial_t u \approx \frac{u_i^{k+1} - u_i^k}{\tau} \tag{A.6}$$

Proposition :A1: We propose the following explicit discrete scheme to solve the problem (A.1)

$$u^{k+1} = \underbrace{\mathbf{I} + \tau A(u^k)u^k}_{Q(u^k)} where$$

u=($u_1, \ldots, u_N$) and $N \times N$ matrix $A = (a_{k,l}(u))$ is obtained from spatial discretization. (A.7)

Proof: The the scheme (A.2.1) is the compact form of following discrete form of problem (A.1)

$$u_i^{k+1} = u_i^k + \frac{\tau}{h}\left(g_{i+1/2}^k \frac{u_{i+1}^k - u_i^k}{h} - g_{i-1/2}^k \frac{u_i^k - u_{i-1}^k}{h}\right) \tag{A.8}$$

A.2.2 Stencil Notation

Equation (A.8) can be written as

(A.9)

$$u_i^{k+1} = u_{i-1}^k \underbrace{\left(\frac{\tau}{h^2} g_{i-1/2}^k\right)}_{=:l_i} + u_i^k \underbrace{\left(1 - \frac{\tau}{h^2} g_{i+1/2}^k - \frac{\tau}{h^2} g_{i-1/2}^k\right)}_{=:ci} + u_{i+1}^k \underbrace{\left(\frac{\tau}{h^2} g_{i+1/2}^k\right)}_{=:r_i}$$

Thus the stencil for given discrete scheme is

l_i	c_i	r_i	=	$\frac{\tau}{h^2} g_{i-1/2}^k$	$1 - \frac{\tau}{h^2} g_{i+1/2}^k - \frac{\tau}{h^2} g_{i-1/2}^k$	$\frac{\tau}{h^2} g_{i+1/2}^k$

Above system can be formulated as a single matrix-vector product

$$\underbrace{\begin{pmatrix} u_1^{k+1} \\ \vdots \\ u_N^{k+1} \end{pmatrix}}_{u^{k+1}} = \underbrace{\begin{pmatrix} q_{1,1} & \cdots & q_{1,N} \\ \vdots & \ddots & \vdots \\ q_{N,1} & \cdots & q_{N,N} \end{pmatrix}}_{Q(u^k)} \underbrace{\begin{pmatrix} u_1^k \\ \vdots \\ u_N^k \end{pmatrix}}_{u^k} \tag{A.10}$$

$$Q(u^k) = \begin{pmatrix} l_1 + c_1 & r_1 & & & & \\ & l_2 & c_2 & r_2 & & \\ & & l_3 & c_3 & r_3 & \\ & & & \ddots & \ddots & \ddots \\ & & & & l_N & c_N & r_N \end{pmatrix} \tag{A.11}$$

Remarks:

– Unit row sums:

– $\forall i \in \{1, \ldots, N\}$

$$\begin{aligned}\sum_{j=1}^{N} q_{i,j} &= l_i + c_i + r_i \\ &= (\frac{\tau}{h^2} g^k_{i-1/2}) + (1 - \frac{\tau}{h^2} g^k_{i+1/2} - \frac{\tau}{h^2} g^k_{i-1/2}) + (\frac{\tau}{h^2} g^k_{i+1/2}) \\ &= 1\end{aligned}$$

– As $Q(u^k)$ is symmetric , column sums are equal to row sums:

– Unit row sums:$\forall j \in \{1, \ldots, N\}$

$$\sum_{j=1}^{N} q_{i,j} = \sum_{j=1}^{N} q_{j,i} = 1$$

– From above properties we can state that nonlinear diffusion preserves the average grey level.

– However, the maximum-minimum principle is not necessarily satisfied as the diagonal entries $q_{i,i} (i = 1 \ldots N)$ might be negative.

– We can impose the condition $c_i \geq 0$

– or $1 - \frac{\tau}{h^2} g^k_{i+1/2} - \frac{\tau}{h^2} g^k_{i-1/2} \geq 0 \Rightarrow \tau \leq \frac{1}{2} h^2$ for $|g_i| \leq 1$

– Thus maximum-minimum principle is satisfied if $\tau \leq \frac{1}{2} h^2$ and $|g_i| \leq 1$

A.2.3 Discretization in two dimensions

Let we rewrite the continuous diffusion equation as

$$\partial_t u = \partial_x (g(|\nabla u|^2) \partial_x u) + \partial_y (g(|\nabla u|^2) \partial_y u) \tag{A.12}$$

$u^k_{i,j}$ approximate $u((i - \frac{1}{2})h_1, u((j - \frac{1}{2})h_2, k\tau)$ with spatial grid sizes h_1, h_2 and time step size τ where

$$\partial_t u \approx \frac{u^{k+1}_{i,j} - u^k_{i,j}}{\tau}.$$

and

$$\partial_x (g \partial_x u) \approx \frac{1}{h_1} \Big((g \partial_x u)^k_{i+1/2} - (g \partial_x u)^k_{i-1/2} \Big)$$

(A.8) can be modified as.

$$
\begin{aligned}
u_{i,j}^{k+1} &= u_{i,j}^{k} + \frac{\tau}{h_1}\left(g_{i+1/2,j}^{k}\frac{u_{i+1,j}^{k}-u_{i,j}^{k}}{h_1} - g_{i-1/2,j}^{k}\frac{u_{i,j}^{k}-u_{i-1,j}^{k}}{h_1}\right) \\
&\quad + \frac{\tau}{h_2}\left(g_{i,j+1/2}^{k}\frac{u_{i,j+1}^{k}-u_{i,j}^{k}}{h_2} - g_{i,j-1/2}^{k}\frac{u_{i,j}^{k}-u_{i,j-1}^{k}}{h_2}\right) \qquad \text{(A.13)}
\end{aligned}
$$

The diffusivity $g_{i+1/2,j}^{k}$ is the arithmetic mean of $g_{i,j}^{k}$ and $g_{i+1,j}^{k}$. $g_{i,j}^{k}$ can be computed as follows

$$
\begin{aligned}
g_{i,j}^{k} &= g\left((\partial_x u)^2 + (\partial_y u)^2\right)_{i,j}^{k} \\
&\approx g\left(\left(\frac{u_{i+1,j}^{k}-u_{i-1,j}^{k}}{2h_1}\right)^2 + \left(\frac{u_{i,j+1}^{k}-u_{i,j-1}^{k}}{2h_2}\right)^2\right)
\end{aligned}
$$

A.2.4 Stencil notation in 2D case

The stencil notation for (A.13) is given as

0	$\tau g_{i,j+1/2}^{k}$	0
$\tau g_{i-1/2,j}^{k}$	-$\tau g_{i,j+1/2}^{k}$ -$\tau g_{i-1/2,j}^{k} + 1 - \tau g_{i-1/2,j}^{k}$ -$\tau g_{i,j-1/2}^{k}$	$\tau g_{i+1/2,j}^{k}$
0	$\tau g_{i,j-1/2}^{k}$	0

Remarks:

- space and time-dependent averaging where weights sum up to 1.
- Central weight become negative if τ is two large $\Longrightarrow$ instability.
- Conditionally stable for $|g| \leq 1$ when $\tau \leq 0.25$

A.3 Numerical Experiments

We consider the Lena image available at http://www.imageprocessingplace.com/ and test the explicit numerical scheme with various time iterations, we keep the $\tau \leq 0.25$, and present the some results for different combinations of time T and the threshold parameter λ. Though the finite element method is slower as

compared to finite difference method from computational(time) point of view, but from our numerical results one can observe that diffusion process in the case of explicit scheme based of finite difference scheme is slower as compared to the unconditionally stable implicit scheme based on finite element method. In first experiment we add the noise with $SD = 20$ and perform our experiment and in second case we increase noise with $SD = 40$ and then check the performance of numerical scheme. Results are given with caption showing the purpose of respective image.

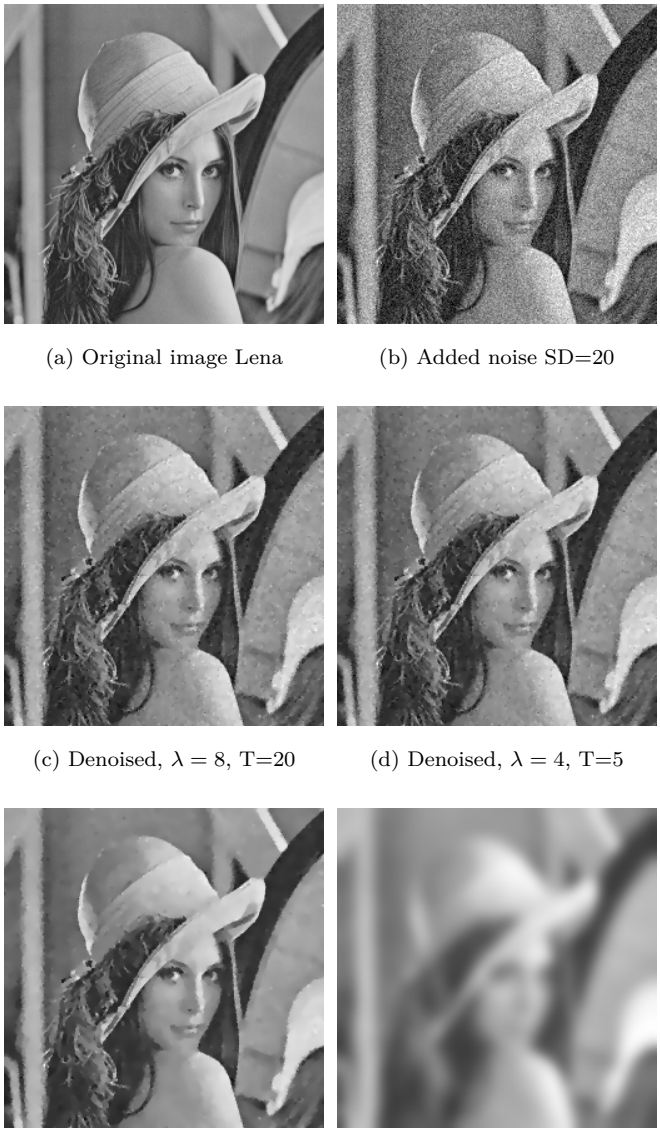

(a) Original image Lena (b) Added noise SD=20

(c) Denoised, $\lambda = 8$, T=20 (d) Denoised, $\lambda = 4$, T=5

(e) Denoised, $\lambda = 4$, T=20 (f) Denoised, $\lambda = 4$, T=80

Figure A.1: Denoising Lena image, noise added $SD = 20$

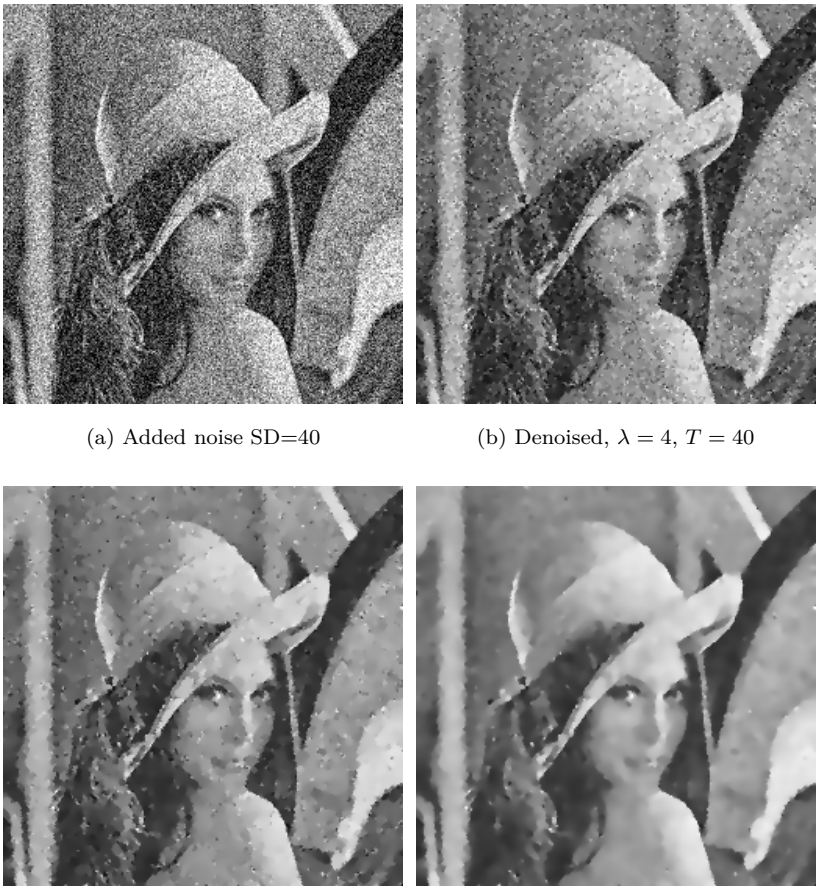

(a) Added noise SD=40

(b) Denoised, $\lambda = 4$, $T = 40$

(c) Denoised, $\lambda = 4$, $T = 80$

(d) Denoised, $\lambda = 8$, $T = 40$

Figure A.2: Denoising Lena image, noise added $SD = 40$

Bibliography

[1] J. Abhau, Z. Belhachmi, and O. Scherzer. On a Decomposition Model for Optical Flow and Stereo-Vision Problems EMMCVPR '09: Proceedings volume 5681, pages 126-139, Berlin, Heidelberg, 2009. Springer-Verlag.

[2] L. Alvarez, R. Deriche, J. Sanchez and J. Weickert. Dense disparity map estimation respecting image derivatives: a PDE and scale-space based approach. Journal of Visual Communication and Image Representation, 13, 321, 2002.

[3] L. Alvarez, J. Esclarin, M. Lefebure, and J. Sanchez. A PDE model for computing the optic flow. In Proc. XVI Congreso de Ecuaciones Diferenciales y aplicationes, Las Palmas de Gran Canaria, Spain (1999), 1349-1346.

[4] P. Anandan. A computational framework and an algorithm for the measurement of visual motion. International Journal of Computer Vision, volume 39(1)2000, 41-56.

[5] G. Aubert, R. Derriche, P. Kornprobst. Optic flow estimation while preserving its discontinuities:a variational approach. In Proc. Second Asian Conference on Computer Vision, vol 2, Singapore (1995) 290-295.

[6] G. Aubert, R. Deriche, P. Kornprobst. Computing optical flow

via variational techniques. SIAM Journal on Applied Math, 60 (1) (1999), 156-182.

[7] R.B. Ari and N.A. Sochen. Variational stereo vision with sharp discontinuities and occlusion handling. In Proceedings of the 2007 IEEE International Conference on Computer Vision, Rio de Janeiro, Brazil, IEEE Computer Society Press, 17, 2007.

[8] Aubert, G. and Kornprobst. P.Mathematical Problems in Image Processing: Partial Differential Equations and the Calculus of Variations. Springer-Verlag,second edition 2006, vol.147.

[9] P.Amster, Cassinelli, M.C.Mariani and D.F.Rial. Existence and Regularity of weak solutions to the prescribed mean curvature equation for a nonparametric surface.

[10] Antonin Chambolle. An algorithm for total variation minimization and applications. Journal of Mathematical imaging and vision 20:89-97, 2004.

[11] Robert A. Adams and John J. F. Fournier. Sobolev spaces. Academic press, Elsevier, 2003.

[12] Z.Belhachmi and F.Hecht. Control of Effects of the regularization on variational optic flow computations. J.Mathematical imaging and vision, 40(1), 1-19, 2010.

[13] Z. Belhachmi, C. Bernardi, A. Karageorghis. Mortar spectral element discretization of non homogeneous and anisotropic Laplace and Darcy equations. M2AN, 41, 4(2007), 801-824.

[14] Z. Belhachmi, D. Bucur. Stability and uniqueness for the crack identification problem. Siam J. Control. Optimal 46, 1 (2007), 253-273.

[15] S.Baker,D.Scharstein, J.P. Lewis,ů Stefan Roth,ů Michael J. Black, R.Szeliski. A Database and Evaluation Methodology for Optical Flow.Int J Comput Vis (2011) 92: 1Ű31.

[16] A. Bruhn, J. Weickert. Confidence measure for variational optic flow methods, computational Imaging and Vision. Springer, Dordrecht, 2005.

[17] Andres Bruhn. Variational Optic Flow Computation, accurate modeling and efficient numerics. PhD thesis in computer Science(2006) Saarbrücken, Germany.

[18] A. Bruhn, J. Weickert, C. Schnörr. Combining the advantages of local and global optic flow methods, in Van Gool Editor, Pattern recognition, Vol 2449 Lecture notes in computer sciences , Springer Berlin (2002), 454-462.

[19] A.Bruhn, Joachim Weickert, Christophschnorr. Lucas/Kanade meets Horn/Schunck: Combining Local and Global Optic flow methods, International Journal of computer vision 61(3),211-231,2005.

[20] A Bruhn, Levi Valgaerts, Michael Breub, Jaochim Weickert, Bodo Rosenhahn and Hans-Peter Seidel. PDE-Based Anisotropic Disparity-Drivin Stereo Vision, MIA group Saarland University Saarbrouken, Germany August 17th, 2006.

[21] T. Brox, A. Bruhn, N. Papenberg and J. Weickert. High accuracy optical flow estimation based on a theory for warping. Lecture Notes in Computer Science. Springer, Berlin, 25Ű36, 2004.

[22] A. Borzi, K. Ito, K. Kunisch. Optimal control formulation for determining the optical flow, SIAM J. Sci. Computing, 24 (3) (2002), 818-847.

[23] J.Bigün, H. Granlund, J. Wiklund. Multidimensional orientation estimation with applications to textures analysis and optic flow, IEEE Transactions on pattern analysis and machine intelligence, 13, 8 (1991), 775-790.

[24] J.Bigün, Granlund, G.H. Optical Flow based on inertia matrix in frequency domain. Proc.SSAB Symposium on Picture Processing, Lund, Sweeden, 1988.

[25] Barron, J.L., Fleet, D.J., and Beauchemin S.S. Performance of optical flow techniques. International Journal of Computer Vision 1994.

[26] S.C Brenner and L.R.Scott. The mathematical theory of finite element methods, Springer, 1994.

[27] G.Bellettini, M.Novaga, M.Paolini and C.Tornese. Convergence of discrete schemes for the Perona-Malik equation. J. Diff. Eq., 245 (2008), 892-924.

[28] Christian Grossmann, Hans-Grg Roos, Martin stynes. Numerical Treatment of Partial Differential Equations. Springer, 2007.

[29] CHANG HUI YAO. Finite element approximation for tv regularization. International journal of numerical analysis and modeling, 2008, volume 5, number3, 516-526.

[30] A. Chambolle and P.-L. Lions. Image recovery via total variation minimization and related problems. Numer. Math., 76(2):167-188, 1997.

[31] T. Corpetti, E. Mémin. Stochastic uncertainty models for the luminance consistency assumption. IEEE Trans. on Image Proc, 2011

[32] A. Chambolle. An algorithm for total variation minimization and applications. J. Math. Imaging Vision, 20(1-2), 89-97, 2004.

[33] P.G. Ciarlet. Basic Error Estimates for Elliptic Problems, in the Handbook of Numerical Analysis, Vol. II, P.G. Ciarlet and J.L. Lions eds, North-Holland, 1991, 17-351.

[34] Danna H.Ballard , Christopher M.Brown. Computer vision. Prentice-Hall, Inc, 1982.

[35] Daniel Scharstein,Richard Szeliski. A Taxonomy and evaluation of Dense Two-Frame Stereo Correspondence Algorithms, International Journal of Computer Vision. 2002, Volume 47, 7-42.

[36] B.Dacorogna. Direct Methods in the Calculus of Variations. Springer-Verlag, Berlin, 1989.

[37] T. Dupont, R. Scott. Polynomial approximation of functions in Sobolev spaces. Math. Comp. 34 (1980), 441-463.

[38] D.C. Dobson and C.R. Vogel. Convergence of an iterative method for total variation denoising. SIAM J. Numer. Anal., Vol. 34, No. 5, pp. 1779-1791, 1997.

[39] H. Engl, M. Hanke, A. Neubauer. Regularization of inverse problems. Kluwer Acad. Publ. (1996), Dordrecht.

[40] H. Engl, K. Kunisch, A. Neubauer. Convergence rates for Tikhonov regularization of nonlinear ill-posed problems. Inverse Problems. 5 (1989), 523-540.

[41] A.Ern and J.-L. Guermond. Theory and practice of finite elements. Springer, 2004.

[42] H. Engl, M. Hanke, A. Neubauer. Regularization of inverse problems. Kluwer Acad. Publ, 1996.

[43] Frdric Hecht, Olivier Pironneau,Jacques Morice. FreeFem++ . http://www.freefem.org/ff++/

[44] Francesca Fierro and Andreas Veeser. On the A posteriori error analysis for equations of prescribed mean curvature. Mathematics of Computation, Volume 72, Number244, 1611-1634, March 26, 2003.

[45] T. Froehlinghaus and J. Buhmann. Regularizing phase based stereo. In International Conference on Pattern Recognition, Part I. 451Ű455, 1996.

[46] David Gilbarg, Neil S. Trudinger. Elliptic Partial Differential Equations of Second Order Springer 1998.

[47] Gilles Aubert, Pierre Kornprobst. Mathematical Problems in image processing, Partial differential equations and calculus of variations. Springer Volume 147.

[48] V. Girault, P.A. Raviart Finite element methods for the Navier-Stokes equations, Theory and algorithms. Springer-Verlag (1986).

[49] W.E.L. Grimson. Computational experiments with a feature based stereo algorithm. IEEE Transactions on Pattern Analysis and Machine Intelligence, 7, 17Ű34, 1985.

[50] M. Ghisi, M. Gobbino. Gradient estimates for the Perona-Malik equation. Math. Ann. 3 (2007), 557Ű590.

[51] B.Horn, B.Shunk. Determining optical flow. Artificial Intelligence, VOL.17(1981), 185-203.

[52] Henning Zimmer, Andres Bruhn, Jaochim Weickert, Levi Valgaerts, Agustin Salgado, Bodo Rosenhahn and Hans-Peter Seidel. Complementary optic flow. 7th International Conference, EMMCVPR 2009, Bonn, Germany, August 24-27, 2009.

[53] W. Hinterberger, O. Scherzer, C. Schnör J. Weickert. Analysis of optical flow models in the framework of calculus of variations. Numerical Functional Analysis and Optimization 23 (1-2), 2002, 69-89.

[54] Irena Galic, Joachim Weickert, Martin Welk, Andres Bruhn, Alexander Belyaev, Hans-Peter Siedel. Image Compression with Anisotropic Diffusion. Journal of Mathematical Imaging Vis(2008) 31:255-269.

[55] Issaque Cohen Nonlinear Variational Method for Optical Flow Computation. 8th SCIA, 523-530, June 93.

[56] Jrgen Jost, Xianquing Li-Jost. Calculus of variations. Cambridge studies in Advanced mathematics 64.

[57] Jean-Fran cois Aujol. Some first-order algorithms for total variation based image restoration. J.Mathematical imaging and vision, 34(4), 307-327, 2009.

[58] A. Klaus, M. Sormann and K. Karner. Segment-based stereo matching using belief propagation and a self-adapting dissimilarity measure. In Proceedings of the 18th International Conference on Pattern Recognition, Part III. 15Ű18, 2006.

[59] A. Kumar, A.R. Tannenbaum, G. J Balas. Optic flow: a curve evolution approach. IEEE Transactions on image processing, 5, 4 (1996), 598-610.

[60] S.Kichenassamy. The Perona Malik paradox. SIAM J. Appl. Math. 57:1328-1342, 1997.

[61] V.Kolmogorov and Ramin Zabih. Multi-camera scene reconstruction via graph cuts. In A. Heyden, G. Sparr,M. Nielsen and P. Johansen, Computer Vision - ECCV 2002, Part III. Volume 2352 of Lecture Notes in Computer Science. Springer, 8296, 2002.

[62] G. Li and S.W. Zucker. Differential geometric consistency extends stereo to curved surfaces. Volume 3953, Lecture Notes in Computer Science, Springer, 44Ű57, 2006.

[63] C. Lei, J. Selzer, and Y.-H. Yang. Region-tree based stereo using dynamic programming optimisation. In Proceedings of the IEEE Computer Society Conference on Computer Vision and Pattern Recognition. 2378Ű2385, 2006.

[64] Leonid P.lebedev, Michael J.Cloud. The calculus of variations and Functional analysis with optimal control and applications in mechanics, World Scientific, Vol.12, 2003.

[65] Lucas B., Kanade T. An iterative image registration technique with an application to stereo vision. In Proc.seventh International Joint Conference on Artificial Intelligence, Vancouver(1981), Canada, pp 674-679.

[66] Luis Alvarez, Rachid Deriche, Javier Snchez, Joachim Weickert. Dense Disparity Map Estimation Respecting Image Discontinuities: A PDE and Scale-Space Based Approach, research report no. 38-74 January 2000, INRIA Sophia Antipolis 2004, France.

[67] D. Mumford and J. Shah. Boundary detection by minimizing functionals. In Proceedings of the International Conference on Computer Vision and Pattern Recognition, pages 22Ű26, San Francisco, CA, June 1985. IEEE.

[68] A.Mansouri, A.Mitiche and J. Konrad. Selective image diffusion: application to disparity estimation. In Proceedings of the 1998 IEEE International Conference on Image Processing. Volume 3., Chicago, IL, 284Ű288, 1998.

[69] Meyers, N.G., Serrin, J. (1964) H = W. Proc. Nat. Acad. Sci. USA 51 (1964), 1055-1056.

[70] Nagel, H.H. 1983. Constraints for the estimation of displacement vector fields from image sequences. In Proc. Eighth Int. Joint Conf. on Artificial Intelligence, IJCAI 83, Karlsruhe, Aug. 812, 1983, pp. 945951.

[71] H.H. Nagel Extending the oriented smoothness constraint into the temporal domain and the estimation of the derivatives of optical flow. Lectures notes in computer sciences, Springer Berlin (1990), 139-148.

[72] H.H. Nagel, W. Enkelmann. An investigation of smoothness constraints for the estimation of displacement vector fields from image sequences. IEEE Transactions on patterns analysis and machine intelligence 8 (1986), 565-593.

[73] L. Oisel, E. Mémin, L. Morin, F. Galpin. 1D dense disparity estimation for 3D reconstruction. IEEE Trans. on Image Processing, 12(9):1107-1119, September 2003.

[74] P. Perona, Malik. Scale space and edge detection using anisotropic diffusion, IEEE, Trans, Pattern anal. Match.Intell 12(1990), 629-639.

[75] Philippe G. Ciarlet. Introduction to numerical linear algebra and optimization, Cambridge Texts in Applied Mathematics, Cambridge University Press, 1989.

[76] L.I. Rudin, S. Osher and E. Fatemi. Nonlinear total variation based noise removal algorithms. Physica D, 60, 259268, 1992.

[77] . Ridgway L. Scott and Shangyou Zhang. Finite element interpolation of nonsmooth functions satisfying boundary conditions. Mathematics of Computation, 54(190), 483-493, 1990.

[78] E.P. Simoncelli, E.H. Adelson, D.J. Heeger. Probability distributions of optical flow. Proc. IEEE computer society conference on computer vision and pattern recognition (1991), 310-315.

[79] C. Schnörr. Segmentation of visual motion by minimizing convex non quadratic functionals. In Proc. Twelfth International Conference on Pattern and Recognition, volume A, IEEE Computer society press (1994), 661-663.

[80] C. Schnörr. Unique reconstruction of piecewise smooth images by minimizing strictly convex non-quadratic functionals. Journal of Mathematical Imaging and Vision, 4(1994), 189-198.

[81] N. Slesareva, A. Bruhn and J. Weickert. Optic flow goes stereo: A variational method for estimating discontinuity-preserving dense disparity maps. In W. Kropatsch, R. Sablatnig and A. Hanbury, eds.: Pattern Recognition. Volume 3663 of Lecture Notes in Computer Science, Springer, Berlin, 3340, 2005.

[82] A.Schatz. An observation concerning Ritz-Galerkin Methods with indefinite bilinear forms. Math.Comp.28(1974), pp.959-962.

[83] D.M. Strong. Adaptive Total Variation Minimizing Image Restoration. CAM Report 97-38, University of California, Los Angeles, 1997.

[84] Y. Li and F. Santosa. A computational algorithm for minimizing total variation in image restoration. IEEE Trans. Image Processing, Vol. 5, pp. 987-95, 1996.

[85] A. N. Tikhonov. Solution of incorrectly formulated problems and the regularization method. Soviet Mathematics Doklady, 4 (1963),1035-1038.

[86] A. N. Tikhonov and V.Y.Arsenin. Solution of ill-posed problems. Winston and Sons, Washington, DC, 1977.

[87] B.Ter Haar Romeny, L.Florack, J. Kooenderink, M. Viergever(Eds). Scale-space theory in computer vision, Lecture Notes in computer Science, Vol.1252, Springer, Berlin, 1997.

[88] R.Verfürth. A Review of a posteriori error Estimation and Adaptive mesh-refinement Techniques. Advances in Numerical Mathematics, Wiely and Teubner(1996).

[89] V.Kolmogorov and Ramin Zabih. Multi-camera scene reconstruction via graph cuts. In A. Heyden, G. Sparr,M. Nielsen and P. Johansen, Computer Vision - ECCV 2002, Part III. Volume 2352 of Lecture Notes in Computer Science. Springer, 8296, 2002.

[90] J.Weickert and Schnörr. A Theoretical Framework for Convex Regularizes in PDE-Based Computation of Image Motion. International Journal of Computer Vision 45,245-264,2001.

[91] Weickert, J. and Schnörr, C. 2001. Variational optic flow computation with a spatio-temporal smoothness constraint. Journal of Mathematical Imaging and Vision, 14(3):245255.

[92] Joachim Weickert, Differential Equations in Image Processing and Computer Vision. lecture slides MIA group Saarbrüken, Summer Term 2009.

[93] J Weickert, Andres Bruhn, Thomas Brox and Nils Papenberg. A Survey on Variational Optic Flow Methods for Small Displacements. FR 6.1-Mathematics University of Sarlandes, Postfach 15 11 50, 6641 Saarbrücken Germany, 2005.

[94] J. Weikert. Lecture notes PDE's in computer vision and image processing 2009.

[95] J.Wiekert Anisotropic Diffusion in Image Processing. B.G. Teubner Stuttgart 1998.

[96] Xiaobing Feng, Michael Neilan, and Andreas Prohl. Error analysis of finite element approximations of the inverse mean curvature flow arising from the general relativity. Numer.Math.2007, volume 108, 1, 93-119.